A Study of $K\eta$ final state in the reaction $K^-p \to K^-\eta p$ at 11 GeV.

11GeV $K^-p \to K^-\eta p$反応における $K\eta$系の研究

林井　久樹

主論文

A study of the $K\eta$ final state in the reaction $K^-p \to K^-\eta p$ at 11 GeV/c

HISAKI HAYASHII

December 1987

ABSTRACT

The first observation of K^* state in the $K\eta$ system is presented. The $K\eta$ system was studied in the reaction $K^-p \to K^-\pi^+\pi^-\pi^0 p$ at 11 GeV/c using the data obtained by the Large Aperture Superconducting Solenoid (**LASS**) spectrometer at SLAC. The sensitivity of the K^- beam experiment was $\sim$ 4.1 events/nb. The $K^-\eta$ effective mass spectrum shows a prominent peak at $\sim$ 1.75 GeV/c^2, which is shown to be due to the $K_3^*(1780)$ by a spherical moment analysis and amplitude decomposition. There is no significant signal of $K_2^*(1430)$. The measured branching ratios for leading $L = 1, L = 2 K^{*'}$s are $BR(K_2^*(1430) \to K\eta) < 0.45$ % at the 95% c.l. and $BR(K_3^*(1780) \to K\eta) = 9.4 \pm 3.4$ %, respectively, which confirm the SU(3) prediction that $K\eta$ couples preferentially to odd spin K^*.

ACKNOWLEDGEMENTS

The work repoted here is the results through the efforts of many people in a collaboration between Group-B at SLAC, University of Cincinnati and Nagoya University. In particular, I would like to appreciate to the staffs of Group-B: David Aston, Bill Dunwoodie, Blair Ratcliff and David Leith for their excellent organization of the experiment and many useful suggestions of the analysis.

I would like to acknowledge the continuous guidance and encouragement of my adviser Ryoichi Kajikawa, Seigi Iwata and Shiro Suzuki. Their helps and fruitful discussions were invaluable for the completion of this analysis. I am indebted to Mayori Takahashii and Asako Nagai for their excellent tape management and helps to process many jobs of this analysis. Lillian Vasillia,the SLAC Group B secretary, helps and makes it comfortable during my stay.

I would like to express my appreciation to the staffs at Nara Woman Univertisity, Prof. S. Yamashita, N. Fujiwara S. Noguch and many students. The completion of this thesis is impossible without their understanding and encouragement.

Table of Contents

1. Introduction

There have been extensive studies of the strange mesons (K^*) in the $K\pi$ and $K\pi\pi$ final states [1,2,3,4,5,6,7], and decay branching ratios of the leading and underlying state below 2.0GeV/c^2 to these channels are relatively well measured. The K^* spectrums observed to date are summarized in fig.1, in which well established K^* resonances quoted in PDG summary table [8] are specified by underline. The states enclosed by dotted line are the resonances reported in the previous experiments [1,2,3,18], and are confirmed by the recent high statistical studies of $K^-\pi^+$ [4] and $K^0\pi^+\pi^-$ [5] channels. The new states found by these analyses are enclosed by solid line. The observed leading states† ($J^P = 1^-, 2^+, 3^-, 4^+$ and 5^-) of orbital excitations are now extended upto $J^P = 5^-$[4]. And many of the underlying triplet partner states expected from the conventional $q\bar{q}$ quark model have been seen together with good candidates for several radial excited states like $J^P = 1^- K_1(1410)$[4,5], $J^P = 2^+ K_2(1970)$[5] and $J^P = 0^+ K_0(1950)$[4].

However, no significant direct observation of K^*'s into the $K\eta$ final state have been reported so far [9] , and the PDG summary table [8] only cites an indirect measurement of the BR($K_2^*(1430) \to K\eta$) taken from a multi-channel fit.

The SU(3) flavor symmetry predicts an interesting feature of the decay properties of K^* resonances in the $K\eta$ state. As is discussed in the next chapter, the $K\eta$ branching fraction for even-spin K^* states will be extremely suppressed while those of odd-spin K^* should be quite substantial. It is of interest since the relative magnitudes of these couplings to even and odd spin K^* depend on the quark contents and the $\eta - \eta'$ octet-singlet mixing angle. Especially the magnitude of the destructive coupling in the $K\eta$ decay of even-spin K^* is sensitive to this mixing angle. A measurement of these branching fractions, therefore, provides a good test of SU(3) symmetry in the hadronic decay of the mesons.

The importance of measuring $K\eta$ decay branching fraction and confirming the selective coupling to even and odd spin K^* has been pointed out by Lipkin who [10],

---

† The leading resonance states mean the most highest spin state in a given mass region. The production cross section of these states are large in the fixed target experiment of hadron beam and most easily accessible. This situation is in contrast with the ψ, Υ states observed in e^+e^- collisions. In these experiments, the states which have the same quantum number to photon (i.e. vector state; $J^{PC} = 1^{--}$) are directory produced. Then the radial exitated states of vector meson ψ, ψ', ψ''... $\Upsilon, \Upsilon', \Upsilon''$... are most popular resonances of $c\bar{c}, b\bar{b}$ bound states.

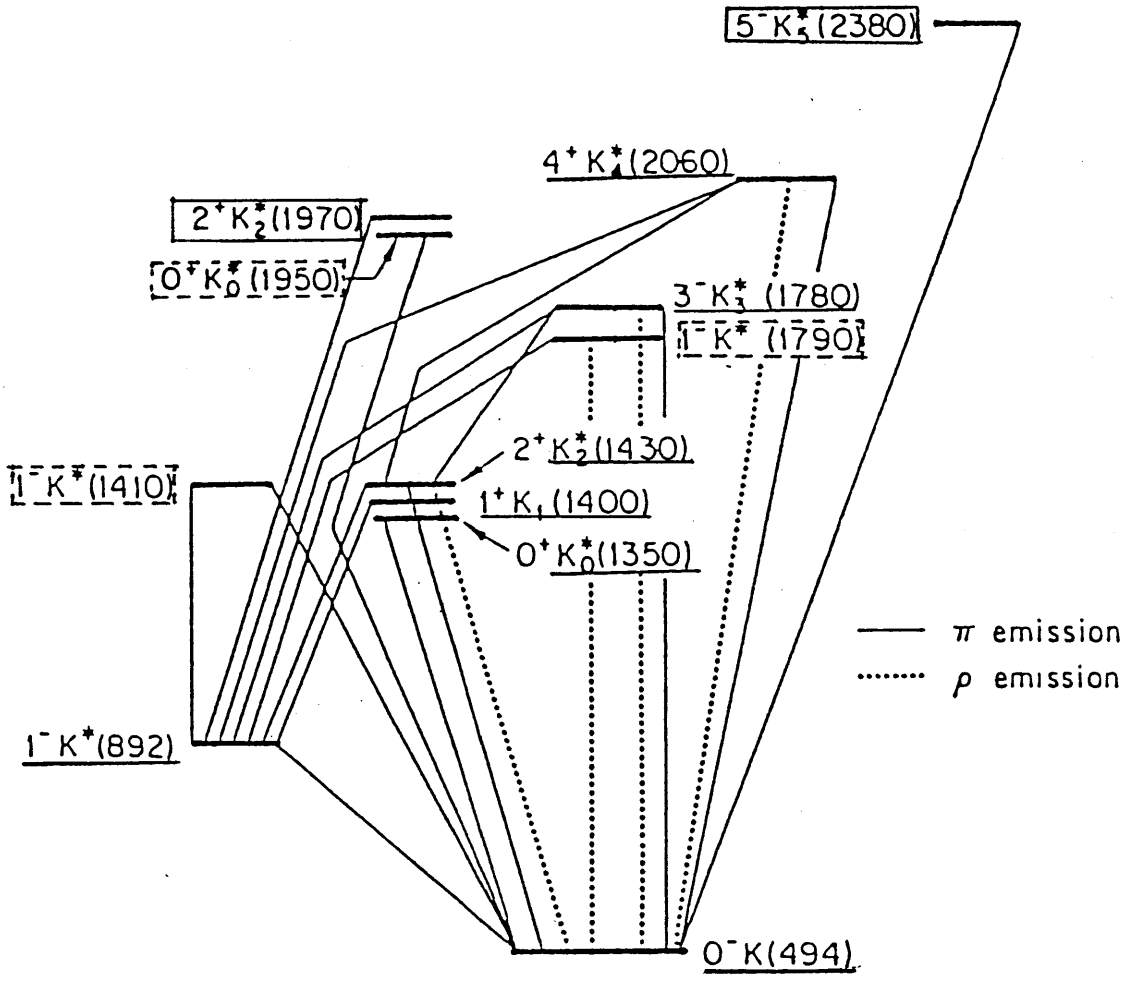

Fig.1 K^* level diagram and the transition observed in $K^-\pi$[4] and $K^0\pi^+\pi^-$[5] channels. This diagram covers all K^* states observed to date except $J^P = 2^-$ $K_2(1770)$ and $J^P = 0^-$ $K_0(1400)$.

emphasized that the same arguments lead to a good methode of distinguishing two different classes of diagrams in the non-leptonic decay of the charmed D^0 meson. In general, it is expected that many diagrams may contribute in this decay and its decay mechanism may be complicated. But as far as the final quark constituent is concerned, there are only two mechanisms for creation of the additional quark pair by weak interaction and by strong final state interaction, as shown in fig.2 and fig.3, respectively. In these figures, a box denotes any arbitrary set of diagrams. (1): In the diagram shown in fig.2 , the additional quark pair in the final state is created directly in the weak decay of the charmed quark $c \to su\bar{d}$. Then the final state has the quark constituents $(s\bar{d})(u\,\bar{u})$. The typical example of this class is the spectator diagram shown in fig.4. (2): While in the diagram of fig.3 , the additional quark pair $q\,\bar{q}$ (where q denotes either

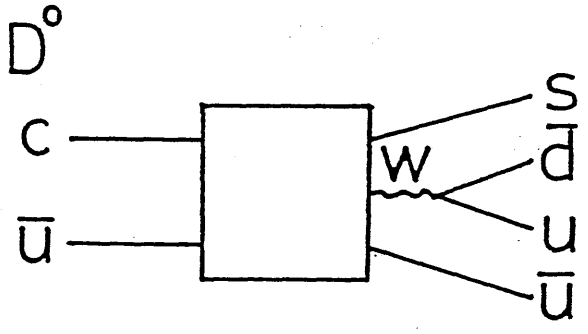

Fig. 2 Weak pair creation.

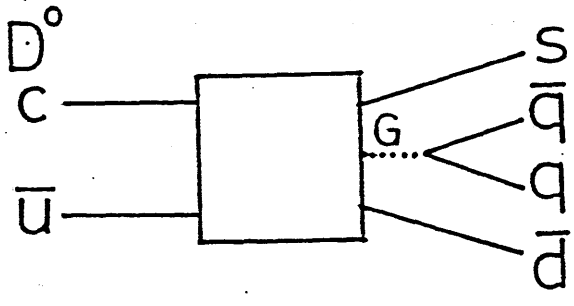

Fig. 3 Strong pair creation. G denote any number of gluons.

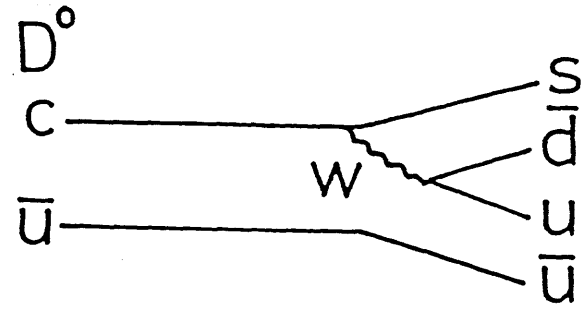

Fig. 4 The spectator diagram.

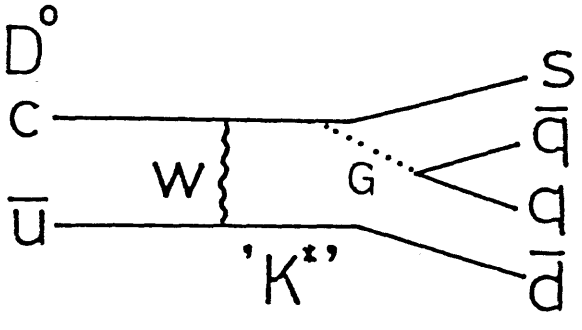

Fig. 5 The W exchange diagram.

u, d or s quark) is created by one or more gluons. An example of this class is the W exchange diagram shown in fig.5.

Lipkin emphasized that the branching ratios $D^0 \to \bar{K}^\circ\pi^\circ$ and $D^0 \to \bar{K}^\circ\eta$ are significantly different between these two classes of the diagrams. In the case (1), since the neutral pseudoscalar π°, η or η' is created via $u\bar{u}$ component, the decay rate of these three channels is roughly equal. However, in the mechanism (2), the $\bar{K}^\circ\eta$ decay of spin zero D^0 should be significantly suppressed by an order of magnitude with the same SU(3) argument that the strong $K\eta$ decay of even spin K^* is suppressed. In this mean, as well as the measurement of the $K\eta$ ($K\eta\prime$) branching fraction of D^0, the experimental check on the SU(3) relation in the strong decay K^* is important to really understand the effect of the mechanism (2) in the nonleptonic decay of D^0 meson [11].

The recent phenomenological analyses of exclusive decays of D meson [12,13] have shown reasonable life time difference of D^+ and D^0 by taking into account the destructive interference due to the presence of the two identical $\bar{d}$ in the decay $D^+ = [\bar{d}c] \to \bar{d}su\bar{d}$. This analysis mainly uses case (1) diagrams and case (2) diagrams(i.e. final state interaction) is partially taken into account. This analysis, however, has the problem in explaining the decay $D^0 \to \bar{K}^\circ\phi$, which only comes from the mechanism (2)[15]. The observation of this decay in several experiments [14] with a branching ratio of $\sim 1\%$ suggests the importance of the case (2) diagrams.

There is some indirect evidence for the expected suppression of the $K\eta$ decay mode of the spin zero K^*. Since the S-wave of $K\pi$ amplitude is fully elastic well above the $K\eta$ threshold [6], the $K\eta$ decay from spin zero K^* is expected to be suppressed. But the direct confirmation for any K^* states has not made until now because of the experimental limitations.

Together with these interests, a search of the exotic states is also important in this channel. In the gauge theory of the strong interaction(QCD), the requirement of the color singlet is believed to explain the confinement of quarks. The conventional meson $q\bar{q}$ and baryon qqq states are in the color singlet state. But other combinations such as multi-gluon states(glue ball ; ggg, gggg..), multi-quark states ($qq\bar{q}\bar{q}, qqqqq\bar{q}$) and hybrid states($q\bar{q}g$) are also possible to make color singlet. The search of these exotics has been carried out in the various reactions, and some evidence of exotic states have been reported in the "gluon rich" channels. In the radiative decay of the J/ψ, the

$\iota(1400)$, the $\theta(1640)$ and the $\xi(2200)$ are seen as good candidates of exotics. Other claims have been made in the double OZI suppressed decay channel $\pi^- p \to \phi\phi p$. Three states g_T, g_T', g_T'' are reported in this reaction. The $K\eta$ system is not such gluon rich channel and pure glue ball states are not accessible, but other exotics such as 4-quark states ($qq\bar{q}\bar{q}$) or hybrid states ($q\,\bar{q}g$) may be in the range of our reach. In this regard, the search on the K^* member of exotic quantum number state $J^{PC} = 1^{-+}$ is important [22].

1.1 The overview of the thesis

Inspired by the considerations described above, the $K\eta$ final state is studied in the non-charge exchange reaction of

$$K^- p \to K^- \pi^+ \pi^- \pi^\circ p \tag{1.1}$$

at 11GeV/c using the Large Aperture Superconducting Spertrometer (**LASS**) at the Stanford Linear Accelerator Center. The entire K^- data set in this experiment consists of $\sim$ 120 million events corresponding to the experimental sensitivity $\sim$ 4.1 events/nb.

This thesis reports the full analysis of this $K\eta$ system with the data which are at least 20 times larger than any of the sample used in the previous experiments [9]. The organization of this thesis is as follows: In the next chapter, the SU(3) relations of K^* decay and the $\eta - \eta'$ mixing angle are discussed in some detail. After describing the apparatus in Chapter 3, event reconstruction and calibration procedure of each component are discussed in Chapeter 4. Chapter 5 describes the detailed event selection of the reaction (1.1). General features of the $K^-\eta$ events are presented in Chapter 6, followed by a description of the moments analysis. The decomposition of these moments into production amplitudes are carried out in Chapter 7. Using these resonance amplitudes, the production cross section and the relative branching ratios are determined. Finaly, Chapter 8 discusses the results and concludes the thesis.

2. The $K^* \to K\eta$ decay and $\eta - \eta'$ mixing angle

2.1 The $K^* \to K\eta$ decay branching ratios in SU(3)

To give more quantitative discussion on the K^* decays, two body decays of K^* resonance to the pseudo-scalars,

$$K^{*-} \to K^-\pi, K^-\eta, K^-\eta'$$

are discussed assuming SU(3) and pseudo-scalar nonet symmetry. The quark line diagrams shown in fig.6 show essential features of the SU(3) relations, and also give the relative decay branching ratios of these hadronic decays.

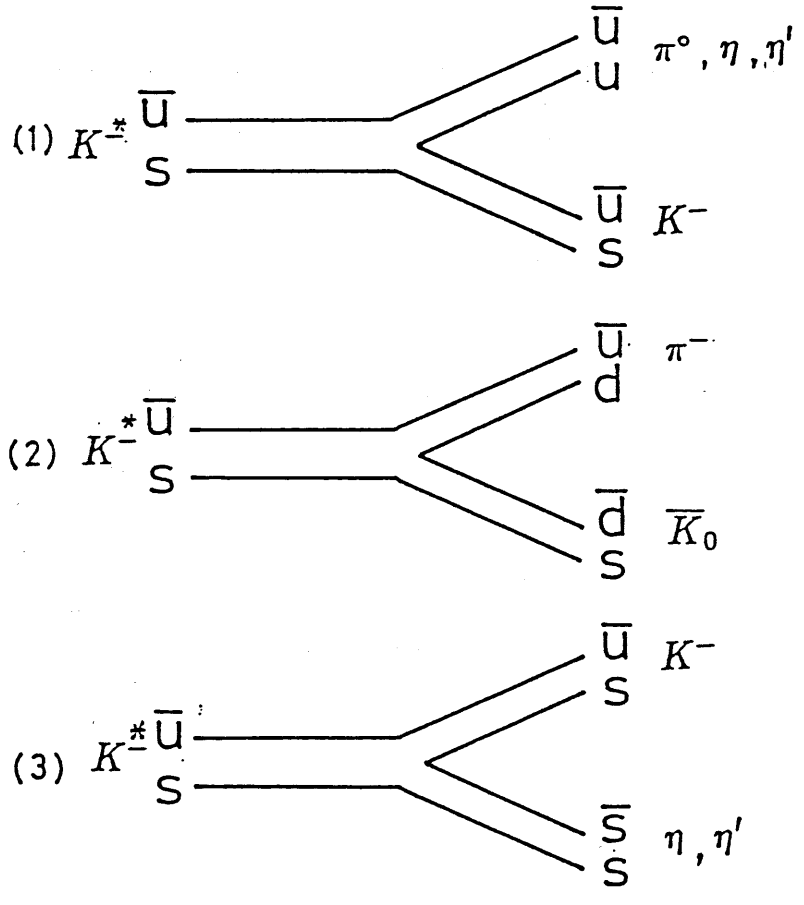

Fig.6 The quark line diagrams of the decays $K^{*-} \to K^-\pi, K^-\eta, K^-\eta'$. Each figure shows the additional quark-antiquark pair creation of (1) $u\bar{u}$, (2) $d\bar{d}$ and (3) $s\bar{s}$, respectively.

There is one quark-antiquark pair in the initial state and two pairs in the final state. Each diagram shows the additional pair creation of $u\bar{u}$, $d\bar{d}$ and $s\bar{s}$ quarks, respectively. Assuming these ampltitudes of pair creations are identical, the decay amplitude can be calculated from the quark contents of each meson state. The charged mesons are simply expressed by the quark wave functions such as $\pi^- = |u\bar{d}>$, while the neutral mesons in the pseudoscalar nonet π°, η_8 and η_1 (octet and singlet state) are expressed by the following form†

$$\begin{aligned} |\pi^\circ> &= \frac{1}{\sqrt{2}}|u\bar{u} - d\bar{d}> \\ |\eta_8> &= \frac{1}{\sqrt{6}}|u\bar{u} + d\bar{d} - 2s\bar{s}> \\ |\eta_1> &= \frac{1}{\sqrt{3}}|u\bar{u} + d\bar{d} + s\bar{s}> \end{aligned} \tag{2.1}$$

in the basis of SU(3). The physical states η and η' are given by mixing η_8 and η_1 states

$$\begin{aligned} |\eta> &= \cos\theta_p|\eta_8> - \sin\theta_p|\eta_1> \\ |\eta'> &= \sin\theta_p|\eta_8> + \cos\theta_p|\eta_1>, \end{aligned} \tag{2.2}$$

where θ_p is the octet-singlet mixing angle of pseudo-scaler nonet.

In this situation, the decay magnitude of $K^{*-} \to K\ \pi$ is given by incoherent sum of the diagrams (1) and (2) counting the quark contents of neutral and charged π mesons:

$$\begin{aligned} |<K\pi|K^{*-}>|^2 &= |<K^-\pi^\circ|K^{*-}>|^2 + |<\bar{K}^\circ\pi^-|K^{*-}>|^2 \\ &= g^2(|<\pi^\circ|u\bar{u}>|^2 + |<\pi^-|d\bar{u}>|^2) \\ &= g^2\left((\frac{1}{\sqrt{2}})^2 + 1^2\right) \\ &= \left(g\sqrt{\frac{3}{2}}\right)^2, \end{aligned} \tag{2.3}$$

where g is a SU(3) common coupling constant in all the diagrams.

On the other hand, $K^{*-} \to K^-\eta_8$ and $K^{*-} \to K^-\eta_1$ decay amplitudes are determined by the diagrams (1) and (3). Since the final state $K^-\eta_8$ and $K^-\eta_1$ are identical in these two diagrams, we must take care the symmetric nature of these decays.

---

† Since we are interested in the simplest case, we neglect the possibile mixing of the η and η' with other pseudoscalar states, such as radially excited quakonium states, gluonium, or exotics.

In the symmetric case, the decay amplitudes is given by adding diagrams (1) and (3) :

$$\begin{aligned}
< K^-\eta_8|K^{*-} >_{\rm sym} &=< K^-\eta_8|K^{*-} > + < \eta_8 K^-|K^{*-} > \\
&= g(< \eta_8|u\,\bar{u} > + < \eta_8|s\,\bar{s} >) \\
&= -g\frac{1}{\sqrt{6}} \\
< K^-\eta_1|K^{*-} >_{\rm sym} &=< K^-\eta_1|K^{*-} > + < \eta_1 K^-|K^{*-} > \\
&= g(< \eta_1|u\,\bar{u} > + < \eta_1|s\,\bar{s} >) \\
&= g\frac{2}{\sqrt{3}}
\end{aligned} \tag{2.4}$$

The anti-symmetric amplitude is obtained by taking a difference between (1) and (3) :

$$\begin{aligned}
< K^-\eta_8|K^{*-} >_{\rm asym} &=< K^-\eta_8|K^{*-} > - < \eta_8 K^-|K^{*-} > \\
&= g(< \eta_8|u\,\bar{u} > - < \eta_8|s\,\bar{s} >) \\
&= g\sqrt{\frac{3}{2}} \\
< K^-\eta_1|K^{*-} >_{\rm asym} &=< K^-\eta_1|K^{*-} > - < \eta_1 K^-|K^{*-} > \\
&= g(< \eta_1|u\,\bar{u} > - < \eta_1|s\,\bar{s} >) \\
&= 0
\end{aligned} \tag{2.5}$$

Compared to the baryons, the hadronic decay of mesons is simpler since the mixing of these two couplings need not be taken into account because of the generalized C (charge conjugation) invariance. With this invariance, either symmetric (D-type) or anti-symmetric (F-type) type coupling is permitted according to the symmetric nature of mesons concerned. This general selection rule can be written by the form:

$$\begin{aligned}
C_a \cdot C_b \cdot C_c = 1 \quad &: \text{symmetric (D} - \text{type) coupling} \\
C_a \cdot C_b \cdot C_c = -1 \quad &: \text{antisymmetric (F} - \text{type) coupling}
\end{aligned} \tag{2.6}$$

for the two body decay of meson multiplet $M_a \rightarrow M_b + M_c$, where C_i is the charge conjugation parity for the i-th multiplet (M_i). The value of C_i can be defined in the SU(3) symmetry limit even for charged meson ($C^{-1}M_iC = C_iM^T$) and is equal to the charge conjugation parity of the neutral non-strage particles in a given multiplet.

Therefore, two body decay of the even spin resonance to the pseudoscalars is expressed by symmetric (D-type) amplitude. Substituting symmetric one (2.4) to (2.2) and using (2.3), the relative branching of even spin K^* states to $K\eta$ and $K\pi$ becomes :

$$R_{\rm even} = \frac{\Gamma(K^*_{\rm J=even} \to K\eta)}{\Gamma(K^*_{\rm J=even} \to K\pi)} = \frac{1}{9}(\cos\theta_p + 2\sqrt{2}\sin\theta_p)^2 \left(\frac{q_{K\eta}}{q_{K\pi}}\right)^{2J+1} \tag{2.7}$$

where J is a spin of K^*, $q_{K\eta}$ and $q_{K\pi}$ are the c.m. momenta of the final $K\eta$ and $K\pi$ states, respectively. The simple kinematic barrier factor is used to correct for the phase space difference between these two decays.

On the other hand, the decay branching ratio of the odd spin resonance is given by the anti-symmetric amplitude (2.5) . Substituting this amplitude to (2.2) and using (2.3), we get

$$R_{\rm odd} = \frac{\Gamma(K^*_{\rm J=odd} \to K\eta)}{\Gamma(K^*_{\rm J=odd} \to K\pi)} = (\cos\theta_p)^2 \left(\frac{q_{K\eta}}{q_{K\pi}}\right)^{2J+1} \tag{2.8}$$

It is noted that $R_{\rm even}$ is already suppressed by a factor of 9 in the unmixed case ($\theta_p = 0°$) compared to $R_{\rm odd}$, and the suppression is even greater when mixing is occured. The quadratic Gell-Mann-Okubo mass formula

$$\tan^2\theta_p = \frac{m_8^2 - m_\eta^2}{m_{\eta'}^2 - m_8^2}, \quad m_8^2 = \frac{1}{3}(4m_K^2 - m_\pi^2) = (0.56{\rm GeV/c^2})^2 \tag{2.9}$$

gives $\theta_p = -10°$,† while linear Gell-Mann-Okubo mass formula

$$\tan^2\theta_p = \frac{m_8 - m_\eta}{m_{\eta 3} - m_8}, \quad m_8 = \frac{1}{3}(4m_K - m_\pi) = (0.61{\rm GeV/c^2}) \tag{2.10}$$

gives $\theta_p = -23°$. $R_{\rm even}$ becomes quite small for these negative θ_p values. As will be reviewed in the next section, the mixing angle derived from the present experiments on various processes support the angle $\theta_p \simeq -20°$. For this angle the suppression of $R_{\rm even}$ is significant and almost completely vanishes. It is noted that $R_{\rm even}$ exactly vanishes at $\theta_p = -19.5°$. Contrary, $R_{\rm odd}$ is relatively insensitive to the mixing angle and the equation (2.8) predicts that the decay fraction to the $K\eta$ channel is approximately as large as the $K\pi$ decay mode except for the difference of kinematical factor. Therefore, substantial number of events from spin odd K^* states is expected in this channel.

† The negative sign is derived from off diagonal component of mass matrix.[8]

In particular, it is interesting and important to check on these drastic SU(3) predictions in the decay of the spin two $K_2^*(1430)$ and spin three $K_3^*(1780)$ resonances because of their large cross sections. The reaction

$$K^- p \to K^\circ \pi^- p,$$

which takes place via same non-charge exchange process as $K^- p \to K^- \eta p$, has been studied extensively[7] in $K\pi$ channel. In this reaction, spin two $K_2^*(1430)$ resonance is produced copiously and the clear signal is observed in the $K^\circ\pi^-$ effective mass distribution, and also spin three $K_3^*(1780)$ is rather well established. In this regard, studying $K\eta$ system compared with $K\pi$ system gives a good mean to check the SU(3) symmetry. In addition, since the production cross section of $K_2^*(1430)$ is known to be large, both observation or non-observation of this resonance in $K\eta$ system are expected to give the good information on the octet-singlet mixing angle in the pure hadronic decay of mesons.

2.2 The $\eta - \eta'$ mixing angle

The value of the $\eta - \eta'$ mixing angle has been the subject of the discussion since the SU(3) flavor symmetry is proposed. As have been described in the previous section, the quadratic and linear Gell-Mann-Okubo mass formule give two different angles of $\theta_p = -10^\circ$ and $\theta_p = -23^\circ$, respectively.

Historically, $\theta_p = -10^\circ$ has been taken by many authers [20,21,19]. This value is phenomenologically interesting because the "perfect mixing" [19] of η and η' states

$$\begin{aligned} |\eta> &= \frac{1}{\sqrt{2}}\left(\frac{1}{\sqrt{2}}(|u\bar{u}> + |d\bar{d}>) - |s\bar{s}>\right) \\ |\eta'> &= \frac{1}{\sqrt{2}}\left(\frac{1}{\sqrt{2}}(|u\bar{u}> + |d\bar{d}>) + |s\bar{s}>\right) \end{aligned} \tag{2.11}$$

gives the angle $\theta_p = -9.7^\circ$ near to $\theta_p = -10.0^\circ$. This expression is in good contrast with the fact that other well known vector ($J^{pc} = 1^{--}$) and tensor ($J^{pc} = 2^{++}$) mesons

can be expressed approximately by the ideally mixed states;

$$|\phi>, |f'> = |s\bar{s}>$$
$$|\omega>, |f> = \frac{1}{\sqrt{2}}(|u\bar{u}> + |d\bar{d}>). \tag{2.12}$$

However, recent experiments on the process $J/\Psi \to \gamma\eta(\eta')$ and the measurements of the $\gamma\gamma$ decay width of η , η' , π° mesons favor the mixing angle of $\theta_p \simeq -20°$. These evidences are summarized in the recent rewiew by Gilman and Kauffman [17]. According to this review, various values of mixing angle derived from the processes $J/\Psi \to \gamma\eta(\eta')$, $\eta, \eta' \to \gamma\gamma$, the reaction $\pi^- p \to \eta(\eta')p$ and the hadronic decay of the light meson are presented below.

$J/\Psi \to \gamma\eta(\eta')$

Assuming the decay $J/\Psi \to \gamma\eta$ and $J/\Psi \to \gamma\eta'$ occur primarily through the radiation of a photon from the charmed quark or charmed antiquark in the initial state, these decays proceed through the SU(3) singlet part of the pseudoscalar (i.e. η_1). This mechanism predicts the decay branching ratio:

$$\frac{\Gamma(J/\Psi \to \gamma\eta')}{\Gamma(J/\Psi \to \gamma\eta)} = \frac{1}{\tan^2\theta_p}\left(\frac{q_{\eta'}}{q_\eta}\right)^3. \tag{2.13}$$

The current experimental value [8] 4.8 ± 0.2 gives

$$\theta_p = -22° \pm 1° \pm 4° \tag{2.14}$$

$\gamma\gamma$ width

Using SU(3), the current algebra predicts the ratios of $\gamma\gamma$ widths [23] :

$$\frac{\Gamma(\eta \to \gamma\gamma)}{\Gamma(\pi^\circ \to \gamma\gamma)} = 18\left(\frac{m_\eta}{m_\pi}\right)^3 (F_\pi)^2 \left(\frac{\cos\theta_p(e_u^2 + e_d^2 - 2e_s^2)}{F_8\sqrt{6}} - \frac{\sin\theta_p(e_u^2 + e_d^2 + e_s^2)}{F_0\sqrt{3}}\right)^2 \tag{2.15}$$

and

$$\frac{\Gamma(\eta' \to \gamma\gamma)}{\Gamma(\pi^\circ \to \gamma\gamma)} = 18\left(\frac{m_{\eta'}}{m_\pi}\right)^3 (F_\pi)^2 \left(\frac{\sin\theta_p(e_u^2 + e_d^2 - 2e_s^2)}{F_8\sqrt{6}} + \frac{\cos\theta_p(e_u^2 + e_d^2 + e_s^2)}{F_0\sqrt{3}}\right)^2 \tag{2.16}$$

where e_u, e_d, e_s are charge of u, d, s quark, respectively. F_π, F_8 and F_0 are the decay constant of the pion, eighth component of the octet and singlet, respectively. The latest

experimental results are [8] :

$$\begin{aligned}\Gamma(\pi^\circ \to \gamma\gamma) &= 7.3 \pm 0.2 \quad \text{eV} \\ \Gamma(\eta \to \gamma\gamma) &= 0.56 \pm 0.04 \quad \text{keV} \\ \Gamma(\eta' \to \gamma\gamma) &= 4.16 \pm 0.30 \quad \text{keV}\end{aligned} \tag{2.17}$$

In the SU(3) limit of $F_8 = F_\pi$, these experimental values give:

$$\begin{aligned}\theta_p &= -20^\circ \pm 2^\circ \\ \frac{F_0}{F_\pi} &= 1.06 \pm 0.04\end{aligned} \tag{2.18}$$

On the other hand, if we take into account one-loop chiral corrections to F_8 and F_π, the above SU(3) relation is broken to $F_8 = 1.25F_\pi$ [23]. This result gives

$$\begin{aligned}\theta_p &= -23^\circ \pm 3^\circ \pm 1^\circ \\ \frac{F_0}{F_\pi} &= 1.04 \pm 0.04 \pm 0.05 \ .\end{aligned} \tag{2.19}$$

Both results are close to $\theta_P \sim -20^\circ$ and the values for F_0/F_π are unity within 10%.

$\underline{\pi^- p \to \eta(\eta')p}$

The SU(3) and nonet symmetry predict the ratio of the cross section at high energies:

$$\frac{\sigma(\pi^- p \to \eta' n)}{\sigma(\pi^- p \to \eta n)} = \left(\frac{\sqrt{2} + \tan\theta_p}{1 - \sqrt{2}\tan\theta_p}\right)^2 \tag{2.20}$$

One experimantal group [24] finds for this ratio to be 0.55 ± 0.06, which implies a mixing angle of $\theta_p = -18^\circ \pm 1.4^\circ$. Another group[25] finds 0.67 ± 0.03, yielding $\theta_p = -15^\circ \pm 1^\circ$. Although there is some disagreement over the experimental values, the results distribute somewhere between $\theta_p \simeq -10^\circ$ to $\theta_p \simeq -20^\circ$.

hadronic decay of light meson

Among the strong decay of light mesons involving η, we consider two decay processes of $f \to \eta\eta$ and $a_2 \to \pi\eta$.

First we consider the decay $a_2 \to \pi\eta$. SU(3) and nonet symmetry leads to the prediction:

$$\begin{aligned} \frac{\Gamma(a_2 \to \pi\eta)}{\Gamma(a_2 \to KK)} &= \frac{2}{3}(\cos\theta_p - \sqrt{2}\sin\theta_p)^2 \left(\frac{q_{\eta\eta}}{q_{\pi\pi}}\right)^5 \\ &= \begin{cases} 2.83 & (\theta_p = -10^\circ) \\ 2.76 & (\theta_p = -23^\circ) \end{cases} \end{aligned} \tag{2.21}$$

The experimental value [8] of this ratio is 2.96 ± 0.54. This value is slightly favor for $\theta_p \sim -10^\circ$ but cannot ruled out $\theta_p \sim -20^\circ$ due to the experimental error.

Secondly, the same symmetry predicts for the decay $f \to \eta\eta$:

$$\begin{aligned} \frac{\Gamma(f \to \eta\eta)}{\Gamma(f \to \pi\pi)} &= \frac{1}{27}(\cos\theta_p - \sqrt{2}\sin\theta_p)^4 \left(\frac{q_{\eta\eta}}{q_{\pi\pi}}\right)^5 \\ &= \begin{cases} 3.2 \times 10^{-3} & (\theta_p = -10^\circ) \\ 6.6 \times 10^{-3} & (\theta_p = -23^\circ) \end{cases} \end{aligned} \tag{2.22}$$

The experimental data are somewhat conflicting. Binon et al.[27] gives $BR(f \to \eta\eta) = (5.2 \pm 1.7) \times 10^{-3}$ which implies $\theta_p \simeq -20^\circ$, while D.Alde et al. [28] measures $BR(f \to \eta\eta) = (2.3 \pm 0.8) \times 10^{-3}$ which favors $\theta_p \simeq -10^\circ$.

These hadronic decays are qualitatively well described by a simple SU(3) relations,† but the mixing angle is not well determined and unable to distinguish between $\theta_p \simeq -10^\circ$ and $\theta_p \simeq -20^\circ$.

In this chapter, I have reviewed SU(3) predictions on the $K^* \to K\eta$ decays and the current experimental situation on the value of $\eta - \eta'$ mixing angle for various processes. I have shown that, if the SU(3) symmetry is also satisfied for the $K^* \to K\eta$ decays, the feature of these decays should be drastically depend on their spin. The significant enhancement is expected for the $K\eta$ decay of odd spin K^* and large suppression is

† As a check of SU(3) and the kinematical barrier factor in the hadronic decay for the tensor meson, we note that the prediction of f meson decays

$$\frac{\Gamma(f \to KK)}{\Gamma(f \to \pi\pi)} = \frac{1}{3}\left(\frac{q_{KK}}{q_{\pi\pi}}\right)^5 = 0.036 \tag{2.23}$$

is in excellent agreement with the experimental value[8] of 0.034 ± 0.003.

expected for the decay of even spin K^*. These decay rates also depend on the $\eta - \eta'$ mixing angle. The current experiments on the various processes support the value $\theta_p \simeq -20°$ for thr mixing angle, although there is no clear distinction of the value between $-10°$ and $-20°$ in the experimental data of the hadronic decays of light mesons. If we accept the favourable angle $\theta_p \simeq -20°$, the $K\eta$ decay of even spin K^* is almost completely suppressed.

The results of the experimental check on this drastic predictions for the $K^* \to K\eta$ decays are reported in the following chapters.

3. The LASS spectrometer

The **LASS** spectrometer (fig.7) was designed and constructed at Stanford Linear Accelerator Center(SLAC) for high statistics studies of high multiplicity hadronic interactions. It consists of a large superconducting solenoidal vertex detector followed by a high resolution dipole spectrometer. These combination of the Solenoid and Dipole spectrometer provide an almost 4π acceptance with fairly good momentum resolution. This is one of the characteristic of this spetrometer compared to another forward arm spectrometers, and this feature is essential in the analysis of the reaction (1.1)because it is necessary to reconstruct π° as missing particle.

The 11 GeV/c kaon beam is provided from the SLAC beam line. The RF separators in this beam line reduce the pion contamination to 1/60 of the kaon. These kaon beam particles are tagged by means of two Cerenkev counters, resulting very clean kaon beam with a purity of $\geq 99.99\%$. The momentum and the directon of kaon beam are measured by scintillation counter hodoscope and 10 planes PWCs with 1 mm wire spacing. The beam momentum is measured with an accuracy of 40 MeV/c.

The solenoid magnet provides a 22.4 KG field parallel to the beam direction. In the solenoid region 6 layers of cylindrical chambers surround the target, and 6 layers of large planar PWCs are located at the down stream of the target. In the beam region, 3 layers of PWCs with 1mm wire spacing are equipped to cover the deadened region of large planar chambers. It is possible to reconstruct the events with high multiplisity more than 10 in this solenoid spectrometer.

The momenta of fast tracks produced with small angle respecting to the beam axis are measured by the dipole spectrometer located downstream. Track reconstruction in the dipole parts are performed by the dipole magnet and 7 layers of magnetostrictive readout spark (MS) chambers. The dipole magnet provides a vertical magnetic field with field integral 30.1 kGm. Two small PWCs also cover the hot region around the beam axis in the MS chambers to avoid the acceptance hole. The large scintillator hodoscopes (HA,HB) are used to provide the on-time information. The momentum resolution of the dipole spectrometer is fairly good and is presented as :

$$\left(\frac{\sigma_p}{p}\right) = 6.53 \times 10^{-4} \cdot p + 1.15 \times 10^{-3} \qquad (3.1)$$

(p in GeV/c)

The momentum resolution for $p = 10\text{GeV/c}$ particle is $\sigma_p \sim 75\text{MeV/c}$.

As particle identification devices, two threshold type Čerenkov counters $\check{C}_1$, $\check{C}_2$ and TOF hodoscope systems are equipped. The effective threshold momenta of the Čerenkov counters for pion are $\sim$ 2.9 and $\sim$ 3.0 GeV/c in $\check{C}_1$ and $\check{C}_2$, respectively. The efficiency attained are 99.8 % ($\check{C}_1$) and 99% ($\check{C}_2$). TOF system consists of 24 azimuthally segmented scintillator array. The distance between the target center and this TOF counter is about 500 cm. Typical time resolusion of TOF system is 530 psec. In the data sample of $K^-p \to K^-\pi^+\pi^-\pi^\circ p$ candidate, π/p, π/K separation are possible up to $\sim$ 2.3GeV/c and $\sim$ 1.1GeV/c, respectively. In addition, the cathode pulse height from cylindrical chambers provides dE/dx information capable to separate π/p of slow momentum up to $\sim$ 0.8GeV/c.

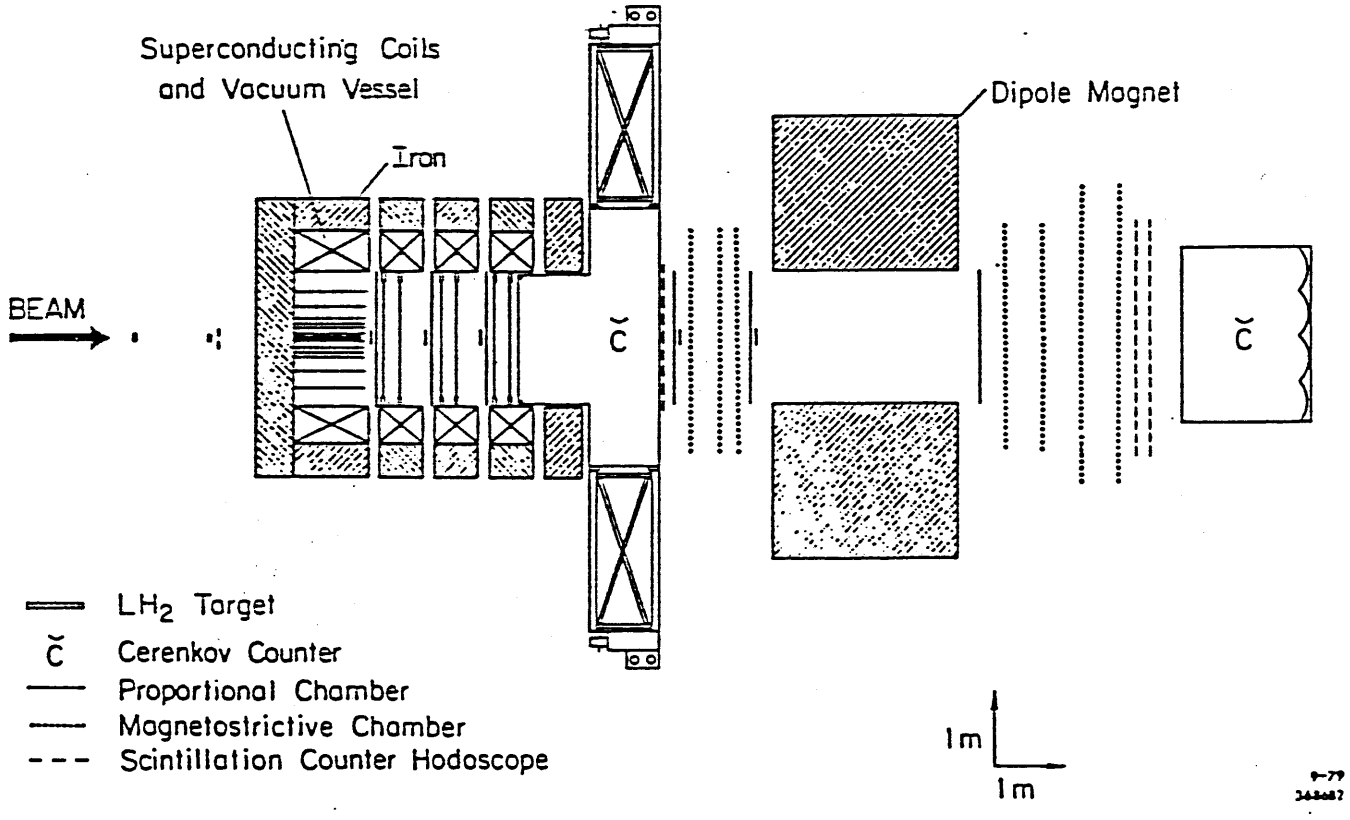

Fig.7 The schematic view of the **LASS** spectrometer

In the following section, some detail of each components in this spectrometer will be described. More detailed description of the spectrometer is given elsewhere [26].

3.1 The beam line

The 11GeV/c kaon beam is provided as secondary particles produced by 21 GeV/c electron beam of the SLAC. This primary electron beam has 1.6μ sec bunch width with maximum repetition rate of 180 Hz. This electron beam is steered on the primary target consist of berylium and copper with radiation length of 0.87,0.25, respectively.

The secondary particles produced on the target with production angle of $1° \pm$ 3.85 mrad are captured in this beam line (fig.8). This secondary beam is focussed at various points F1-F4 on the beam line. Two RF separators located between F1 and F4 enrich the kaon particles. The contamination of pions or protons are reduced to $\pi/K = 1/60, p/K = 1/55$ by these separators.

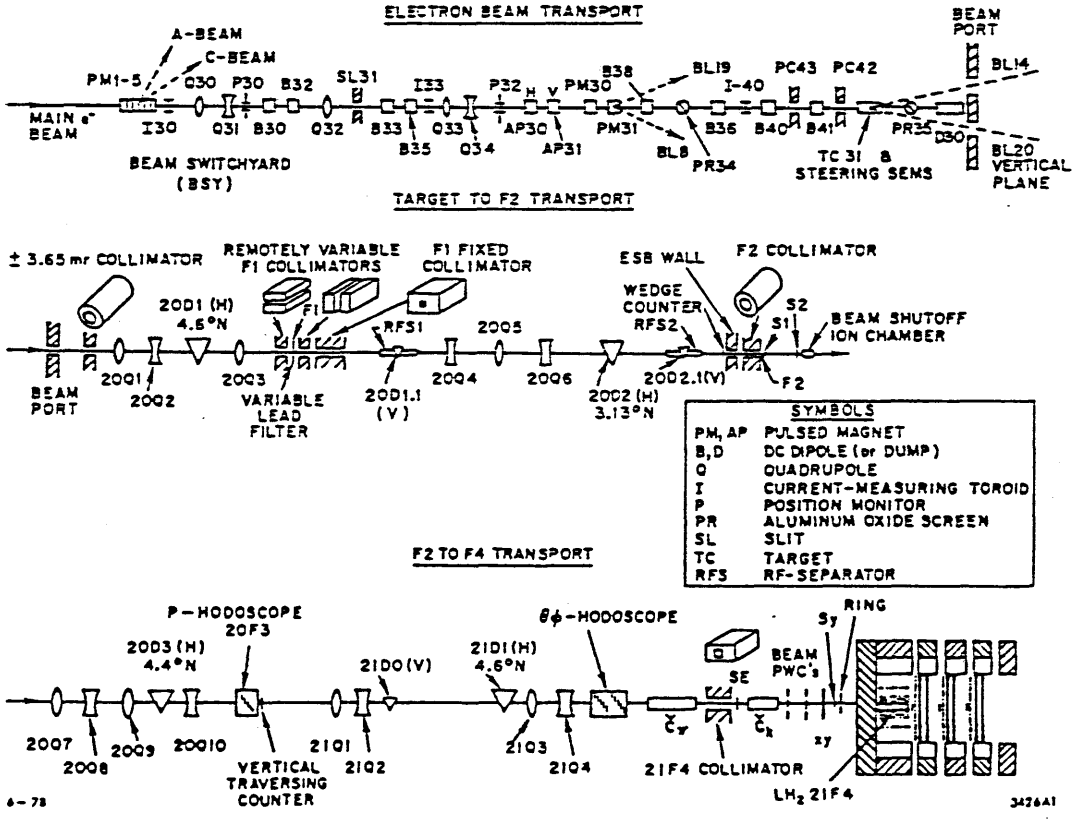

Fig.8 A schematic representation of LASS beam line

The momentum of each beam particle is determined by P-hodoscope. It consists of six overlapped finger scintillation counters, which digitize the beam position to 11 bins. Each bin is 0.61cm wide and is equivalent to a momentum bin width $\frac{\sigma_p}{p} = \pm.25\%$. In the nominal 11 GeV/c operation, the beam momentum measured in the n − th bin is given by $p = 10.600 \pm 0.0495\text{n}$ GeV/c . The overall beam momentum resolution is calibrated to be 0.040GeV/c by the dipole spectrometer.

The spatial position of each beam particle is roughly measured by $\Theta\Phi$ hodoscope and beam trajectory is tracked by Beam PWCs located 1.2m upstream of the Solenoid magnet. $\Theta\Phi$ hodoscope consists of 2×12 array of 1.27 cm wide plastic scintillators. Θ hodscope measures holizontal position and Φ measures the vertical position. The Beam PWCs consist of 10 sets of PWCs with 1.016 mm wire spacing, which are grouped in two packages separated by 1 m. In each group, x, y, e and p coordinates ($e \equiv (x-y)/\sqrt{2}, p \equiv (x+y)/\sqrt{2}$) are measured. The beam direction is determined with the accuracy of 0.3 mrad by these Beam PWCs.

The identification of K beam particles is performed by two threshold Čerenkov counters $\check{C}_\pi$ and $\check{C}_K$ located downstream of Θ, Φ . $\check{C}_\pi$ is a 6 meter long counter filled with H_2 gas at 40 psia, while $\check{C}_K$ is 1.28 m long and filled with CO_2 gas at 75 psia. 11GeV/c pion generates Čerenkov light in both devices, while kaon produces the signal only on $\check{C}_K$. Combining RF separator and these Čerenkov counters, K beam with the purity of $\geq$ 99.99% is obtained.

The final component of the beam line are three scintillators called SE,SY and RING counters. SE counter (0.952 cm thickness) counts beam particles for normalization purpose and also used to provide the starting timing for the TOF system. SY counter (0.318 cm thick, 2.54 cm diameter ring counter) is used to define the beam profile. RING counter is 1.27 cm thick paddled counter having 2.54 cm diameter hole in the middle, which is used to veto the beam halo.

Typical number of beam particles defined by the system usable in the **LASS** spectrometer was 3-5 per bunch. The beam repetition rate was between 60 to 120Hz.

The target

The liquid H_2 is contained in an appendix with 85.04 cm long and 2.54 cm in radius measured in a room temperature. The lenght at liquid H_2 temperature ($\sim 20K°$) is

$\sim$ 84.6cm . The target is wrapped by mylar sheets and is contained in an aluminum vacuum jacket having a wall thickness of 0.71 mm. The material around the target is limited such that protons with momenta $\geq$ 0.225GeV/c could be go out normal to the beam axis.

3.2 The Solenoid Spectrometer

The Solenoid Magnet

The superconducting solenoid magnet provides a field of 22.4 KG parallel to the beam axis. The inner diameter of the magnet is 185 cm and its overall length is 465 cm. This magnet consists of four separate superconducting coils so that planar chambers can be inserted. The uniformity of the magnetic field B_z (parallel to the beam axis) is $\pm 1\%$ and B_φ, B_r components are uniform within 3.1% in the fiducial volume of $r \leq$ 75cm and $0 \leq z \leq$ 320cm . The field in the magnet volume is mapped every 2.54 cm in the Z direction.

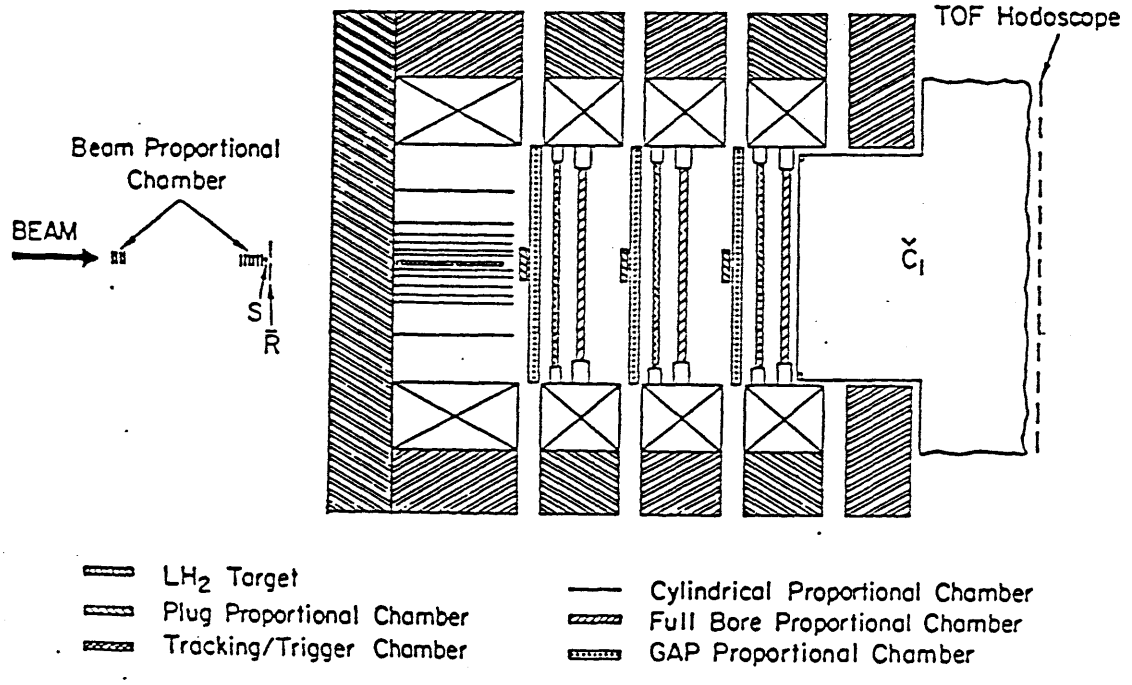

Fig.9 The Solenoid Spectrometer

The Cylindrical Chambers

The target is coaxially surrounded by six layers of cylindrical proportional wire chambers (Fig.- 9). The innermost and outermost radius are 6.05 cm and 49.02 cm, respectively. In each layer, anode wires are strung parrarel to the cylinder axis in 2.00 mm pitch. These anode wires are sandwitched by 2 cathodes, which are made of strip line oriented $\pm 10°$ to the anode wire in inner 4 cylinders and $\pm 15°$ for outer 2 cylinders. The active length is 100 cm for cylinder 1 through 4, and 87 cm for 5,6. The cylinder consists of paper honeycomb and double aluminum mylar laminate cathode foils, resulting small amount of materials in each cylinder ($\sim 0.11 gm/cm^2$). The physical dimentions of the cylindrical chambers are summarized in table-1.

The typical chamber efficiency is $\sim 98 - 99\%$ and cathode spatial resolutions are $\sim 200\mu$ as shown in table-2.

Table-1: The physical dimentions of the cylindrical chambers.

Cylinder Number	Anode Radius (cm)	No. of Anode Wires	Anode/Cathode Gap (mm)	Cathode Pitch (mm)	No. of Strips on (inner)	No. of Strips on (outer)	Stereo Angle
1	6.05	190	4.78	5.00	70	82	10°
2	9.55	300	4.78	5.00	114	126	10°
3	12.99	408	5.09	8.00	98	106	10°
4	16.55	520	5.09	8.00	126	134	10°
5	29.41	924	5.77	10.35	175	182	15°
6	49.02	1540	5.77	10.35	294	301	15°

Table-2: The Cathode spatial resolution of cylindrical chamber.

Cylinder Number	cathode resolution (μm)	Z resolution (μm)
1	175.	700.
2	155.	620.
3	195.	780.
4	185.	740.
5	220.	580.
6	220.	580.

The Solenoid Planar Chambers

The downstream of the target in the Solenoid Magnet is covered with three kind of PWC chambers. 3 layers of GAP chamber, 3 layers of PLUG chambers and 3 layers of full bore chambers (called N.5 chambers).

GAP chambers

The GAP chambers are PWC with anode and cathode readout (Fig. 10). The wire spacing of the anode is 2.032 mm and two cathode planes consist of 6.86 mm wide separated 1.27 mm strips etched into aluminum mylar sheet. The strips are rotated $\pm 45°$ with respect to vertical anode wire. This arragement makes it possible to provide the unique space point by one chamber plane. The anode wires ($\sim$ 1.5m length 20μ diameter gold-plated tungsten) are held by a pair of insulated support wires stretched perpendicular to the anode. The spacial resolution of the cathode is $\sim 200\mu$m .

In these chambers, the central region around the beam axis with a radius of 8.255 cm is deadened by a mylar sheet with stylofoam supports. This prevents the tracks in the high intensity beam region from producing the unnessesary and disturbing signal on cathode strip. This deadened region is completely covered by the following PLUG chambers.

PLUG chambers

1 mm wire spacing PLUG chambers are located on the beam axis where the instantaneous particle flux is high. Five PLUG chambers are used in **LASS** . The first three PLUG chamber completely cover the deadened area of GAP chambers, while the remaining chambers cover similarly deadened area of three MS chambers in the TWIXT region(the region between solenoid and dipole magnet). One PLUG chamber has 3 anode planes which provide the information of x, y and e coordinates ($e \equiv x\cos\theta - y\sin\theta$ with $\theta = 35°$).

Full-Bore Chambers

The full-bore chambers (fig. 11), labelled with the 1.5, 2.5 and 3.5 chambers, are planar PWCs with anode wire spacing of 2.032 mm, which are mounted in the inner bore of the solenoid magnet coil. Each chamber consists of three anode planes oriented y, x and e cooridinates. ($e \equiv x\cos\theta - y\sin\theta$ with $\theta = 45°$) . The chamber frame

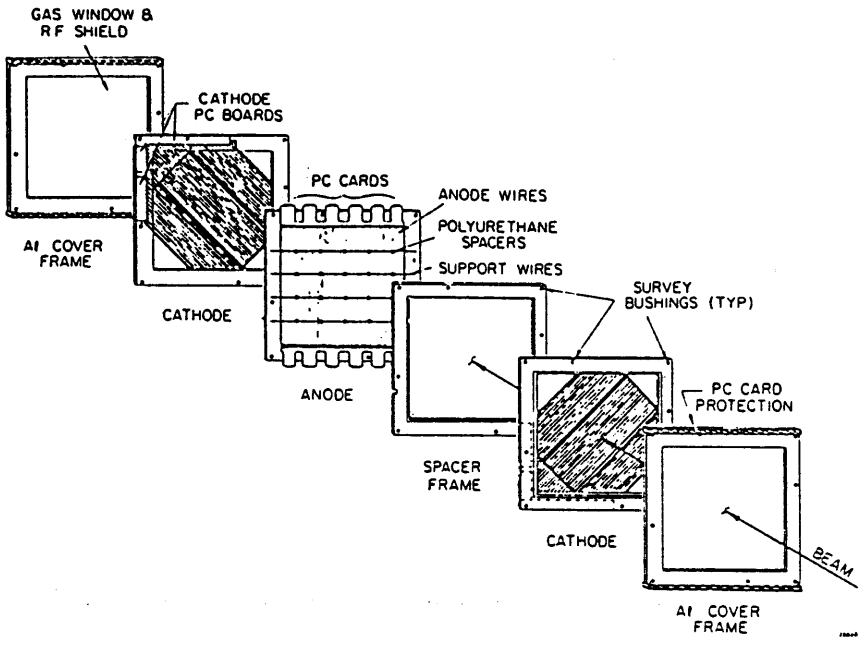

Fig.10 An assembly of a GAP chamber

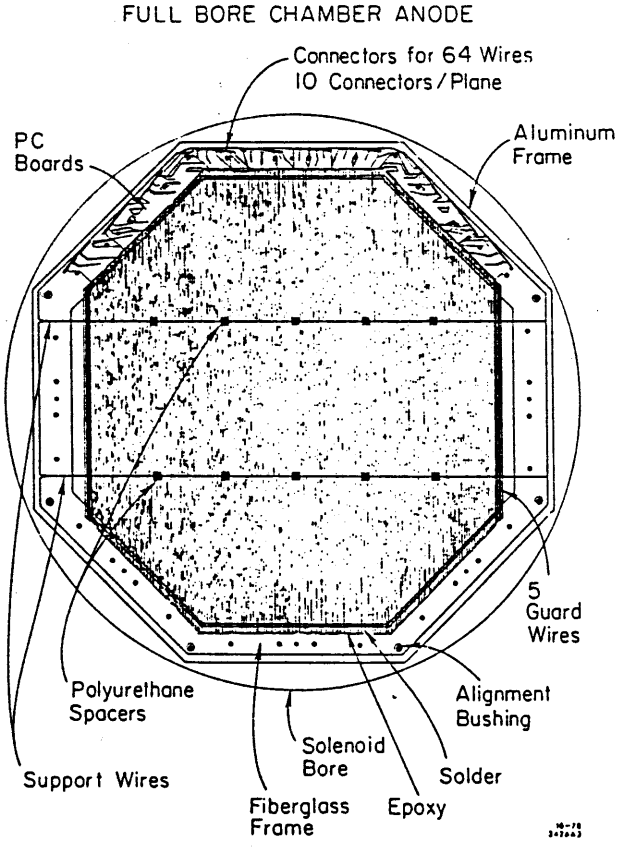

Fig.11 A schematic of a full-bore chamber

is octagonal in shape so that to cover as much of the solenoid bore as possible. The diameter of active area is approximately 141 cm.

3.3 The Dipole spectrometer

The dipole spectrometer measures the momenta of particle produced within 50 - 100 mrad of the beam axis with momenta $p \geq 1.5\text{GeV/c}$. The configuration is shown in fig.12.

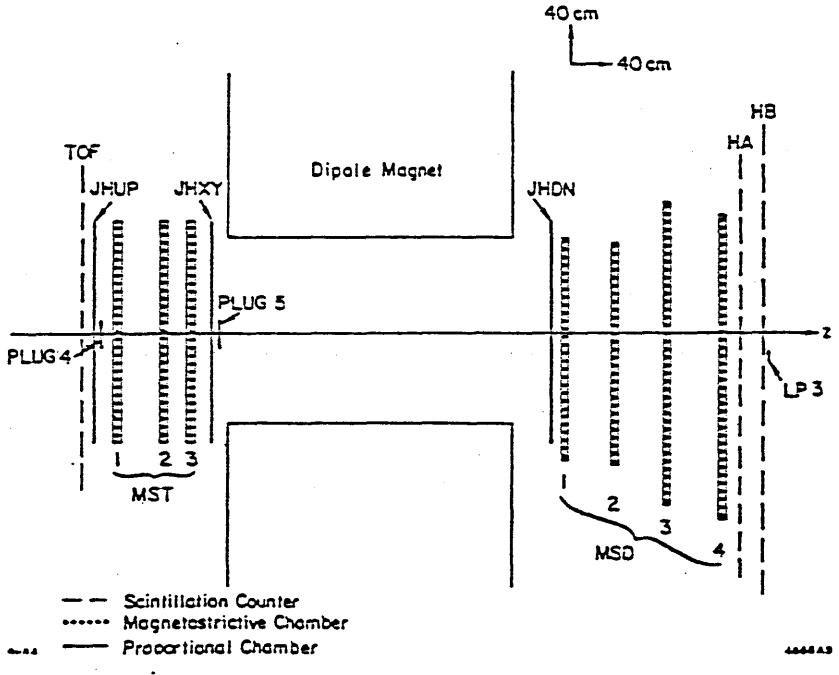

Fig.12 The schematic view of the dipole spectrometer

The Dipole Magnet

The Dipole Magnet is a conventional water-cooled magnet having an apeture of 185cm(H) × 102cm(V). (holizontal × vertical). The magnetic field is oriented to the vertical direction and the maximum strength is 18KG at full excitation(7050 A), which corresponds to a total field integral along the z-axis of 30.1 KG · m. The 11 GeV/c particle is kicked by this field approximately 90 miliradian. (The half of the experiment was performed by 2/3 field integral because of budget constraint.)

The Magnetostrictive Spark Chamber

Seven magnetostrictive readout spark chambers (MS chambers) are used in the

dipole spectrometer. Three are at the region between solenoid and dipole magnet (TWIXT region) and four are at the downstream of the dipole magnet. Five of these chambers have effective area of 150 × 300 cm and other 2 have larger effective area of 200 × 400 cm. Each MS chamber provides x,y, e and p coordinate informations, where $e \equiv x\cos\theta - y\sin\theta$ and $p \equiv x\cos\theta + y\sin\theta$. The stereo angle θ is ± 30° for five MS chambers and ± 25° for two large chambers.

The readout of the coordinate is performed with magnetostrictive wand line . Two or three fiducial wires are placed on each wand line. The time arrival of each pulse is digitized by a time digitizer circuit called ANNA module with a 20 MHz clock. This implies a wand coordinate digitization by $\sim$ 0.027 cm for typical wand lines. The spacial resolution of the MS chamber is 0.5 $\sim$ 1.0 mm.

The twixt region is suffered by strong stray field of solenoid magnet. To minimalize the effect of this magnetic field on MS wand, each wand in the twxit MS chamber is wound by a coil and is pulsed with a current of 10-30 A during the beam spill to cancel out the field effect. However, the MS chambers in the twixt region still have lower efficiency relative to the downstream chambers. A typical efficiency of each plane is 0.70 - 0.85 for twixt chambers and 0.95 for down stream chambers.

The Scintillator Hodoscopes HA,HB and LP3

Two large scintillator hodoscope arrays, HA and HB, are located right behind the MS chambers. These counters are consisted with paddles of scintillators contacting at the center, as shown fig.13. The HA hodoscope consists of 2 × 21 paddles, having dimensions of 20.32 cm × 83.82 cm except center paddle. The dimension of center paddles are 10.16 cm × 83.82 cm . The HB array consists of 2 × 38 paddles. The center 24 paddles have dimensiones of 10.16 cm × 83.82 cm . The outer 14 paddles have dimensiones of 15.24 cm × 83.82 cm . Both HA,HB hodoscope are arranged to form a 10.16 cm × 10.16 cm hole at the center.

A circular counter with a radius of 9.84 cm, called LP3, covers the beam hole in the HA and HB. It is used to veto the non-interacting beam particles in the event trigger logic.

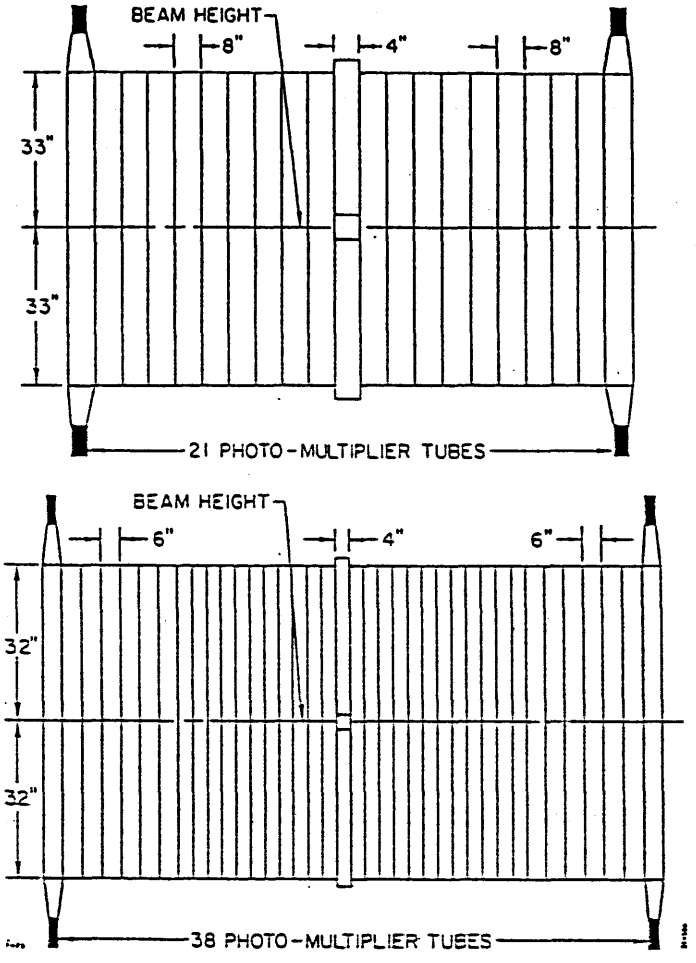

Fig.13 The HA and HB counter hodoscopes

3.4 The Čerenkov Counters

LASS has two threshold type Čerenkov counters named $\check{C}_1$ and $\check{C}_2$. $\check{C}_1$ Čerenkov counter is located at the downstream of the solenoid magnet while $\check{C}_2$ counter is situated at the tail end of the **LASS** spectrometer.

The $\check{C}_1$ counter

Freon 114 gas is filled in $\check{C}_1$ at atmospheric pressure. The momentum threshold for π and K are $\sim$ 2.6GeV/c and $\sim$ 9.2GeV/c, respectively. The length of the gas radiator is $\geq$ 180 cm.

This counter is segmented into 38 optically isolated cells, which enables this counter to identify a particle in a multi-particle enviroment. The segmentation of the $\check{C}_1$ counter

is shown in fig.14. The counter is segmented into four ring named D,C,B,A ring in the order of increasing radius. Each ring is further divided in azimuth into 2 for D ring, and 12 cells for B, C and A ring. The partition is achieved with vacuum depositioned aluminum mylar sheets. At the downstream end of each cell, Čerenkov light is reflected normal to the beam axis into an optical assembly consisting of a plastic Fresnel lens, a light collecting horn and a RCA 8850 Quantacon photomultiplier (fig.15). This photomultiplier has good single photo-electron response. Because of the large stray magnetic field in this region, the phototubes are carefully shielded with a set of iron pipe and μ-metal.

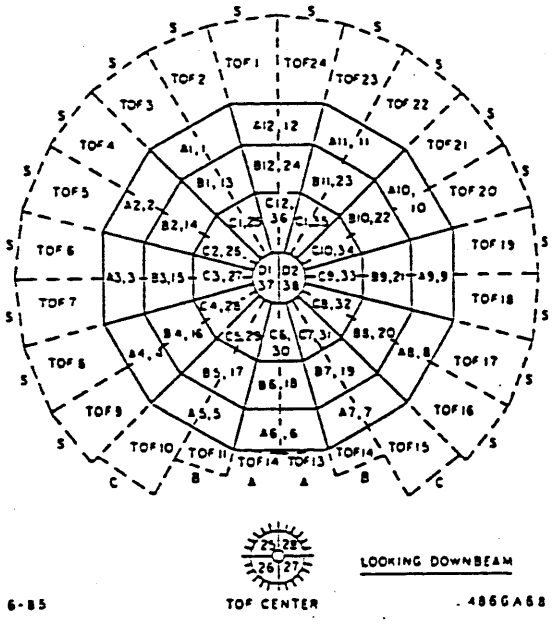

Fig. 14 A schematic representation of $\check{C}_1$ Čerenkov counter. The TOF hodoscope located immediately downstream are also shown by dashed lines.

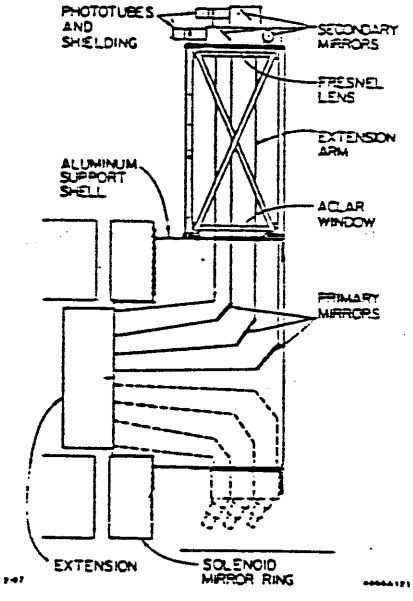

Fig. 15 The mechanical structure of the $\check{C}_1$ Čerenkov counter: A cross section of the $\check{C}_1$ arm showing the light collection path.

Since the optics of $\check{C}_1$ counter is rather complicated, the performance of the $\check{C}_1$ counter is a function of particle trajectory inside the counter. The precise efficiency as a function of position, direction of the particle and momentum is mapped by using a large sample of $\pi^{\pm}$ in the decayed daughter of K°. The efficiency curve is shown in fig.16. Marginal particles which passes within 3 cm of a cell boundary and the lower three inefficient cells of the bottom quadrant have been excluded in this measurement. The asymptotic efficiency are $0.971 \pm 0.006, 0.987 \pm 0.002$ and 0.998 ± 0.002 for A,B

and C ring respectively. The effective momentum threshold for π, which gives efficiency better than 0.95, is $\sim$ 3.0GeV/c.

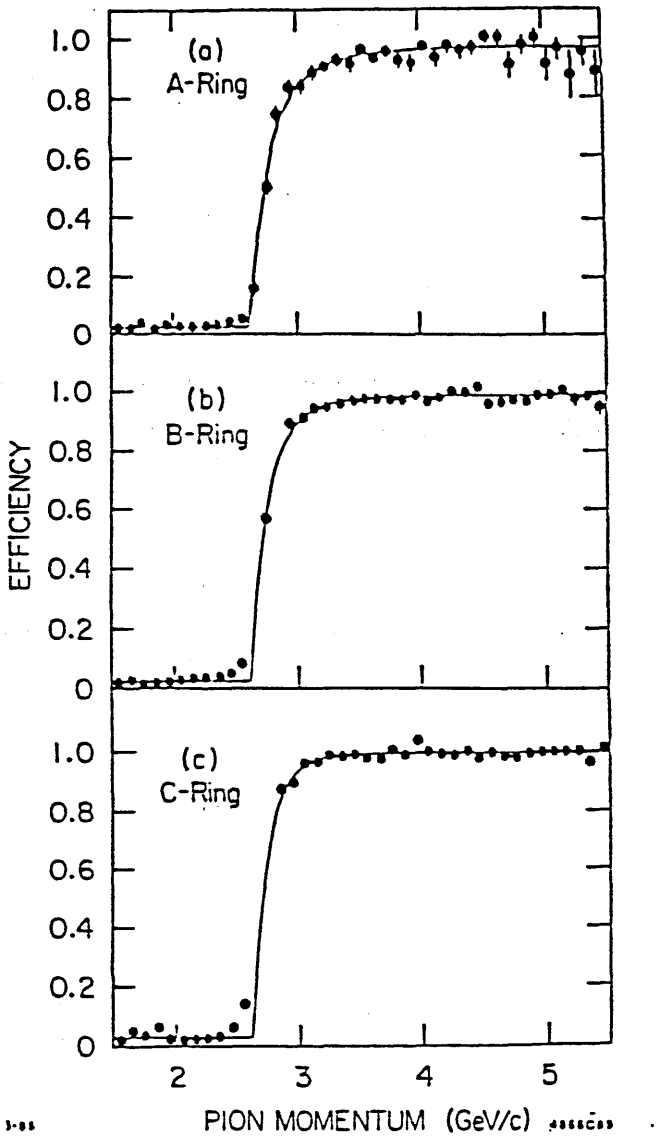

Fig.16 The efficiency curve for the three rings of $\check{C}_1$. This curve is obtained using pure smaple of $\pi^{\pm}$ identified as decayed daughter of K° .

The $\check{C}_2$ Čerenkov counter

Freon 12 (CCl_2F_2) is filled at 1.2 atmospheric pressure in $\check{C}_2$. The length of the radiator is 175cm. The Čerenkov photons are reflected by one or more of eight mirrors located at the back of the counter (fig.17). Those photons are focussed by the light "horns" onto the photocathode of a photomultiplier XP2041. The phototube which is sensitive to UV photons are used since intensity of Čerenkov radiation is proportional

to $1/\lambda^2$.

The asymptotic efficiency of the counter is 99 % and the effective pion threshold momentum is $\sim$ 3.0GeV/c.

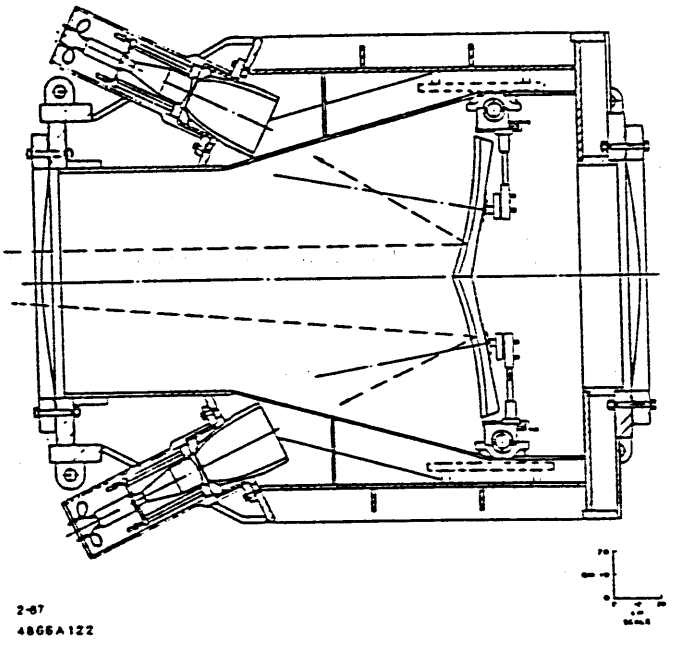

Fig.17 A side view of $\check{C}_2$ Čerenkov counter.

3.5 The TOF system

The TOF counter system (fig.18), is located at z=573 cm immediately downstream of $\check{C}_1$ counter. The TOF system consists of 1 cm thick 24 paddle shaped scintillators. Each scintillator is viewed from one end by phototube through a lucite light guide having a Winstone cone shape light collector. Because of the large leakage field of solenoid ($\sim$ 600 Gauss), each phototube is shielded by two layers of steel and μ-metal with bucking coil, and phototude axis is set approximately perpendicular to the magnetic field.

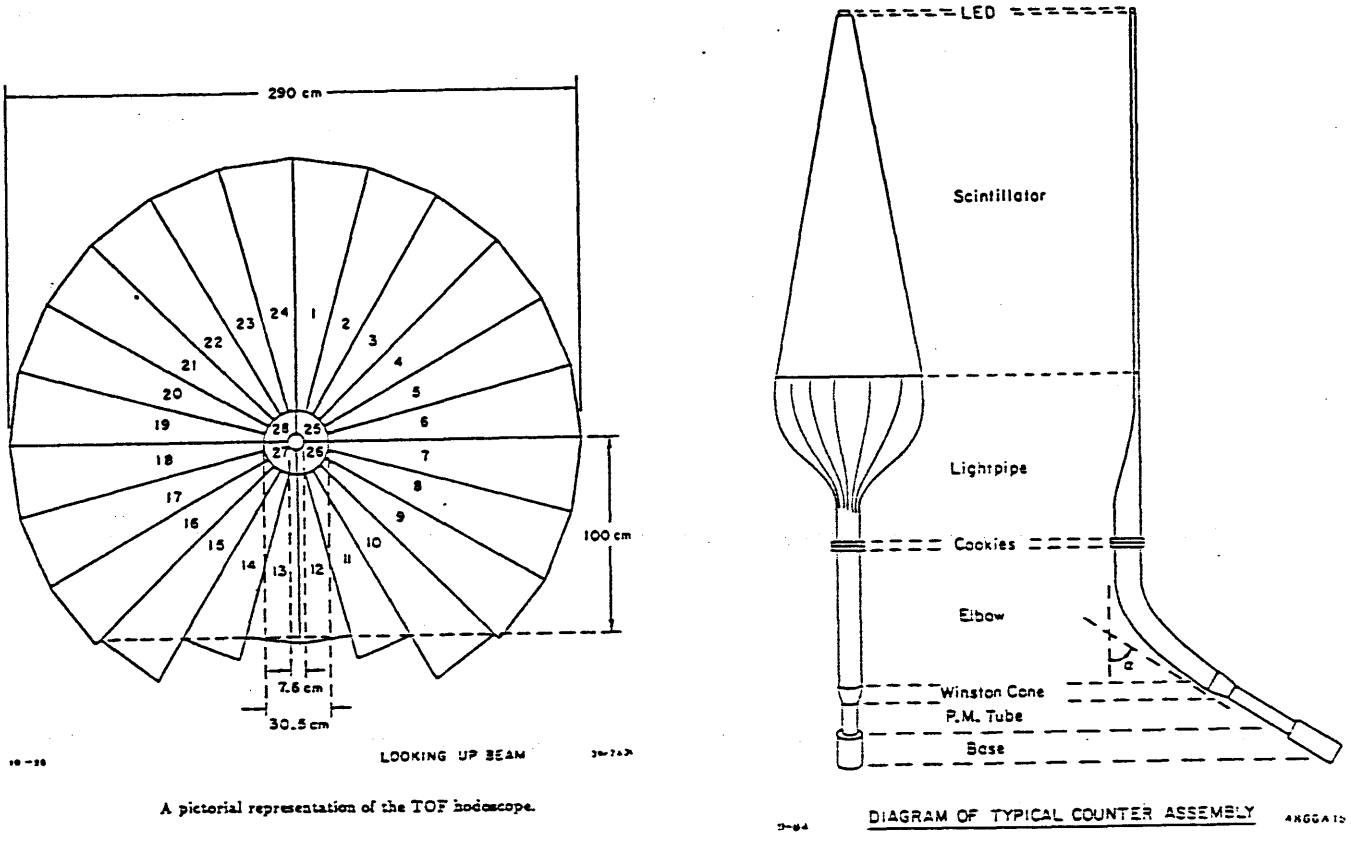

A pictorial representation of the TOF hodoscope.

Fig.18 A beam view of the TOF hodoscope.

The phototube output is discriminated and used as a stop signal of TDC. The start timing is provided by SE counter in the beam line. The pulse height of the TOF counters and SE counter are also measured to correct the time walk due to the variation of pulse height.

The conversion of the observed TDC value into measured time t_{meas} and various corrections are performed with the following formula:

$$t_{meas} = \alpha_1 TDC - \alpha_2 - \frac{\alpha_3}{\sqrt{ADC_{SE}}} - \frac{l}{v} - \frac{\alpha_4 + \alpha_5 l}{\sqrt{ADC_{TOF}}} - \alpha_6 l^2 - \alpha_7 l^3 \qquad (3.2)$$

In this expression, l is light path in the scintillator; v is effective velocity of light in the scintillator ; the α_j are constants to be determined from the data and ADC_{SE}, ADC_{TOF} are the measured ADC value of SE and TOF counters. The terms involving ADC_{SE}

and ADC_{TOF} correct time walk of these counters due to variations of the pulse height, and l^2, l^3 terms provide a position dependent correction for the internal optics of the TOF counters.

The parameters in this formula are determined using a sample of fast ($p \geq 3$GeV/c) negatively charged tracks. The obtained time resolution of the TOF system is listed in table-3.

Table-3: The time resolution of the TOF system.

TOF No.	Resolution (psec)	TOF No.	Resolution (psec)
1	605	13	422
2	521	14	437
3	710	15	392
4	580	16	551
5	675	17	534
6	510	18	516
7	631	19	506
8	427	20	564
9	501	21	512
10	445	22	601
11	458	23	547
12	504	24	490

With this configulation of the TOF system, the separation of π /K is possible upto $\sim$ 1.1GeV/c and π/p separation is possible upto $\sim$ 2.3GeV/c .

3.6 Ionization measurements in the cylindrical PWC

The primary design criteron for cylindrical chambers was focussed on efficiency for multi-particle detection. For this purpose, "magic gas" mixture (20 % Isobutane, 4 % Methylal, 0.5 % Freon 13B1 and balanced Ar) is used to operate these chambers in a partially saturated mode. However, it is found that a significant particle discrimination between proton and π or K is still attainable in momenta below $\sim$ 0.8GeV/c if we carefully calibrate the pulse height. Here we discuss the method of the calibration of the pulse height and its performance of particle discimination.

Calibration procedure

The calibration of the pulse height of the cathode strips in the cylindrical chambers are, at first, perfomed using relativistic ($\beta \geq 0.9$) negative charged particles. This provides a 95 % pure sample of pions. Using this sample, incident angle θ dependence and gain variation in each cathode are corrected run by run basis.

After making these corretions, β dependence of the pulse height is calibrated using the pure proton sample in the Kp elastic events. The measured pulse height shows well known Landau distribution (fig.19-a). However, the measured pulse height raised to the 0.3 power are found to be reasonably Gaussian. (see Fig.19-b). The mean of the Gaussian distribution as a function of β is shown in Fig.20. A clear β dependence is seen.

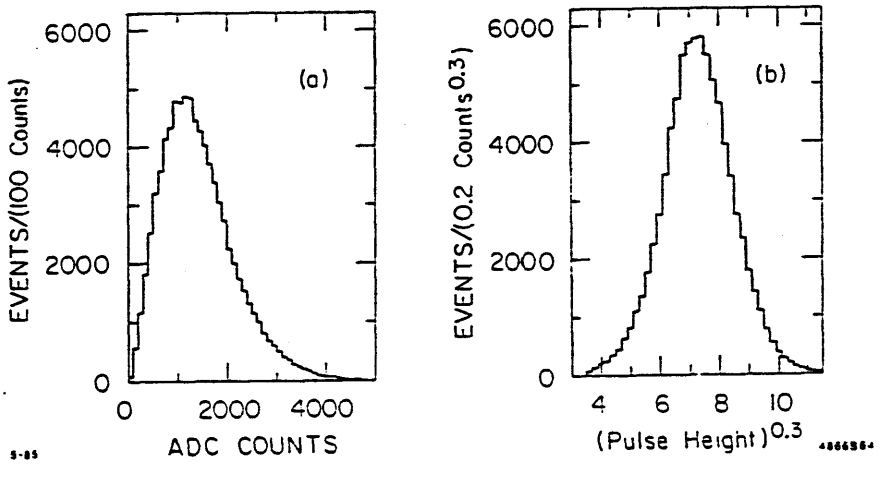

Fig.19 (a) The distribtion of the cathode pulse height in cylindrical chamber. (b) The distribution of the pulse height raised to the power 0.3

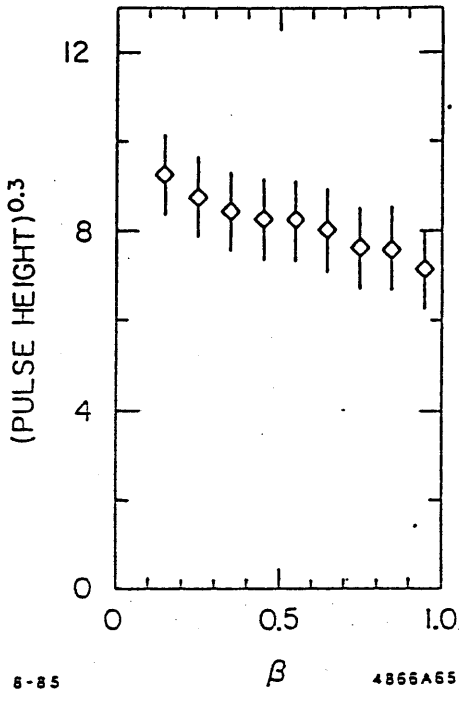

Fig.20 The mean of the pulse height distribution raised to the power 0.3 for one cylinder as a function of β

Discrimination Procedure

The probability (η_i) that a track is a proton or pion is determined using this Gaussian distribution:

$$\eta_i = \frac{1}{\sqrt{2\pi}\sigma} exp\left\{-\frac{1}{2}\cdot\left(\frac{\rho_M - \rho(\beta_i)}{\sigma}\right)^2\right\}, \tag{3.3}$$

where ρ_M is the expected mean value of the pulse height raised 0.3 power distribution calibrated by protons in Kp elastic events and σ is the standard deviation of this distribution and $\rho(\beta_i)$ is measured pulse height raised 0.3 power for a track to be known and i is an index of proton or pion. Using measured momentum, β_i is calculated for each of the mass hypothesises of proton or π to obtain the particle probability: η_i. This probability is determined in each cathode at first and then multiplied together for all the contributing cylinders.

To illustrate the results of this procedure, fig.21 shows the scatter plot of the logarithm of the likelihood ratio η_p/η_π versus particle momentum for positive cylinder tracks. The p/π separation is seen clearly in this figure.

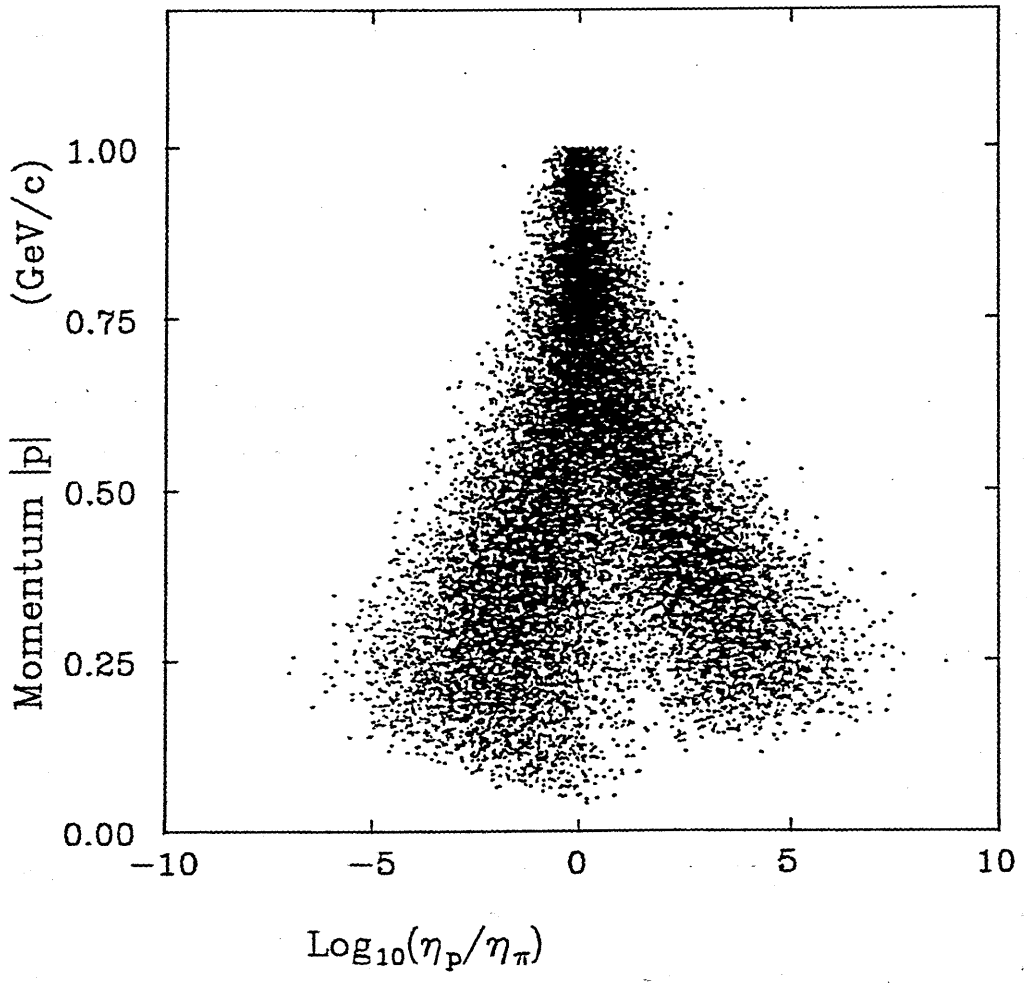

Fig.21 A scatter plot of the logarithm of the likelihood ratio η_p/η_π versus particle momentum for positive cylinder tracks.

3.7 The DATA Acquisition SYSTEM

The read-out system

The signal from the PWC anode are amplified and stored in a shift register memory. The time arrival of each anode signal relative to the event trigger is stored in 6-bits memory. Time-slot in each bit is 25 nsec and the full time window is as large as 800nsec. The total number of the PWC anode wire is approximately 14000 [29,30].

About 2500 channels of PWC cathode signal are first amplified and then passed into a sample and hold module (SHAM -IV)[31]. The hold signal of SHAM module is scanned by 12-bit ADC (BADC) [32]. Each SHAM module consists of 32 individual channels and the BADC multiplexes the 20 SHAM module (640 channels).

The ANNA modules store all of the information from MS chamber. The ANNA module digitize the time information with 20MHz clock. Up to 15 fold timing informations on each wand are stored in this module.

The TDC and ADC information for TOF and Čerenkov counters, the bit information of the counter hodoscope and the signals from beam line devices are read out by conventional CAMAC module. And the scaler information is also automatically read out every 256 events.

These data are collected by DEC PDP-11/04 mini-computer and sent to the SLAC central computer system via IBM system 7. The SLAC central computer were used to spool the data onto magnetic tape and monitors the various aspects of the spectrometer such as efficiency of chambers and coordinate multiplicities.

3.8 The Trigger Logic

The event trigger for this spectrometer is designed to detect the most of Kp induced reactions as much as possible. All of the beam induced events having at least 2 charged tracks are detected in our event trigger. This trigger logic basically consist of two parts; the beam trigger logic and the cluster logic.

The Beam Logic

The beam trigger logic BT is given schematically as:

$$BT = \Theta\Phi \geq 1 \cdot \overline{\Theta\Phi \geq 2} \cdot SE \cdot SY \cdot \overline{RING} \cdot \check{C}_K \cdot \overline{\check{C}_\pi} \tag{3.4}$$

Logic $\check{C}_K \cdot \overline{\check{C}_\pi}$ ensures that a incoming beam particle is a kaon. $(SE \cdot SY \cdot \overline{RING})$ coincidence requires that incoming particle goes into the target. The gate width of the coincidence $(\Theta\Phi \geq 1) \cdot \overline{(\Theta\Phi \geq 2)}$ is set $\sim$ 20 nsec so that no more than one particle enters the target within $\pm$20 nsec. When more than one beam particle enter the target separated more than 40 nsec during a beam spill and makes a reaction in the target, the time information of PWCs and scintillator devices in the spectrometer can discriminate these interactions.

The Cluster logic

The cluster logic determines if two or more charged tracks exist in the region surrounding the target. This is accomplished by counting the number of hits in the two inner cylindrical chambers (CYL) and in the first two plug chambers(PLUG). The detailed description of the cluster logic is listed in the table-4.

Table-4: The cluster logic

Signal	Definition
$PLG_1 \geq 1$	at least 2 planes of PLUG1 have ≥ 1 hit
$PLG_1 \geq 2$	at least 2 planes of PLUG1 have ≥ 2 hit
$PLG_2 \geq 1$	at least 2 planes of PLUG2 have ≥ 1 hit
$PLGS \geq 1$	$PLG_1 \geq 1 + PLG_2 \geq 1$
$CYL \geq 2$	$CYL2 \geq 1 \cdot (CYL1 \geq 2 + CYL2 \geq 2)$
$CYL \geq 3$	$CYL2 \geq 1 \cdot (CYL1 \geq 3 + CYL2 \geq 3)$
$\overline{CYL \geq 3}$	$\overline{CYL1 \geq 3 \cdot CYL2 \geq 3}$
$CYL = 2$	$CYL2 \geq 2 \cdot \overline{CYL \geq 3}$
$CYL = 1 or 2$	$CYL2 \geq 1 \cdot \overline{CYL \geq 3}$

The Event Trigger

The event trigger logic uses these two logics and also the number of hits in the TOF, HA and HB counters. The complete event trigger is formed from the logical OR of four kind of physics triggers, labelled to T0(i) (i = 1 to 4):

$$
\begin{aligned}
T0 &= T0(1) + T0(2) + T0(3) + T0(4) \\
T0(1) &= BT \cdot \overline{LP} \cdot TOF \geq 1 \cdot (PLG_1 \geq 1 \cdot CYL \geq 2 + CYL \geq 3) \\
T0(2) &= BT \cdot \overline{LP} \cdot \overline{(HA \geq 1 \cdot HB \geq 1)} \cdot CYL = 2 \\
T0(3) &= BT \cdot \overline{LP} \cdot TOF \geq 1 \cdot (PLGS \geq 1 \cdot CYL = 1 \textit{ or } 2) \\
T0(4) &= BT \cdot \overline{LP} \cdot TOF \geq 2 \cdot PLG_1 \geq 2
\end{aligned}
\tag{3.5}
$$

The logic $T0(1)$ is for the events with three or more secondaries of which at least two enter the cylinders, $T0(2)$ is for the events with secondaries go predominantly transverse to the target, $T0(3)$ is for the events with at least one goes forward and one or two particles moving transverse to the beam line and $T0(4)$ is for the events that particles are produced to forward direction primarily.

The trigger acceptance for the reaction $K^-p \rightarrow K^-\pi^+\pi^-\pi^\circ p$ is flat and greater than $\sim 97\%$.

The monitor Trigger

At the same time, another 4 minority triggers are used to monitor and calibrate the spectrometer.:

$$
\begin{aligned}
T1 &= BT \cdot \overline{LP} \cdot TOF \geq 1 \cdot HA \geq 2 \cdot HB \geq 2 \\
T2 &= BT \cdot \overline{LP} \cdot TOF \geq 1 \cdot HA \geq 1 \cdot HB \geq 1 \cdot \overline{HA \geq 2 + HB \geq 2} \\
T3 &= BT \\
T4 &= BT \cdot \overline{LP} \cdot TOF \geq 1
\end{aligned}
\tag{3.6}
$$

T1 is designed to be sensitive for the events that the beam particle weakly decays into three charged pions ($K^- \rightarrow \pi^-\pi^+\pi^-$). These events are used to make a relative calibration of the beam momentum and the dipole magnet. T2 trigger accepts K^-p elastic scattering events. T3 trigger yields a random sample of the beam track. These beam sample are used in Monte Calro event generator to simulate the beam profile realistically. The T4 trigger provides a random sample of "interacting" events in the spectrometer. These four minolity triggers are scaled down by the factor of $10 \sim 100$.

3.9 The data sample

The data taking was started February of 1981 and ended on May of 1982. In those over the course of two years, the data were taken in three separate running periods:

1. 2/04/81 – 3/03/81
2. 5/09/81 – 6/29/81
3. 3/27/82 – 5/27/82

Total accumulated triggers are 120 million for a K^- beam, and 23 milion triggers for a K^+ beam. These raw data is stored on $\sim$ 2600 reels of 6250 bpi(byte per inch) magnetic tape.

4. The event reconstruction and calibration

The raw data consist of address of hit wires, pulse height of cathode strip, time information of MS wand and ADC and/or TDC value of counters, etc. The tasks of the event reconstruction program are finding tracks from these raw data, determining the particle momentum by track fitting and the recognition of the event paterns. In this chapter, I describe the basic algorithm used to the event reconstruction in this experiment. Conceptually, the **LASS** spectrometer consists of three elements, Beam line, Solenoid and Dipole spectrometer. The track finding in each element is performed independently, at first, and joined each other later. It is important to emphasize that the success of the algorithm depends crucially on the quality of the raw coordinate information. For this purpose, the basic properties of each device were monitored through the experiment and many calibration and alignment constants were created over the course of the experiment to remove the run-by-run variation.

4.1 Track Parametrization

Tracks to be reconstructed from the raw data include (i) beam tracks, (ii) solenoid tracks, (iii) dipole tracks consist of twixt segments and downstream segments.

The beam tracks and the dipole track segments are fitted by straight lines parametrized by the form:

$$\begin{aligned} X &= X_0 + \left(\frac{dX}{dZ}\right) \cdot (Z - Z_{ref}) \\ Y &= Y_0 + \left(\frac{dY}{dZ}\right) \cdot (Z - Z_{ref}) \end{aligned} \tag{4.1}$$

where $X_0, Y_0, dX/dZ$ and dY/dZ are parameters to be determined and Z_{ref} is a given reference point fixed during the fit.

The solenoid tracks make helical trajectories along the Z-axis. These tracks are fitted by helices. The parametrization we use is :

$$\begin{aligned} X &= X_0 + R \cdot cos(\phi) \\ Y &= Y_0 + R \cdot sin(\phi) \\ \phi &= \phi_{ref} + \frac{d\phi}{dZ} \cdot (Z - Z_{ref}) \end{aligned} \tag{4.2}$$

where $X_0\, Y_0\, R, \phi_{ref}$ and $d\phi/dZ$ are parameters to be determined and Z_{ref} is again a

given reference point fixed during the fit. With this parametrization, momentum and charge of a forward going particle are given by

$$\begin{aligned} P_T &= \alpha \cdot B \cdot R \\ P_L &= \alpha \cdot B / |\frac{d\phi}{dZ}| \\ Q &= -sign(\frac{d\phi}{dZ}) \end{aligned} \tag{4.3}$$

with $\alpha = 2.997925 \times 10^{-4}$ $(GeV/KG \cdot \mathrm{cm})$ and B=22.323 (KG).

4.2 Beam track reconstruction

The position and direction of incoming beam particles are measured by the beam chamber package (beam PWCs). This beam package is physically divided into upstream of anode planes having x, y, p and e coordinates and a downstream package giving y, x, y', x' , and p . The pattern recognition algorithm begins by forming two-way, three-way and four-way match points in each package. These match points are made only for the points that has consistent timing known from the time-slot information. The Beam track candidate are formed from a pair of these match points. Only pair of the match points are selected whose timing is consistent with that a particle passes through these chambers. In these candidates, a good in-time beam tracks are selected by requiring that the beam track is corroborating with $\Theta\Phi$ hodoscope and it also passes through SY counter. As a result, a single track is found in $\sim$ 50% of the events, while double and triple beam tracks occur at the rate of $\sim$ 35% and $\sim$ 15% , respectively. The primary beam track is then selected as one from the proximity to the events trigger timing and maximum hodoscope corroboration.

There are no confusion to select the corresponding beam track. However, the other beam tracks also produce the hit points in the PWCs located along the beam region in the spectrometer. To reduce the confusion created by these secondary beams, the PWC coordinates corroborating to these beams are poisoned out, and are not used to define the match points in the Solenoid track finding.

4.3 Solenoid track reconstruction

The solenoid track reconstruction consists of

1. The coordinate making for each cathode and anode planes.
2. The match points making in each chamber.
3. Track finding and fitting by a helix.

The coordinate making

The timing signals from the PWC anodes are recorded wire by wire in the time slot bits. The first task is to select intime bits and to cluster the hits on contiguous wires. The center position is used if contiguous wires are hit. The coordinates of anode are then obtained by multiplying cluster address and wire spacing.

The coordinate perpendicular to the cathode strip is obtained from the pulse height ratio between the peak pulse height at the center strip and the pulse height of it side strips. Since usually a track induces the significant signal in three strips, we have two pulse height ratios with left and right strips (R_l, R_r). These pulse height ratios are uniquely related to the position of an avalanche caused by a particle passing through. To obtain this avalanche position, expected induced pulse shape is calculated with the assumption of point charge located in the middle of two infinite grounded conducting planes. With this assumption, the induced charge density at a point (x, y) due to an image charge Q at (x_0 ,0) can be calculated. Here x is the direction along the anode wire and y is perpendicular to anode. By integrating over y for a strip with edges at x_1 and x_2 , the induced cathode charge is given by:

$$C(x_0) = \frac{Q}{\pi}\sum_{n=0}^{\infty}(-1)^n\left(\tan^{-1}\left(\frac{x_2 - x_0}{(2n+1)g}\right) - \tan^{-1}\left(\frac{x_1 - x_0}{(2n+1)g}\right)\right) \qquad (4.4)$$

where g is the effective gap length between anode and cathode planes. From this distribution, we obtain the relation between the pulse height ratio and the avalanche position (x_0). In practice, however, one adjustment of a parameter in this equation is necessary to reproduce the observed distribution of the pulse height ratio. This adjustment is done by tuning the effective gap length (g) so taht the observed pulse height ratio is reproduced (fig.22).

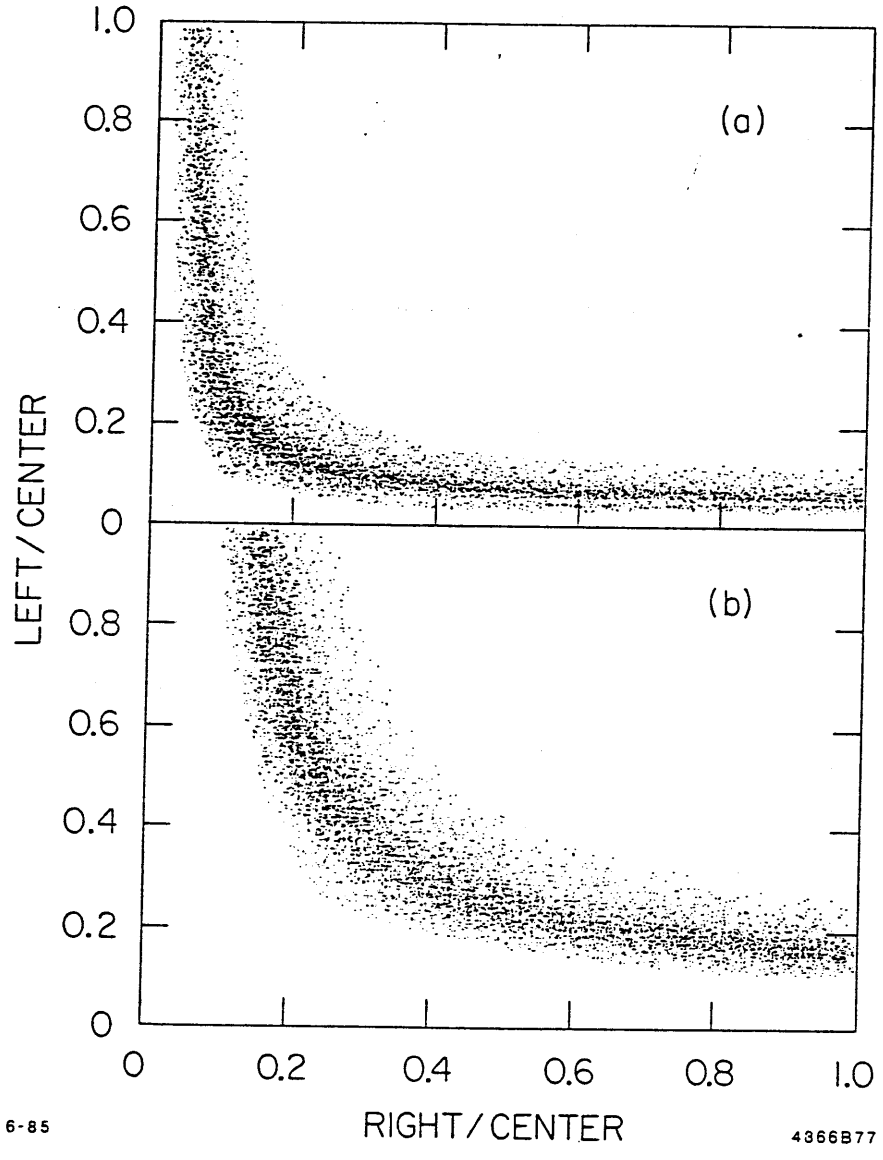

Fig.22 The scatter plot of left and right pulse height ratio for (a) the down stream foil of GAP2 and (b) the inner foil of cylinder 2.

The merit of this method is that coordinates are obtained directory without fitting the pulse height distribution and can be calculated very fast. And this method is free from the systematics observed in other methods. It is known that the position given by the center of gravity or fitting by Gaussian or Lorentzian is shifted systematically depending on an avalanche position on a cathode strip.

In addition to this basic algorithm, various corrections were necessary to achieve the good resolution which is presented in the previous chapter. One was mechanical corrections for foil deformation. Since cathode foils were stretched over the chamber frame, the cathode foil were distorted. This distortion was surveyed by microscope for each strip before installing the chamber and correction was done based on this data. The correction of the amplifier gain and pedestal were performed using the calibration data provided by test pulse.

The wire by wire spacing of the anode plane in the Gap chambers was also surveyed directly before installation. Because of these fine tuning and a capability of defining 3 dimensional coordinate point thanks to the anode and cathode read out, the coordinates of Gap chambers are most reliable. Gap chambers are, then, used as the absolute reference in the solenoid spectrometer.

Track reconstruction in the Solenoid

The helix track-finding algorithm is based on the use of match points derived from the individual PWC devices in the solenoid. As the first step, a helix candidate is chosen from any of three match points in separated devices. This helix candidate is extrapolated to the other devices and searched how many corroborating coordinates are found within a suitable window size(4 σ). If a candidate has a small number of corroborating points compared to the expected number of corroborating points, that candidate is discarded immediately. A χ^2 fit to a helix is performed to the remaining candidates. If the resulting χ^2 is good (if the fitting probability is greater than $> 10^{-4}$), the track is accepted.

To speed up the track finding algorithm, a special procedure known as 'poisoning' is invoked. That is, once a track with good quality is found, the coordinates associated to this high quality track are poisoned, i.e. they are flagged as being already used and are removed from match points yet to be used. This procedure drastically reduces the

number of helix candidates. The resultant track finding efficiency for a non decaying track is more than 99 %. This results are checked by eye-scan of several hundred events and also from Monte Calro study.

4.4 Dipole track reconstruction

Reconstructing particle trajectory in the dipole spectrometer involves three distinct steps.

1. Coordinate making in MS chamber.
2. Finding lines in the twixt region and the downstream region of the dipole magnet.
3. Crossing each downstream line and the twixt line through the dipole magnet.

MS coordinate making

The coordinate of the MS chambers are determined from the time between the fiducial signal and the each spark signal pulse propagate in the magnet strictive wand line. The important correction for these coordinate is for the non-linearity caused by the variation of propagation speed along a magnetostrictive wand line. This correction factor was determined using many tracks of real data. Since the stability of the magnetostrictive wand line was not good, $\sim$ 50 correction tables were recreated over the course of the experiments.

The twixt and dipole track finding

The first step of the track finding in these region is to determine the candidate of the track segments using any two MS (or PLUG) chambers in down or twxit regions. The goodness of this track candinate is judged by comparing the number of corroborating points on another chambers and the expected numbers. If the level of corroboration is acceptable, a line fit is performed and if the confidence level of the fit is $< 10^{-4}$, those candidates are rejected. A final check is made to see whether the track candidate is associated by in-time devices of scintillator hodoscopes or proportional chambers. If no association is found in those devices those track candidates are discarded.

In the next step, the downstream and twixt tracks are crossed through the dipole magnet. The momentum of the track is determined by swimming the downstream track through the dipole magnetic field into the twixt region. The initial estimation of the

momentum is made from the total bend of the track in the x-z plane. The discrepancy between the angle of the swum track and the twixt track provides a correction to the initial momentum estimate. This procedure is iterated until the angles of the swum track and twixt track agree. The error in the momentum is determined from the uncertainty of the downstream and twixt tracks, taking the multiple scattering effect into account.

The txist MS chambers were more inefficient than the downstream chamber. If a twixt partner of a downstrem track is not found, the twixt track finding is repeated by using the angle of the downstrem track in the non-bending plane(the y-z plane). The resulting twixt line-finding efficiency is 95 %.

Joining and swimming of the tracks

The final step of the tracking is the joinig of the dipole track to the corresponding solenoid helix track. The dipole track is swum from the twixt region back into the solenoid upto the Gap 3. This swimming is performed by the Runge- Kutta method using the measured field map. At that point, the joining is checked in position and direction. If the partner is found, those solenoind track is refitted with the constraint of the momentum detemined by the dipole.

A precise hit location in TOF and $\check{C}_1$ counters is necessary to obtain the propagation time in the TOF counter and to define the fiducial volume in the $\check{C}_1$ cells. The unjoined solenoid tracks are also swum to TOF counter by the same Runge-Kutta method.

4.5 Topology Recognition

The final task of the event reconstruction program is to associate the beam and solenoid tracks to the production (primary) and the decay (secondary) verteces.

The primary vertex is reconstructed from the tracks of final state and beam track. The location is determined by a least square fit, which minimize sum of the square of distance d_i between the i'th track and a common primary vertex position :

$$PVQ = \sum_i d_i^2/n,$$

where n is the total number of vertex associated tracks. If the quality of the fit to this common vertex is poor, the track with the largest contribution to PVQ is removed

and the minimization is repeated. This procedure is iterated until an acceptable fit is achieved.

Similar algorithm is used to seach the candidate of $K^0, \Lambda, \overline{\Lambda}$ and γ convertion around the target. These particles make the geometrically clear signature of V° vertex. This V° vertex is looked for any pair of opposite signed tracks that pass within 1 cm at the closest point. The vertex point of V° is determined by a least square fit by minimizing the distance between a common secondary vertex and the 2 decayed tracks. The minimum decay length required is 1cm - 2cm depending on the V° production angles. Then the candidates for K^0, Λ and γ are loosely selected by assuming the appropriate tracks mass to decayed tracks.

The resultant topologies of the events are classified into following eight classes:

1. Top(1) : n-prong (All charge helices are associated with the primary vertex.)
2. Top(2-4): one V° + n-prong, where V° is consistent with $K^\circ, \Lambda, \overline{\Lambda}$ or γ
3. Top(5) : one V^- + n-prong
4. Top(6) : two V° + n-prong
5. Top(7) : one V° and V^- + n-prong
6. Top(8) : Three V° + n-prong

Usually it is not possible to unambigously asciribe an event to one particular topological configuration. Some times the tracks can be arranged into several different vertex configurations. In this case, the multiple choices of the topologies are permitted.

4.6 The production of Data Summary Tape

The event reconstruction algorithm required 0.55 sec/event on an IBM 3081K computer. Required CPU time to process the entire data sample is 2.4 CPU years. (IBM 3081K equivalent). To meet this need, the event reconstruction was shared by three computers. FACOM M200 at Nagoya University high energy Laboratory, FACOM M382 at Nagoya University Computer Center and 9 168/E processors at SLAC. About 60 % of data were processed by the first two computers and the remaining were processed by 168/E. Using these computers, the event reconstruction could be finished in a year.

The results of the events reconstruction and the track associated coordinate information are stored in DST (Data summary Tapes). The data sample contained in the DST is $11 \cdot 10^7$ events in K^- beam experiments. These huge number of events are stored in about 1000 reels of 6250BPI (byte/inch) DST tapes.

5. The event selection of the K $\pi^+\pi^-\pi^\circ$ p sample

This chapter describes the event selection to filter the reaction:

$$K^-p \rightarrow K^-\pi^+\pi^-\pi^\circ p \tag{5.1}$$

off E135 DST's. The $K^-\eta p$ final state is obtained from this reaction by taking η resonance region in the $\pi^+\pi^-\pi^\circ$ system. In the final state of this reaction (5.1), there are 4 charged particles and one neutral π°. The π° in this final state is unseen particle in this experiment, since no γ counter is equipped in the **LASS** spectrometer. But, this reaction can be reconstructed in this spectrometer since it covers nearly 4π acceptance and its reconstruction efficiency of charged particles is execellent.

Starting from the DST's, the filtering of the reaction (5.1) is performed by following four steps.

1. The topological event selection and loose kinematical cuts.
2. The Kinematic fits
3. The Particle identification
4. The final event selection

In the first step, the candidates of the $K^-\pi^+\pi^-\pi^\circ p$ events are selected from four prong events by imposing the loose missing mass cut. In the next step, the surviving events are refitted with a full kinematical constraints to distinguish reaction (5.1) from the predominant background process : $K^-p \rightarrow K^-\pi^+\pi^-p$. And one-kinematical constraint fit called 1-C fit is performed assuming the true reaction (5.1) . Four kinds of 1-C fits are carried out with different mass hypothesises to cover all possible combinations of charged particle masses. Then the ambiguities of the mass assignment remained in the 1-C kinematical fit are resolved by using the information of two Čerenkov counters and TOF counter hodoscope in the third step. The final event selection is carried out to reduce the remaining background in the sample.

The kinematical fits done in the second step serve a powerfull tool for data selection and the improvement of resolution. This fit (1-C) is also useful to reduce the possible number of combinations for charged particle masses. The effectiveness of these fitting procedure are examined by the real event observing narrow signals of η and ω resonance in the $\pi^+\pi^-\pi^\circ$ system. The detail of the event selection is discussed in following sections.

5.1 The topological event selection and loose kinematical cuts

A first step in the $K^-\pi^+\pi^-\pi^\circ p$ data selection is focussed on deducing huge data sample to a more manageable size. Those events consist of four prong associated to the interaction vertex with net charge zero are selected as candidates for the reaction (5.1), and following rather loose kinematical requirements are imposed: (a) for at least one mass assignment combination, the missing mass squared (MM^2) recoiling against $K^-\pi^+\pi^-p$ must satisfy $|MM^2| < -0.3(\mathrm{GeV/c^2})^2$; (b) the four momentum transfer $|t'_{p-p}| = |t - t_{min}|$ is smaller than $2.0(\mathrm{GeV/c})^2$ for at least one of the accepted mass permutations; and (c) with the assumption that the missing momentum vector corresponds to π°, the effective mass of the three pion system $M(\pi^+\pi^-\pi^\circ)$ must satisfy $M(\pi^+\pi^-\pi^\circ) \leq 1.1$ GeV/c for at least one of the surviving mass combinations.

3177K events survived these criteria. A typical missing mass square distribution for these sample is shown in fig.23, where 4 enetries per event are plotted assuming all hypothetical combinations of $K^-\pi^+\pi^-p$. A peak seen around $MM^2(K^-\pi^+\pi^-p) \sim 0$ comes from the reaction (5.1) and the predominant background process: $K^-p \rightarrow K^-\pi^+\pi^-p$.

The effective $\pi^+\pi^-\pi^\circ$ mass distribution for these 4 prong events of all sample are shown in fig. 24. Again all possible mass combinations of $K^-\pi^+\pi^-p$ are plotted per event if missing mass square falls in the region between -0.15 $(\mathrm{GeV/c^2})^2$ and 0.1 $(\mathrm{GeV/c^2})^2$† A clear ω signal is already observed above a large continuous background, and a little bump of η signal is seen at $M(\pi^+\pi^-\pi^\circ) \sim 0.55\mathrm{GeV/c^2}$.

Futher event selections are, then, carried out focussing on the reduction of these substantial background. The refit of the event with kinematical constraints and the information of particle indentification devices are very effective to reduce these background.

† More tight missing mass square cut than the criteria (a) is applied to make possible of the direct comparion between this distribution and the later sample.

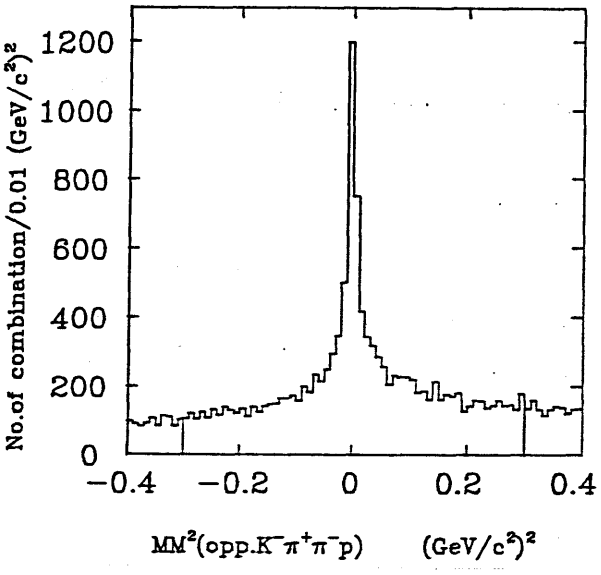

Fig.23 A typical missing mass square $MM^2(K^-\pi^+\pi^-p)$ distribution for 4 prong sample. 4 enetries per event are plotted assuming all hypothetical combination of $K^-\pi^+\pi^-p$.

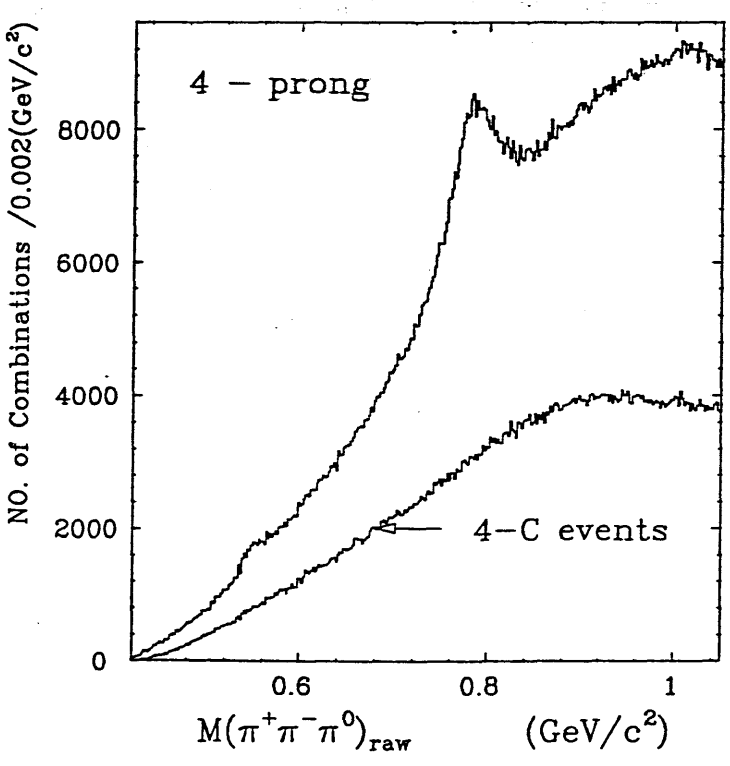

Fig.24 The $\pi^+\pi^-\pi^\circ$ effective mass distribution for all 4 prong events. All possible mass combinations are plotted. The inner histogram is the same distribution for the events removed by 4-C fit as the candidate of the reaction: $K^-p \to K^-\pi^+\pi^-p$

5.2 The Kinematic fit

The refit of loosely selected $K^-\pi^+\pi^-\pi^\circ p$ event are performed by a multi-vertex least-squares fitting program called MVFIT. This program refits the track associated measured coordinates with the constraints of the point primary vertex or/and of the reasonable kinematical requirements. The method of *Lagrange* multipliers is used in this constraint fit. In this method a χ^2 function to be mimimuzed is defined by the form:

$$L = \sum_i \left(\frac{x_i - x_{pred}}{\sigma_i} \right)^2 + 2 \sum_j \lambda_j F_j \tag{5.2}$$

where x_i are measured coordinates; x_{pred} are the predicted coordinates for the current set of tracks and vertex parameters; σ_i are the estimated error of x_i including the effect of multiple scattering; λ_j are addtional free parameters of the *Lagrage* multipliers and F_j are the equations which define the constraints such as point vertex , energy or momentum conservation.

The fit only with the constraint with the point vertex is called "Geometry" fit. Together with Geometry fit, we also fit each event with two different kinematical hypotheses. One is so called 4-C fit and the other is 1-C fit. In the 4-C fit, the event is fitted with the hypothesis $K^-p \rightarrow K^-\pi^+\pi^-p$ imposing the constraint that the energy and 3 momenta are conserved between initial and final state. On the other hand, in the 1-C fit, we assume the true reaction $K^-p \rightarrow K^-\pi^+\pi^-\pi^\circ p$. With the assumption that missing momentum is carried by a π°, the total energy conservation gives one kinematical constraint.

In general, there are four possibilities of mass assignments for the charged particles in these reactions. Two of these possibilities come from the permutation of K^- and π^- for two negative charged tracks and another two combinations come from the permutation of π^+ and p for the two positive tracks. Explicitly , these four combinations are written as follows:

$$\begin{aligned}
&\text{i)}\ X_f^- X_s^- X_f^+ X_s^+ &&= K^-\pi^-\pi^+ p \\
&\text{ii)}\ X_f^- X_s^- X_f^+ X_s^+ &&= \pi^- K^-\pi^+ p \\
&\text{iii)}\ X_f^- X_s^- X_f^+ X_s^+ &&= K^-\pi^- p\ \pi^+ \\
&\text{iv)}\ X_f^- X_s^- X_f^+ X_s^+ &&= \pi^- K^- p\ \pi^+
\end{aligned} \tag{5.3}$$

where the superscript +/- of X denotes the charge of a particle and the subscript f/s specifies the faster or slower particle in the same charged tracks according to the longitudinal momentum P_z.

Four kind of fits assuming these combinations of mass hypothesis are performed in both 4-C and 1-C fits. The CPU time required to fit each event was approximately 1 sec on FACOM M200 equivalent, the resultant total CPU time to process 3177K events was 883 hours.

The event selection after MVFIT

The convergence of geometry fit is required to filter good candidates of the reaction (5.1). The predominant background process $K^-p \rightarrow K^-\pi^+\pi^-p$ is removed if events satisfy the 4-C kinematical hypothesis with the confidence level of $\geq 1.0^{-10}$ for at least one possible particle assignment. Then the events are accepted if they satisfy the 1-C kinematical hypothesis $K^-\pi^+\pi^-\pi^\circ p$ with the confidence level of $\geq 1.0^{-10}$.

The events with poorly measured tracks are failed in the geometry fit but thaose are negligible (0.6 %). The confidence level distribution of 4-C fit and cut value is is shown in fig. 25. To show the reliability of 4-C cut, $M(\pi^+\pi^-\pi^\circ)$ distribution of the removed events by this cut are shown in the inner histogram of fig.24 . Approximately 41 % events are removed by this 4-C cut but no evidence of the loss of η or ω signal is observed in these rejected events. The cut position of 1-C fit is shown in fig. 26, and the same $\pi^+\pi^-\pi^\circ$ effective mass distribution eliminated by this 1-C confidence level cut is seen in fig. 27-b . Additional 25 % of events are removed by this 1-C cut but also no evidence of η or ω is observed in these discarded event smaple.

As are shown, these kinematical fits are very effective to remove the background without serious loss of true events.

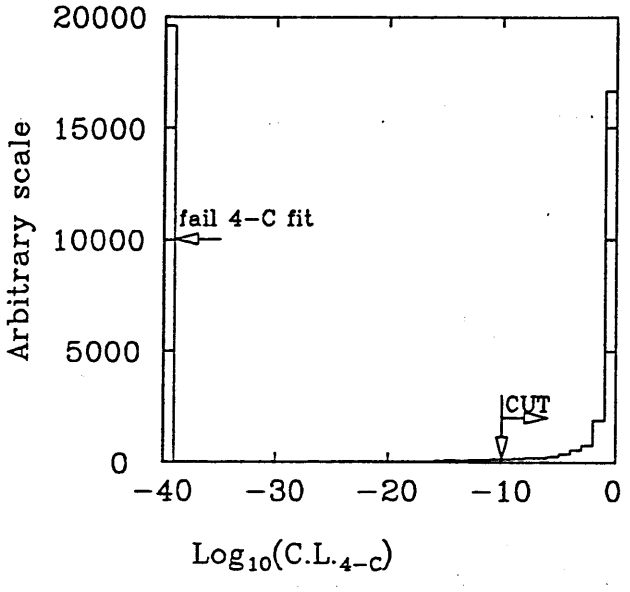

Fig. 25 Confidence level distribution of 4-C fit with the hypothesis $K^-p \to K^-\pi^+\pi^-p$

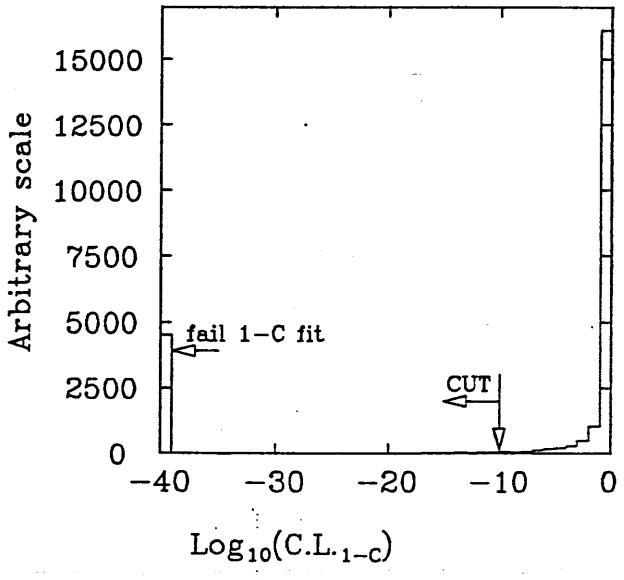

Fig. 26 Confidence level distribution of 1-C fit with the hypothesis $K^-p \to K^-\pi^+\pi^-\pi^0 p$

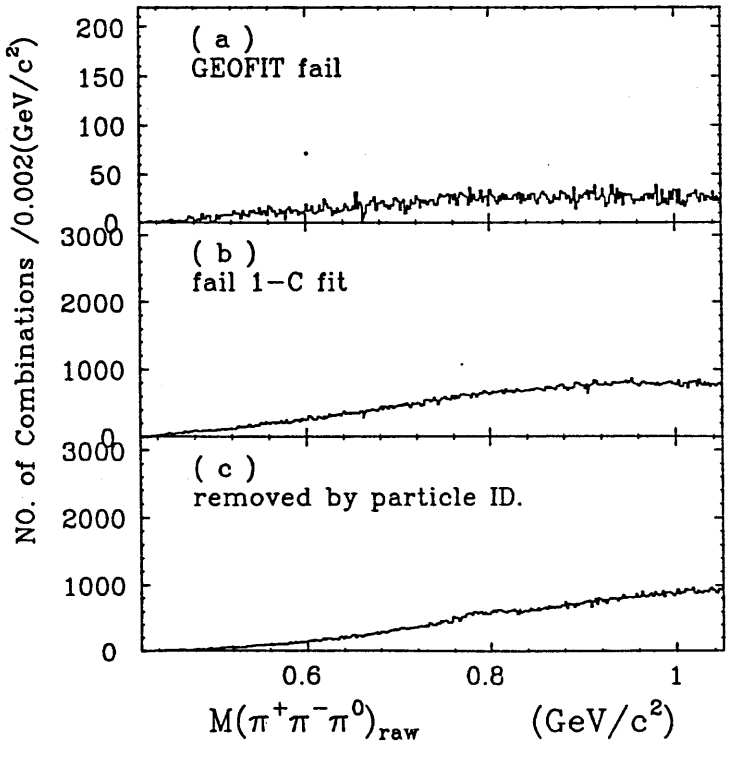

Fig. 27 The $\pi^+\pi^-\pi^0$ effective mass distribution removed by (a) geometry cut. (b) 1-C confidence level cut (c) anti-particle identification. All possible combinations of $K^-\pi^+\pi^-p$ are plotted per event.

5.3 The particle identification

The events are accepted if they satisfy the 1-C hypothesis for at least one possible particle assignment. Then the ambiguities of the mass assignment are remained in these sample. The information of two Čerenkov counters and TOF system is useful to resolve these ambiguities. This section summarize the condition of the particle identification by these devices.

The $\check{C}_1$ and $\check{C}_2$ Čerenkov counters are used to separate π and K above 3.0 GeV/c. To reduce the probability of mis-identification in these devices, good $\check{C}_1$ cell region which gives the local efficiency $\geq 95\%$ for pion is used to identify kaon.

The TOF counter system is used to identify both positive and negative particles. Using the measured time t by TOF system and the particle momentum p, the mass square of a particle is given by the equation :

$$m^2(\beta) = p^2 \left\{ \left(\frac{tc}{L} \right)^2 - 1 \right\} \tag{5.4}$$

where L denotes the path length of a particle, and c is the velocity of light.

In the sample passed the 1-C loose cut, the m^2 distribution is plotted against the momentum in fig. 28-a and fig.28-b for positive and negative charged particles, respectively. For positive charged particles, clean π^+ and p band are seen and K^+ signal are negligiblly small. The information of TOF counters are used to separate π^+ and p below 2.3 GeV/c if the mass derived from (5.4) is consistent with π or p mass within 3 σ. For negative charged tracks, the signal is dominated by π^-. The band of K^- is not clear since the number of slow K^- particles is relatively small in this momentum range. To pick up the well identified π^- , 3 σ separation of π and K is required below 1.3 GeV/c .

Using these information of particle identification, good combinations of mass assignment are selected from the solutions succeeded by 1-C fit. For example, in a case that 1-C fit succeeds in the mass assignment for X_f^+ be π^+ and X_s^+ be p but still has ambiguities i) and ii) shown in Eq.(5.3) , and if a faster negative chaged particle X_f^- is identified by Čerenkov counter as π^-, then we can define the right mass assignment ii) for this event. In this way all consistent assignments are picked up from the solutions of

1-C fit. With this rather loose requirement of the particle identification, the ambiguity of the mass determination is reduced drastically. In fact, as is discussed in the latter section, the possible mass assignments in the final sample can be determined uniquely for about 90% of total events. Before discussing these points more quantatively, I summarize the futher cuts applied to the sample.

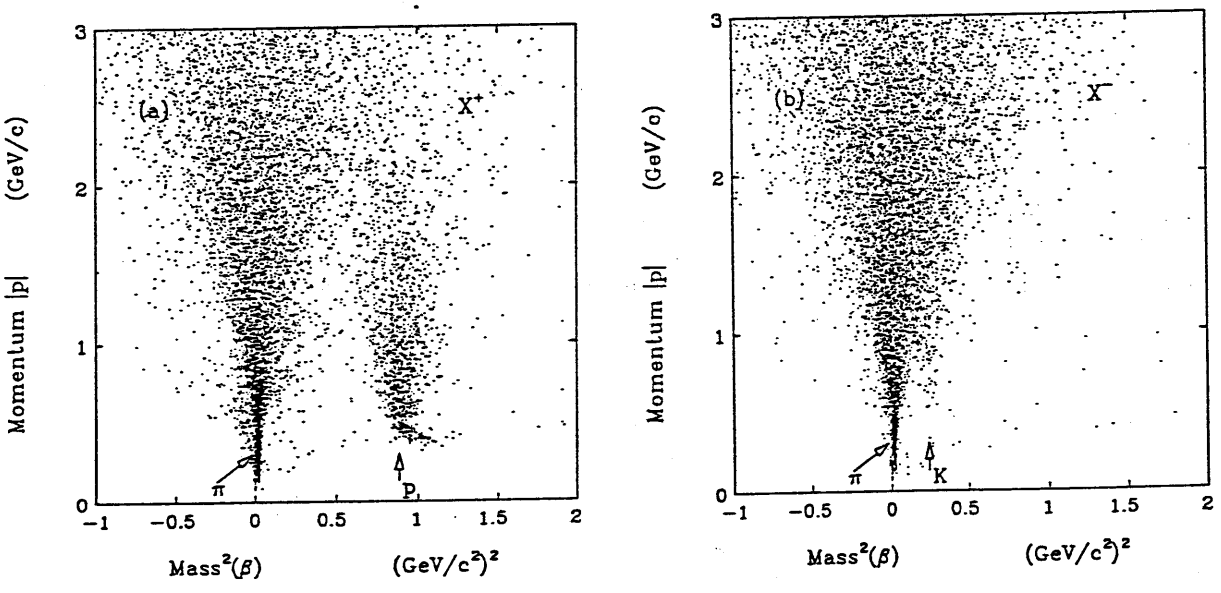

Fig.28 The scatter plot of particle momentum versus m^2. m^2 is derived from measured time by TOF counters. (a) and (b) show the distribution for plus, minus charged particles, respectively.

5.4 The final event selection

In the final step of the event selection, I have searched possible good criteria to reduce the remaining background without serious loss of the true events. As a result, I have found following cuts are appropriate for this purpose.

1. The anti-particle identification:

2. The V° rejection:

3. The target region cut:

4. The dE/dx cut:

5. The tight missing mass and 1-C confidence level cut:

1. The anti- particle identification

Since the constraint of 1-C fit itself is rather loose, it is possible that another non $K^-p \to K^-\pi^+\pi^-\pi^\circ p$ events are also fitted accidentally by 1-C fit. To remove some of these background, following two classes of events are rejected using the information of the particle identification.

1. 8 % events are positively identified such non $K^-\pi^+\pi^-p$ combinations as $\pi^-\pi^-X^+X^+$, $K^-K^-X^+X^+$, $X^-X^-\pi^+\pi^+$ and $X^-X^-K^+X^+$, where $X^\pm$ stand for the non identified particles by particle identification devices.

2. There are another class of events which the results of particle identification are consistent with the $K^-\pi^+\pi^-p$ combinations but they are inconsistent with all succeeded solutions of 1-C fit. For example, a faster negative charged particle X_f^- is identified as K^- by Čerenkov counter but only mass assignments of π^- for this particle are succeeded by 1-C fit. 17 % of events falls to this class and are eliminated from the sample.

In these two classes of event, only small evidence of η or ω signal are observed as shown in fig.27-c. These loss are consistent with the mis-identification probabilities of particle identification devices.

2. The V° rejection

Other useful cut to reduce the background is the rejection of the event including the γ conversion around the target. Although non ambiguous V° events have been removed when we have selected 4 prong events, the events which have a V° solutions as alternative topology assignment still remain in these sample. For these candidates, the scatter plot of the decay helicity angle at the rest frame of the V° versus V° mass is shown in fig.29. In this distribution, pion mass is assumed for the decayed daughter particles. Clear bands of γ seen in the left edge of this figure, while K° band

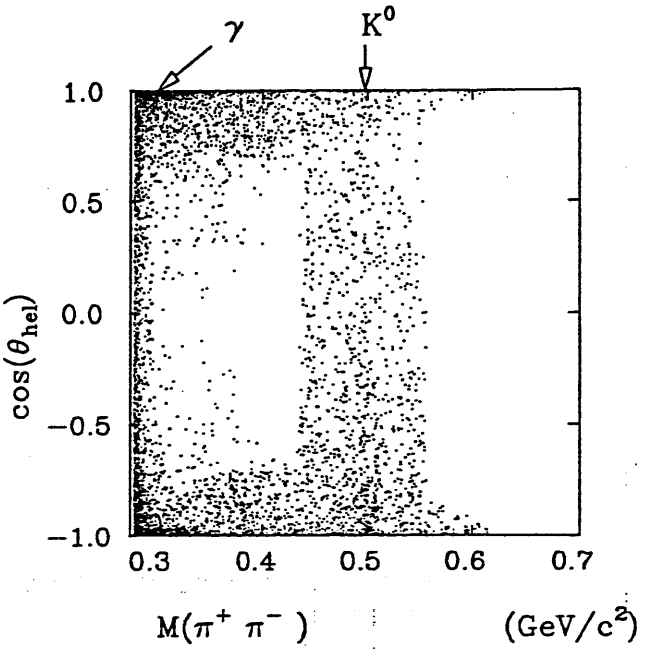

Fig. 29 Scatter plot of the decay helicity angle versus to V^0 mass for the V^0 candidates. Pion mass is assumed for decayed particles.

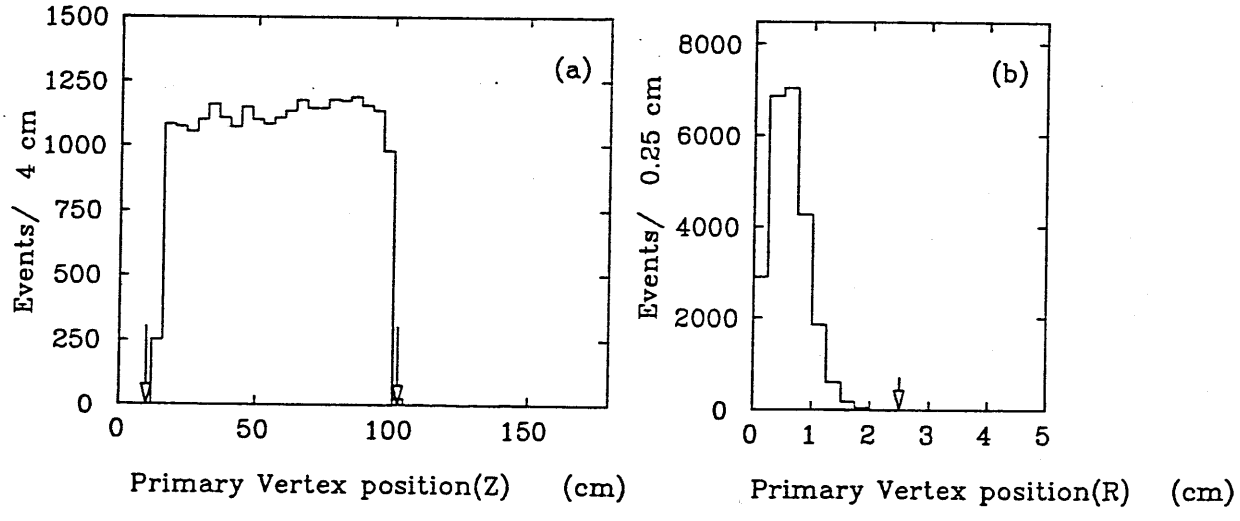

Fig. 30 The distribution of beam interaction position. (a): Z position and (b): radial position. Arrows indicate cut position

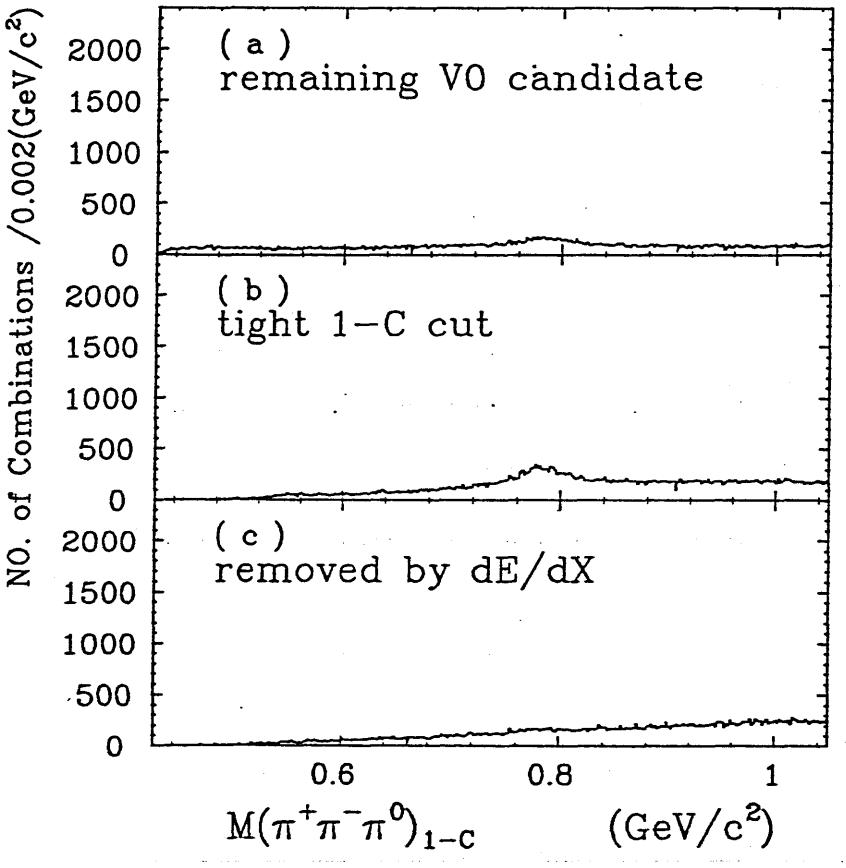

Fig. 31 The $\pi^+\pi^-\pi^\circ$ effective mass distribution removed by (a) the V0 cut. (b) the 1-C tight cut. (c) the dE/dx cut. All possible combinations of $K^-\pi^+\pi^-p$ are plotted per event.

is not clear. These γ candidates are rejected, if following two criteria are satisfied. (1) the mass of V° is less than 5.5MeV/c^2 with the assumption that daughter particles are electron . (2) The decay length of V° (i.e. the distance between primary and V° vertex) is greater than 2.0 cm. Additional 6 % of events are removed by this cut. The $M(\pi^+\pi^-\pi^\circ)$ spectrum for rejected events are shown in fig. 31-a.

3. The target region cut

The location of beam interaction point (fig.30) is required to be inside the target :

$$\begin{aligned} -10.1 \text{ cm} < PVZ &\leq 102.1 \text{ cm} \\ PVR &\leq 2.5 \text{ cm} \end{aligned} \tag{5.5}$$

where PVZ is a primary vertex z position and PVR is a radial distance of the vertex from the target center. The effect of this cut is small(0.3 %).

4. The dE/dx cut

One independent check on the mass assignment can be made using dE/dx information on the cylindrical chamber. The likelyhood function describing the ratio of pion and proton probability derived from the pulse height information of the crylindrical chamber is plotted against the particle momentum in fig. 32. The particles of K^-, π^+ π^- and p specified in each figure are the assignment determined using Čerenkov , TOF counters and 1-C kinematic fit. As can be seen in these figures, the dE/dx information for K^- and π^- are consistent with the particle assignment, while for π^+ or p, we can observe the small portion of the events that dE/dx tells wrong assignment. These excessed events specified by the solid line of fig.32-c and fig.32-d, are removed since three pion mass $M(\pi^+\pi^-\pi^\circ)$ spectrum for these rejected events shows no evidence of the η or ω signal by all possible combinations of mass assignment (fig.31 -c). Additional 10 % of events are removed by this cut.

5. The tight missing mass and 1-C confidence level cut.

Finally the criteria on the missing mass and 1-C confidence are tightened to

$$\begin{aligned} &-0.15(\text{GeV/c}^2)^2 < MM^2(\text{opp. } \text{K}^-\pi^+\pi^-\text{p}) \leq 0.1(\text{GeV/c}^2)^2 \\ &C.L._{1-C} \geq 0.01 \quad . \end{aligned} \tag{5.6}$$

The tight 1-C cut is required in order to reduce the ambiguity of the mass assignment. The lost events by this tight 1- C cut is shown in fig.31- b.

The missing mass squared $MM^2(K^-\pi^+\pi^-p)$ distribution calculated from the unfitted quantities is given in fig.33. The vertical lines in this figure indicate the cut position.

583092 $K^-\pi^+\pi^-\pi^\circ p$ sample are passed all cuts described above. We call this a final $K^-\pi^+\pi^-\pi^\circ p$ sample.

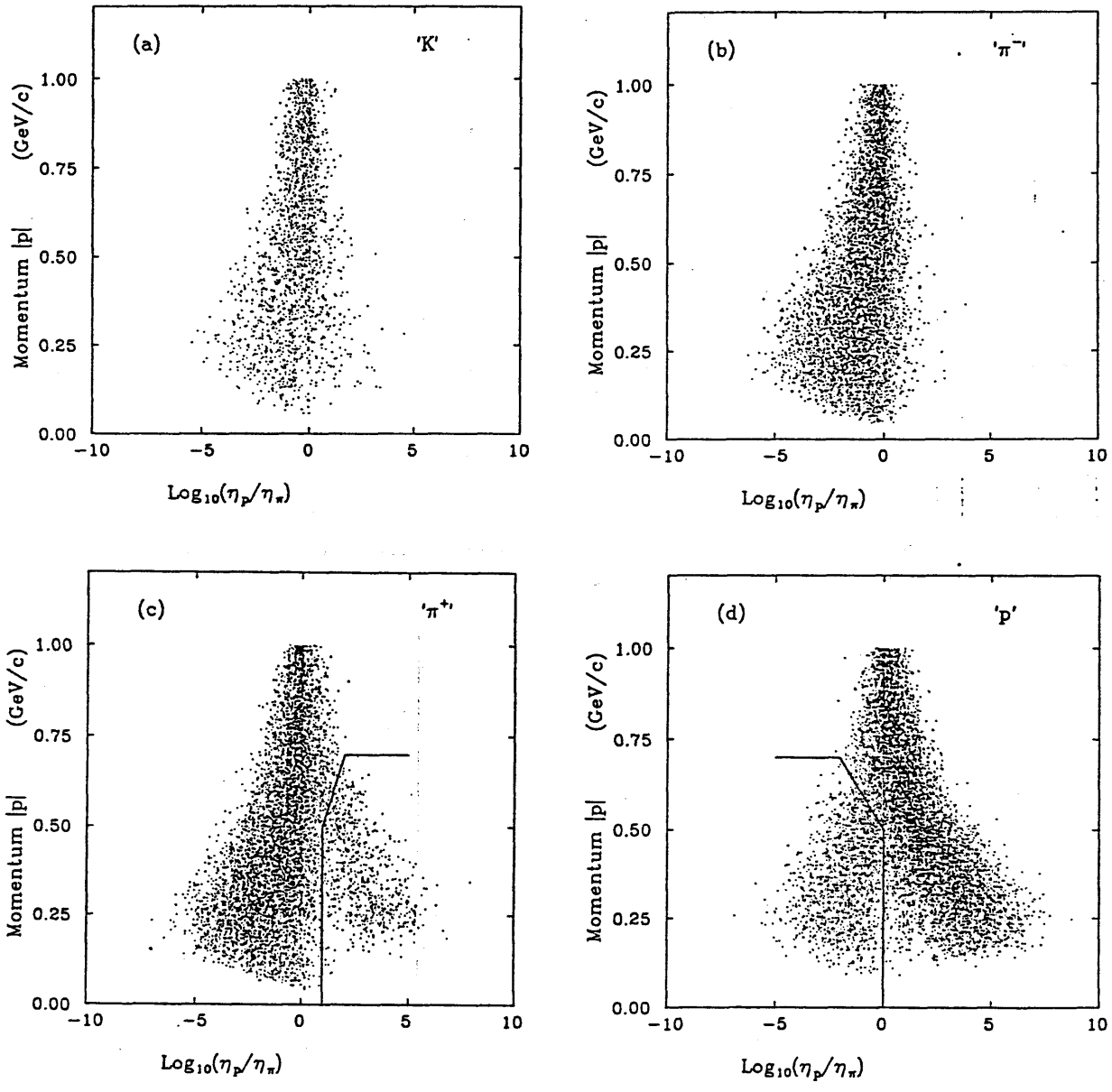

Fig. 32 Particle momentum versus $log(\eta/\eta_\pi)$ for the final sample of $K^-p \rightarrow K^-\pi^+\pi^-\pi^\circ p$ events. The particles (a) K^- , (b) π^- ,(c) π^+ and (d) p specified in each figure are the ones determined using another particle devices and 1-C fit. The lines in (c) and (d) indicate the cut position used to remove inconsistent events.

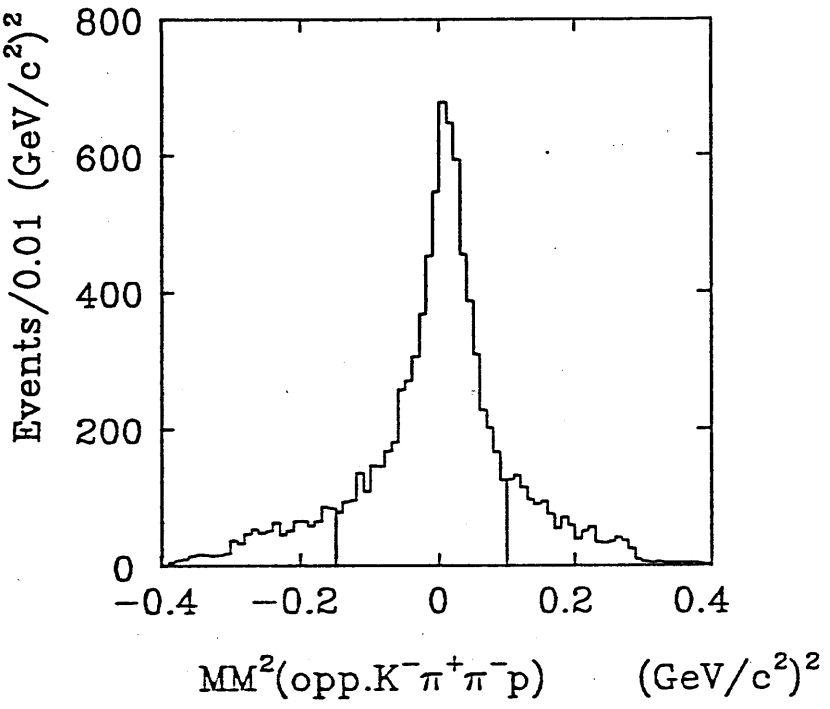

Fig. 33 A typical raw $MM^2(K^-\pi^+\pi^-p)$ distribution calcurated from the unfitted quantities of $K^-p \to K^-\pi^+\pi^-\pi^\circ p$ sample passed all selection criteria. The vertical lines indicate the cut position. The most probable one combination of charged particle masses described in the text is used to calculate the missing mass square.

5.5 The discussion of mass assignment

In this final sample, 1-C kinematical fit gives in an unique assignment of the charge particle masses for 62 % of events, and other 25 % , 12 %, 1.0 % of the events have 2 , 3 or 4 fold ambiguities. It should be noted that the possible number of the assignment for charged particle is limitted relatively well by 1-C kinematical fit. And the remaining ambiguities of 1-C fit mainly exist in an alternative assignment between K^- and π^- of high momentum ($\geq$ 1.0GeV/c) two negative charged particles. On the other hand, π^+/p discrimination is done reasonably well by this 1-C kinematical fit.

The particle identification by Čerenkov and TOF counters are in the complementary situation. The high or moderate momentum particles can be idenfified by these devices. Therefore these informations work effectively to reduce the remaining ambiguities in 1-C fit. To illustrate the overall situation of the particle identification, the event ratio that each particle in a event is identified by these particle identification devices are summarized in Table-5.

Table-5:

	K^-	π^-	π^+	p
Čerenkov	50 %	26 %	17 %	-
TOF	0.5 %	12 %	27 %	6 %
Čerenkov/TOF	50 %	38 %	44 %	6 %
Čerenkov/TOF	72 %			

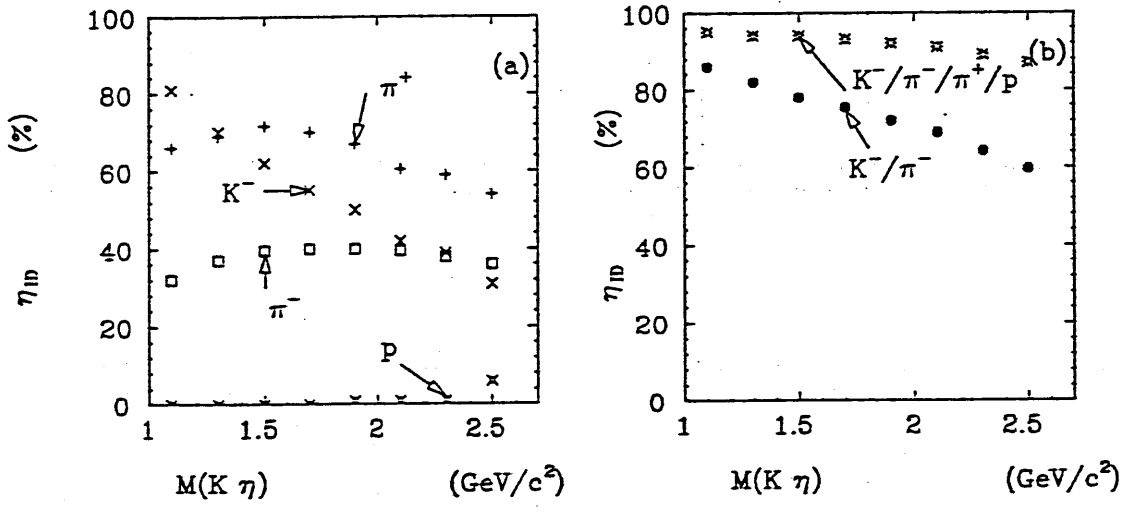

Fig.34 The probability of particle identification by Čerenkov and TOF counters for the rection $K^-p \to K^-\eta p$, ($\eta \to \pi^+\pi^-\pi^\circ$) (a) : The identification probabilities of K^-, π^+, π^- and p . (b): the probabilities that either K^- or π^- is identified and at least one of the particle is identified . In this Monte Calro, the decay angular distribution is thrown uniformly.

As can be seen from this table, each K^-, π^-, π^+ praticle is identified for almost half of the events. And for 72 % of full data sample, either K^- or π^- is identified by these devices. To see the situation in the η mass region , the same probabilities of particle identification studied by the $K^-p \to K^-\eta p$ Monte Calro event are shown in fig. 34. The Monte Calro indicates that either K^- or π^- can be identified for about 75 % of the events at $M(K\eta) \sim 1.75\text{GeV/c}^2$. Convining these informations and 1-C kinematical fit, the resultant assignment of the charged particle masses is done uniquely for 87.7 % of the events. A two fold ambiguity remains for 11.9 % of the events and 0.4 % have more ambiguities.

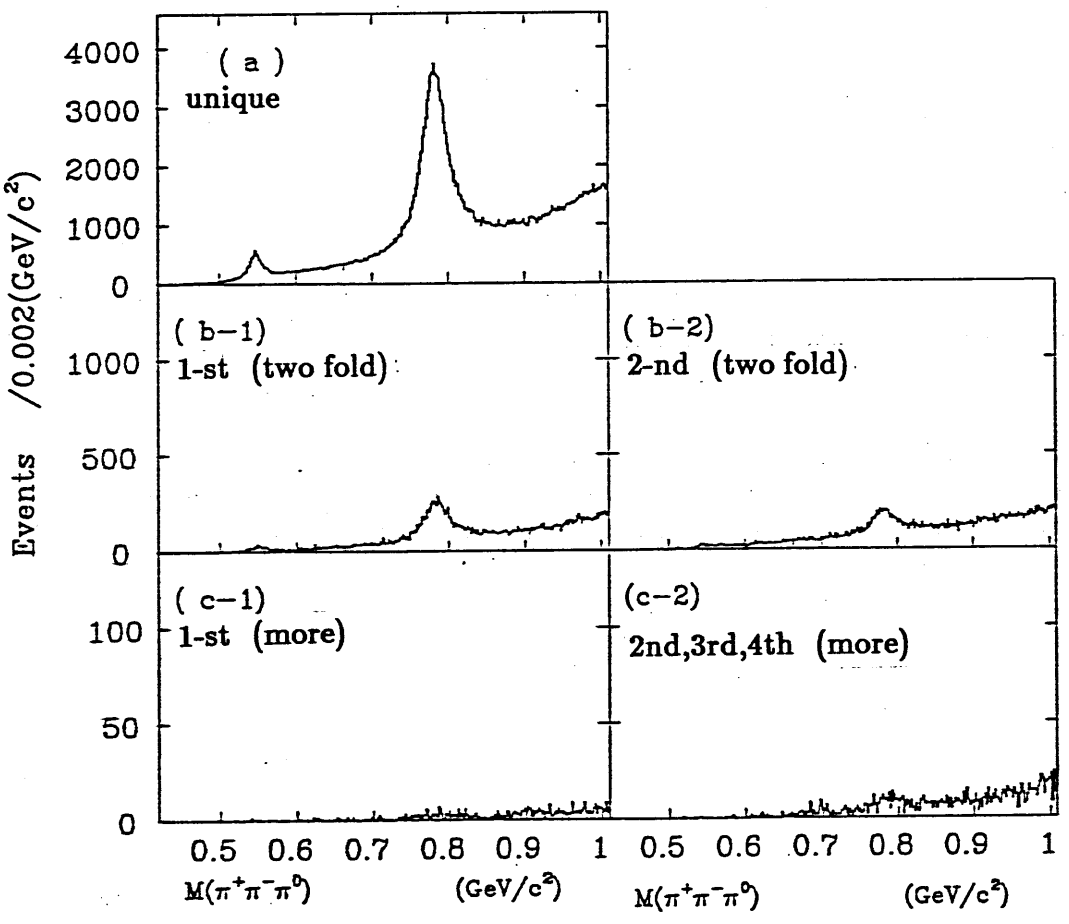

Fig. 35 (a): $M(\pi^+\pi^-\pi^0)$ distribution for events those mass assignment are determined uniquely. (b-1) : The same distribution of the first mass hypothesis and (b-2): second hypothesis for the two-fold ambiguity events. (c-1) : The same distribution of the first mass hypothesis and (c-2) : possible second to fourth mass hypothesis for events have more ambiguity.

The remaining ambiguities for the $\sim$ 12% of events are, finally, resolved by choosing the particle assignment that gives the largest 1-C confidence level. To show the reliability of this choice, each $M(\pi^+\pi^-\pi^\circ)$ distribution of all possible mass assignments for ambiguous events is given in fig. 35 together with the distribution of the events in an unique mass assignment. The loss of the η , ω signal by choosing the first candidate of the mass assignment is 2.5 %, 3 % of total accepted events, respectively. The masses of the charged particles in the reaction (5.1) are determined remarkably well without serious loss of the true events, even though the final state of this reaction is rather complicated.

The summary of the event selection discussed in this chapter is shown in Table-6.

Selection Requirements	Fraction Cut	Removed events	remaining events
1.total triggered events(K^- beam)			$11\cdot10^7$
$K^-\pi^+\pi^-\pi^0 p$ event selection			
2. select 4-prong events ..all 4 tracks are associated to primary ..vertex and $\Delta Q=0$.			$1.87\cdot10^7$
3. apply loose kinematical requirements $-0.30GeV^2<MM^2(K^-\pi^+\pi^-p)^{\nu}\leq 0.30GeV^2$ $\lvert t_{(p-p)}\rvert^{\nu} \leq 2.0\ GeV^2$			
4. $M(\pi^+\pi^-\pi^0)^{\nu}\leq 1.1GeV$			3177512
5. geometry fit is converged.	0.004	12083	3165429
6. 4-C event cut. Cut if $C.L._{4\text{-}C}\geq 1.0^{-10}$	0.408	1291145	1874284
7. good 1-C fit.($K^-\pi^+\pi^-\pi^0 p$) Accept if $C.L._{1\text{-}C}\geq 1.0^{-10}$	0.252	472023	1402261
8. particle identification.	0.269	354306	1047955
9. primary vertex is inside target.	0.003	2899	1045056
10. remove V^0(γ) events	0.072	75450	969606
11. 1-C tight cut. Accept if $C.L._{1\text{-}C}\geq 0.01$	0.143	146744	822862
12. $\frac{dE}{dx}$ cut	0.094	77484	745378
13. tight π^0 cut. $-0.15GeV^2<MM^2(K^-\pi^+\pi^-p)_{raw}\leq 0.10GeV^2$	0.218	162287	583092
$K^-\eta p$ event selection			
14. select $K^-\eta p$ events $0.520GeV<M(\pi^+\pi^-\pi^0)\leq 0.570GeV$	0.987	575466	7626
15. remove N^* . Cut if $M(\eta p)\leq 2.00GeV$	0.388	2959	4667
16. remove Y^*. Cut if $M(Kp)\leq 1.85GeV$	0.155	725	3942
17. limit t region . $0.08GeV^2<\lvert t\rvert\leq 1.0GeV^2$	0.260	1024	2918

Table-6 The summary of the event selection on the reaction $K^-p \rightarrow K^-\pi^+\pi^-\pi^0 p$.

5.6 The general feature of the $K^-\pi^+\pi^-\pi^\circ p$ system.

The three pion mass $M(\pi^+\pi^-\pi^\circ)$ spectrum of final 583092 $K^-\pi^+\pi^-\pi^\circ p$ sample shows clear indication of the η and ω (fig. 36). The same plot with expanded η region is shown in fig. 37.

The solid curve supperposed is a fit by resolution functions plus background parametrized by third-order polinomial functions. Double Gaussians having a common center is used as resolution function to reproduce each signal shape:

$$\left(\frac{d\sigma}{dM}\right) = a_{R_1} \cdot exp\left(-\frac{(\mathrm{M}-\mathrm{M_R})^2}{2\cdot\sigma^2_{\mathrm{R}_1}}\right) + a_{R_2} \cdot exp\left(-\frac{(\mathrm{M}-\mathrm{M_R})^2}{2\cdot\sigma^2_{\mathrm{R}_2}}\right) \qquad (5.7)$$

where M is invariant mass of $\pi^+\pi^-\pi^\circ$ and $a_{R_1}, a_{R_2}, \mathrm{M_R}, \sigma_{\mathrm{R}_1}, \sigma_{\mathrm{R}_2}$ are parameters to be determined by the fit. The fit results are summarized in table-7. The results of the fit with single Gaussian are also shown for comparison.

Table-7: The parameters fit $\pi^+\pi^-\pi^\circ$ distribution.

Resonance	Gaussian	$\mathrm{M_R}$ (MeV/c^2)	σ_{R_1} (MeV/c^2)	σ_{R_2} (MeV/c^2)	a_{R_2}/a_{R_1}
η	double	548.0 ± 0.4	6.4 ± 0.8	16 ± 2	0.51 ± 0.18
	single	548.1 ± 0.4	9.7 ± 0.3		
ω	double	782.7 ± 1.1	13 ± 1	31 ± 1	0.58 ± 0.04
	single	783.0 ± 1.0	19 ± 1		

The mass positions are in good agreement with the world average value of η and ω resonances, and the width is consistent with the spectrometer resolution.

There are 7626 events in the η mass region $0.520\mathrm{GeV/c^2} < M(\pi^+\pi^-\pi^\circ) \leq 0.570\mathrm{GeV/c^2}$ (fig.37) and the signal to noise ratio of this signal is about 1:1 . The number of this η sample after background subtraction is one order of magnitude larger than any other previous experiments[9].

In the following sections I discuss the overall acceptance and resolutions of $K\eta$ system and the absolute normalization of this experiment after describing the Monte Calro simulation.

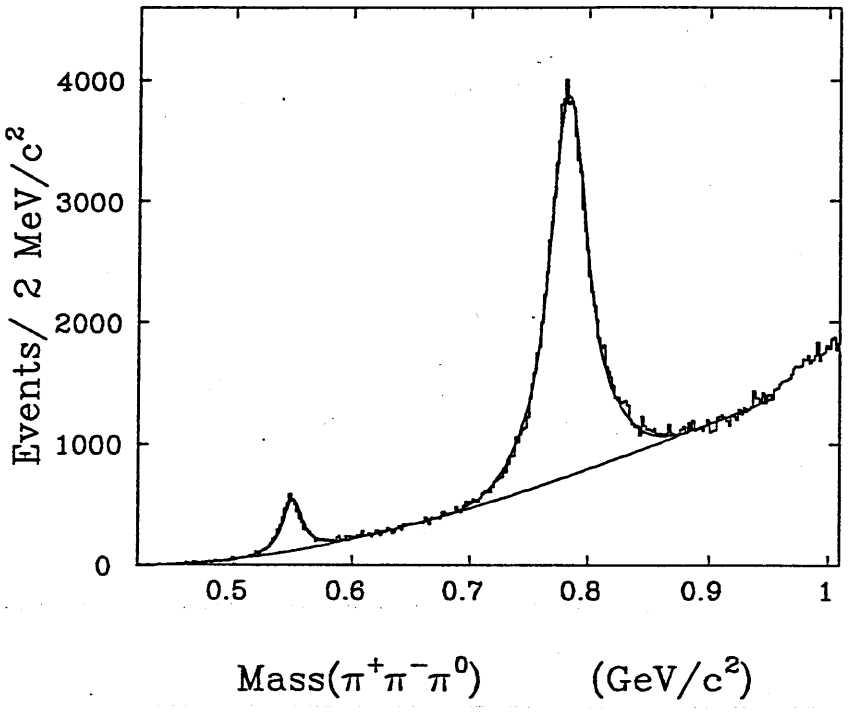

Fig. 36 The $\pi^+\pi^-\pi^\circ$ effective mass distribution of final sample showing clear η and ω signal. The solid line is a fit by the resolution functions of double Gaussian form plus background term parametrized by third order polinomial function.

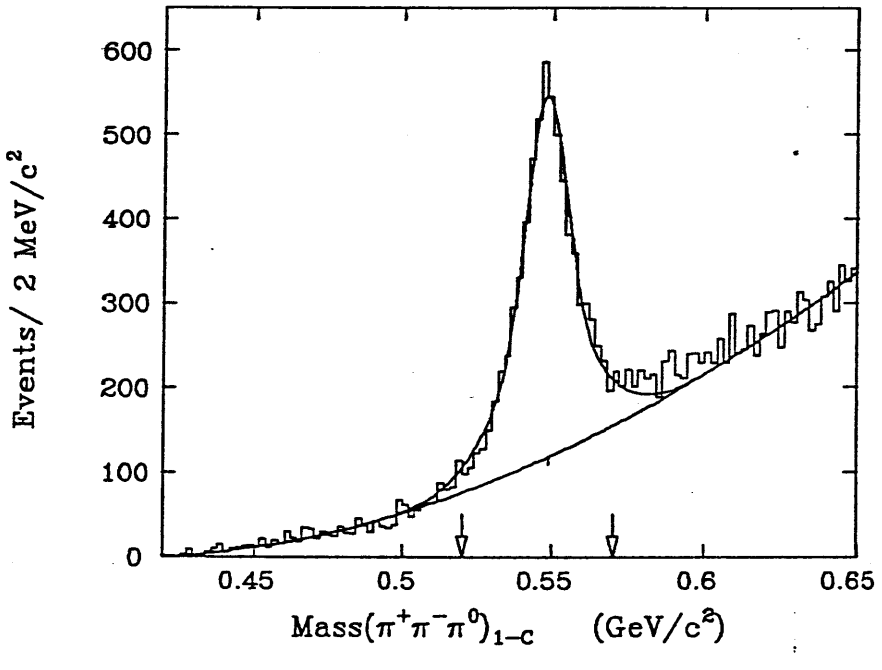

Fig. 37 The $\pi^+\pi^-\pi^\circ$ effective mass distribution of η mass region. Arrow indicate the η region used in the analysis.

5.7 The Monte Calro simulation

Although the geometrical acceptance of the LASS spectrometer covers most of the 4π solid angle acceptance, the acceptance corrections are carried out to take into account the resolution and efficiency of detectors, decay and absorption of particles and cuts applied in defining the sample. The Monte Calro events of the $K^-\eta p$ reaction are thrown flat in $M(K^-\eta)$ and in t-channel helicity angles, and with an exponential $|t'_{p-p}|$ dependence of slope $4.0/(\mathrm{GeV/c})^2$, which approximately match to the real event distribution.

Each tracks of these generated events are processed through the simulation program of LASS spectrometer described in Appendix-2. In this simulation program, many attentions are payed on particle tracking and the detector response, to reproduce the realistic performance of the LASS spectrometer. The results of the simulation are given at the level of the raw coordinates with exactly same format of the real data. Then these events are processed by the same programs of event reconstruction, kinematical fitting and the later event analysis programs used in the real data to determine the acceptance. After correcting the acceptance by these M.C. events, more realistic mass and angular distribution is reproduced by weighting to the M.C. events. (see Capter 5.2)

The comparison of η signal between data and Monte Calro is displayed in fig.38, where histogram shows the data distribution after subtracting the background. In this subtraction, the background parametrized by third-order polinomial (see Fig.37) is used. Monte Calro distribution is supperposed by closed circle. The agreement between data and Monte Calro is good.

5.8 Overall Acceptance

The effects of the cuts used to selected the $K^-\eta p$ sample is summarized in Table-8.

The overall acceptance is mainly determined by 4 prong requirements and tight cut of 1-C fit which is applied to reduce the ambiguity of mass assignments. The effects of other cuts are small. The difficulty to detect the slow proton is main reason of the loss in the 4 prong requirement. With this reason, the acceptance is rapidly changed in the

small $|t'_{p-p}|$ region as shown in fig. 39. The loss of the η signal by tight 1-C requirement is roughly consistent with the estimated η signal loss in the real data. The overall accetance (fig. 40) smoothly changes from 0.32 to 0.34. It is noted that the acceptance does not drop even if in the high $M(K^-\eta)$ mass region around $\sim 2.4\text{GeV/c}^2$.

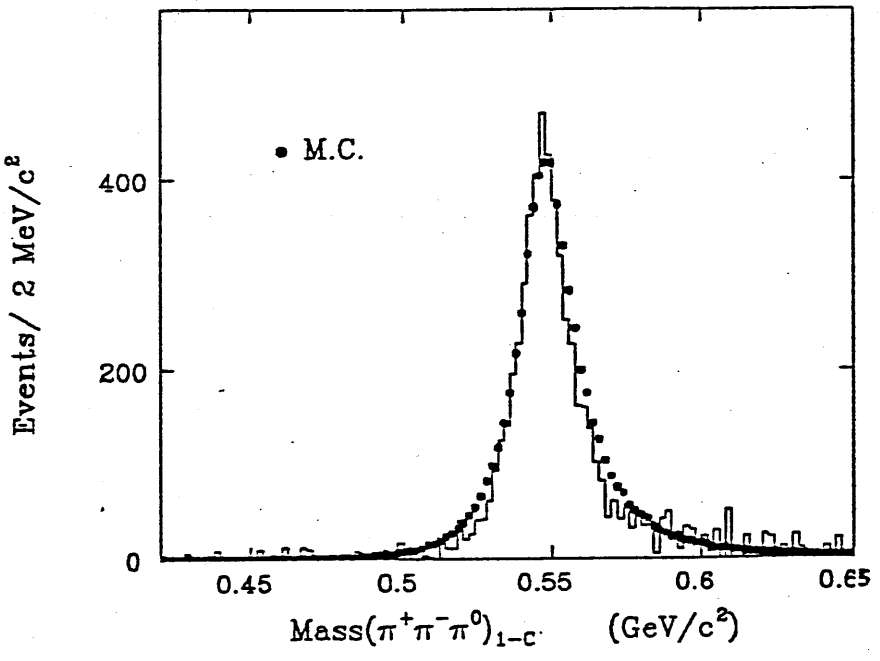

Fig. 38 Background subtracted $M(\pi^+\pi^-\pi^\circ)$ distribution in the η region. Histogram shows the data distribution after background subtraction. Monte Calro distribution is shown by closed circle. In this Monte-Calro the decay angular distribution of real data is also taken into account.

	$1.4GeV<m(K^-\eta)\leq 1.5GeV$		$1.7GeV<m(K^-\eta)\leq 1.8GeV$	
Selection Requirements	Fraction Cut	Accumlative acceptance	Fraction Cut	Accumlative acceptance
1. event trigger	0.026	0.974	0.016	0.984
2. 4-prong events				
..4 tracks associate to beam	0.481	0.520	0.468	0.535
..vertex and $\Delta Q=0$.	0.026	0.506	0.022	0.523
3. apply loose kinematical cut. $-0.30GeV^2<MM^2(K^-\pi^+\pi^-p)^v\leq 0.30GeV^2$ $\lvert t_{(p-p)}\rvert^v \leq 2.0\ GeV^2$	0.012	0.494	0.017	0.507
4. geometry fit is converged.	0.001	0.493	0.001	0.506
5. 4-C event cut Cut if $C.L._{4\text{-}C}\geq 1.0^{-10}$	0.053	0.466	0.033	0.490
6. good 1-C fit. Accept if $C.L._{1\text{-}C}\geq 1.0^{-10}$	0.031	0.452	0.033	0.474
7. particle identification	0.030	0.434	0.036	0.457
8. target region cut.	0.001	0.432	0.001	0.456
9. tight π^0 cut. $-0.15GeV^2<MM^2(K^-\pi^+\pi^-p)_{raw}\leq 0.10GeV^2$	0.062	0.407	0.088	0.416
10. remove $V^0(\gamma)$ events	0.056	0.384	0.047	0.397
11. 1-C tight cut. Accept if $C.L._{1\text{-}C}\geq 0.01$	0.106	0.344	0.104	0.356
12. select $K^-\eta p$ events $0.520GeV<M(\pi^+\pi^-\pi^0)\leq 0.570GeV$	0.046	0.328	0.033	0.341
13. N^* cut	0.002	0.328	0.039	0.327
14. Y^* cut	0.002	0.327	0.033	0.317

Table-8 Effects of the event selection on the acceptance. The table list the effect of the selection criteria on the $K^-p \rightarrow K^-\eta p$ for $K^-\eta$ mass around 1.45 and 1.75 GeV. The cuts are descibed in the preceding section.

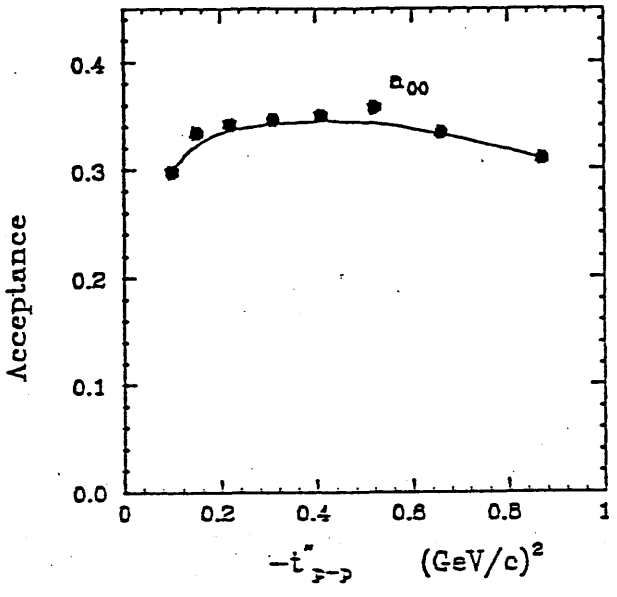

Fig. 39 The acceptance as a function of $|t'_{p-p}|$

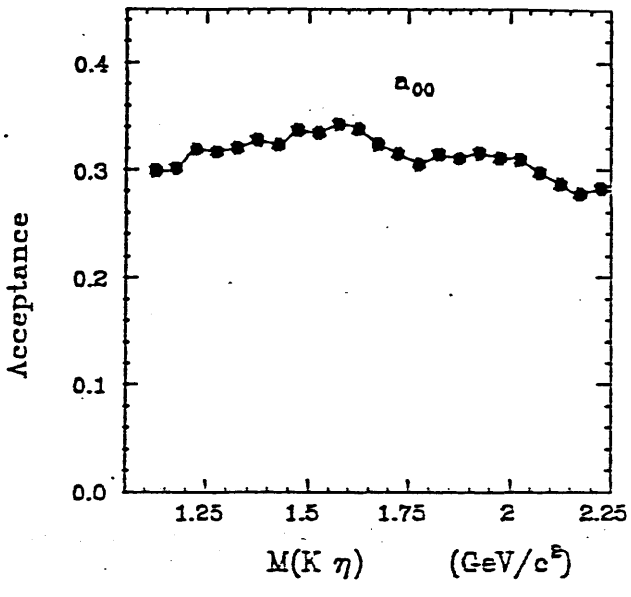

Fig. 40 The acceptance as a function of $M(K^-\eta)$. The acceptance after appling all cuts are shown. The effect of N^* and Y^* resonance cuts and the limit of the $|t'_{p-p}|$ region are taken into account.

5.9 Kinematics and Resolutions

The kinematics of the reaction $K^-p \to K^-\eta p$ can be completely specified by four kinematical variables in a given beam momentum experiment, since η is $J^p = 0^-$ particle and target is not porlarized. The convenient these four variables are the invariant mass of $K^-\eta$ system $M(K^-\eta)$, the momentum transfer from target to proton minus its minimum $|t'_{p-p}| = |t_{p-p} - t_{min}|$ and two decay angles $\cos\theta_{GJ}$ and ϕ_{GJ} of the K^- direction in the t-channel helicity frame. (Gottfried- Jackson frame). The definition of these angles is illustrated in fig.41.

The resolution of the invariant mass $M(K^-\eta)$ changes from 18 MeV/c^2 to 22 MeV/c^2 depending on the $K^-\eta$ effective mass as shown in fig. 42. The $|t'_{p-p}|$ resolution varies from 0.016 to 0.020 (GeV/c)^2 depending on the $K^-\eta$ mass from 1.1 GeV/c^2 to 2.3 GeV/c^2 . The resolution of decay angles $\cos\theta_{GJ}$ and ϕ_{GJ} are about 0.02 and 0.03 radian , respectively. These resolutions are accurate enough to make a precise angular analysis in the next chapter.

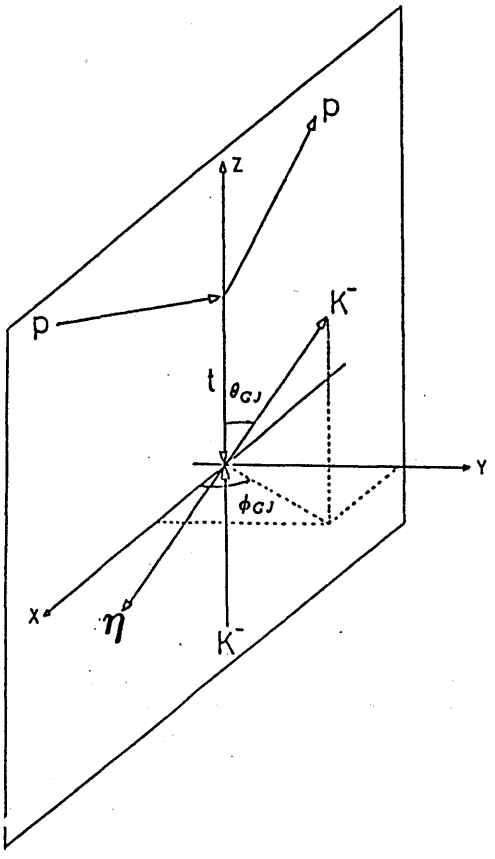

Fig. 41 The definition of the decay angles $\cos\theta_{GJ}, \phi_{GJ}$ in the t-channel helicity frame.

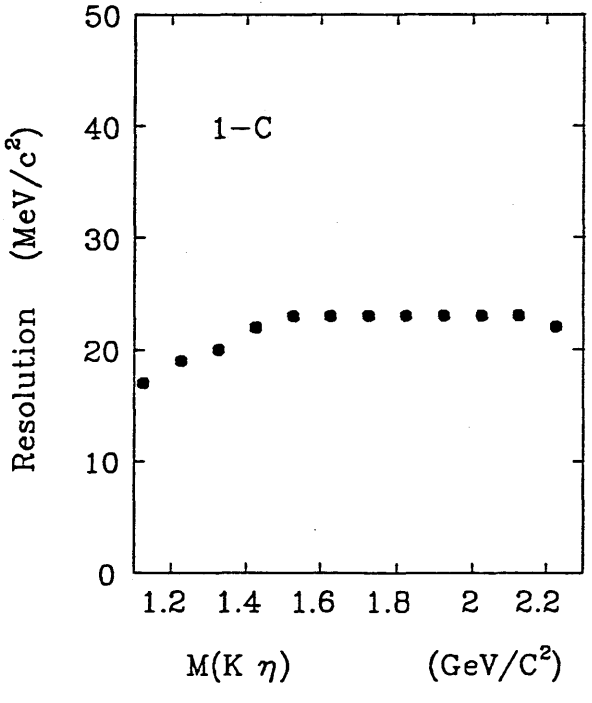

Fig. 42 The resolution of the invariant mass of $K^-\eta$ as a function of $M(K^-\eta)$.

5.10 The sensitivity of the experiment

The sensitivity of the experiment is defined as

$$S = N_{beam}\rho_p L\eta_{cor}$$

where N_{beam} is the number of beam particles enter the target, ρ_p is the number of protons/cm^3 in the target and L is the length of the target. Finally η_{cor} is a correction factor comes from beam decay, electronics dead time and event processing loss.

The total number of K^- beam particles over the course of the experiment is $N_{beam} = 1.469 \times 10^9 \pm 0.3\%$. The effect of the spectrometer dead time have been taken into account in this value. The correction of another effect are summarized following table : Table-9.

Table-9: The corrections to the raw beam flux.

Type of Correction	Size of Correction
Beam decay before entering target	0.983 ± 0.002
Beam interaction or decay in target	0.954 ± 0.002
Electronics and trigger deadtime	0.996 ± 0.010
Event processing losses	0.882 ± 0.020
Total corrections	0.768 ± 0.026

The target proton density ρ_p averaged over the course of the experiments is $4.728 \cdot 10^{22} \pm 0.5\%$ cm^{-3} . The target length at the liguid H_2 temperature is estimeted to be $L = 84.6 \pm 0.2$ cm.

The resultant sensitivity in the K^- beam experiment is :

$$S = 4.082 \pm 2.7\% \text{ events/nb}$$

6. Angular moment analysis

6.1 The general features of the $K\eta$ system

M($K^-\eta$) distribution.

Selecting the η mass region in $0.520\text{GeV/c}^2 < M(\pi^+\pi^-\pi^\circ) \leq 0.570\text{GeV/c}^2$ which contain 7626 events , the $K^-\eta$ effective mass spectrum (fig. 43) shows a prominent peak around 1.75GeV/c^2, and no other significant structure is observed in the other mass region. In particular, there is no structure in the $K_2^*(1430)$ region.

N^*, Y^* background

In the dalitz plot of the final state $K^-\eta p$ (fig.44), we can see this prominent peak as an intense band. Other intense bands seen in the low ηp and K^-p mass region of this dalitz plot come from the diffractive processes :

$$\begin{aligned} K^-p &\to K^-N^* \\ K^-p &\to Y^*\eta \end{aligned} \tag{6.1}$$

These processes are contributing to the high mass region of $K^-\eta$ system.

These N^* and $Y^*(\Sigma^*/\Lambda^*)$ resonances are eliminated from the sample used in the angular analysis of $K^-\eta$ system with the cuts

$$\begin{aligned} M(\eta p) &\leq 2.00\text{GeV/c}^2 \\ M(K^-p) &\leq 1.85\text{GeV/c}^2 \end{aligned} \tag{6.2}$$

The positions of cuts are shown in the effective mass distributions of ηp (fig. 45) and K^-p (fig. 46), respectively. The resultant $K^-\eta$ distribution is shown by the shaded histogram in Fig.43. The high $M(K^-\eta)$ mass region contains the reflections of these N^*, Y^* productions, but low mass region $\leq 1.80\text{GeV/c}^2$ is free from these reflections.

The angular distribution around $M(K\eta) \sim 1.75\text{GeV/c}^2$

The polar $\cos\theta_{GJ}$ and azimuthal ϕ_{GJ} angular distributions in a prominent peak region ($1.70\text{GeV/c}^2 < M(K\eta) \leq 1.80\text{GeV/c}^2$) are shown in fig.47 and fig.48 for

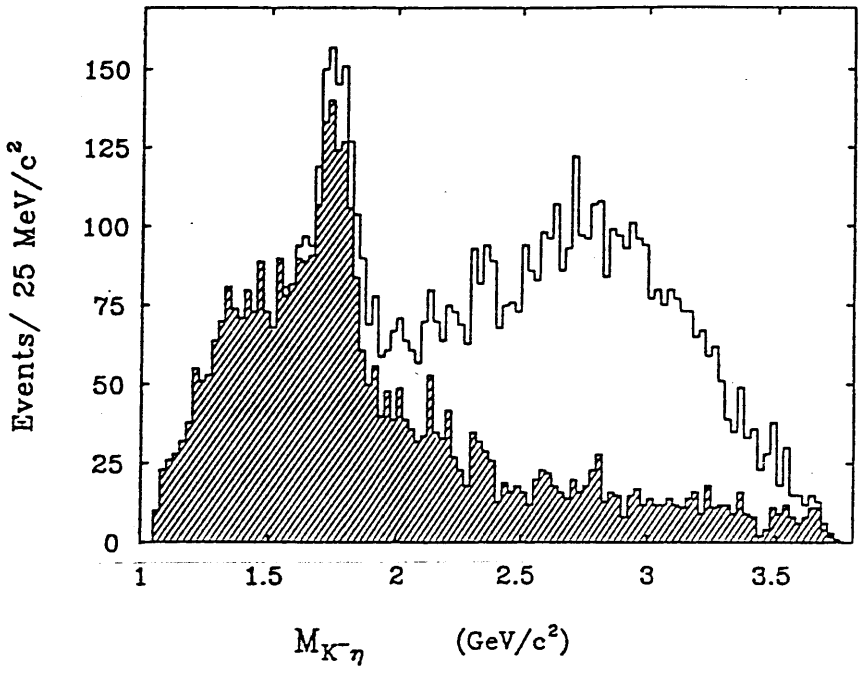

Fig. 43 The $K^-\eta$ effective mass distribution. The inner histogram shows the results after the diffractive background are removed by requiring $M(\eta p) > 2.00\text{GeV/c}^2$ and $M(K^- p) > 1.85\text{GeV/c}^2$.

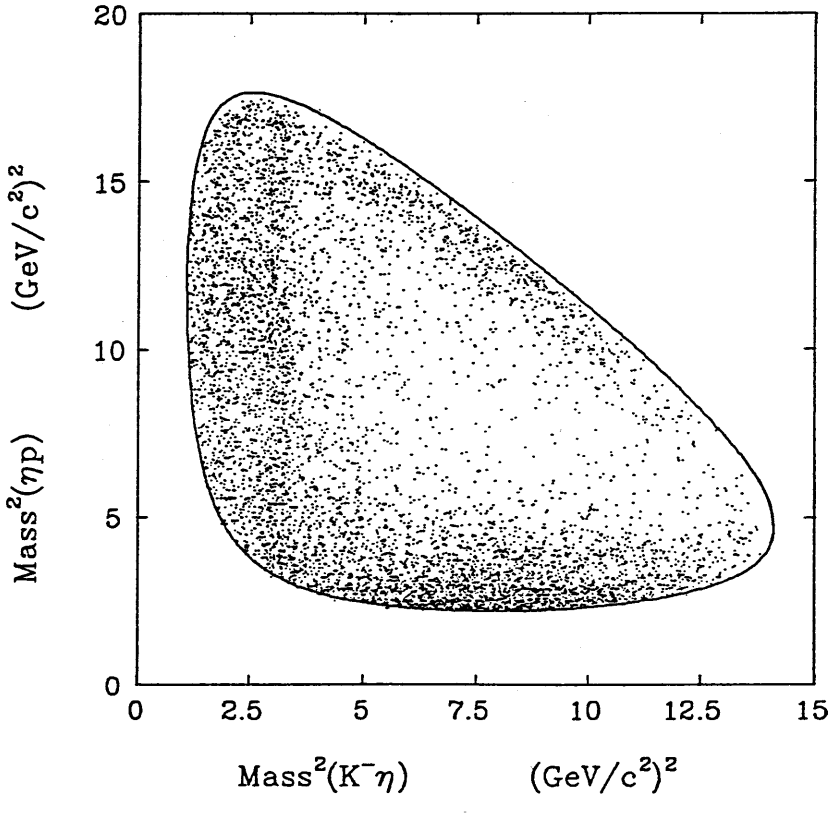

Fig. 44 The Dalitz plot of the reaction $K^- p \to K^- \eta p$.

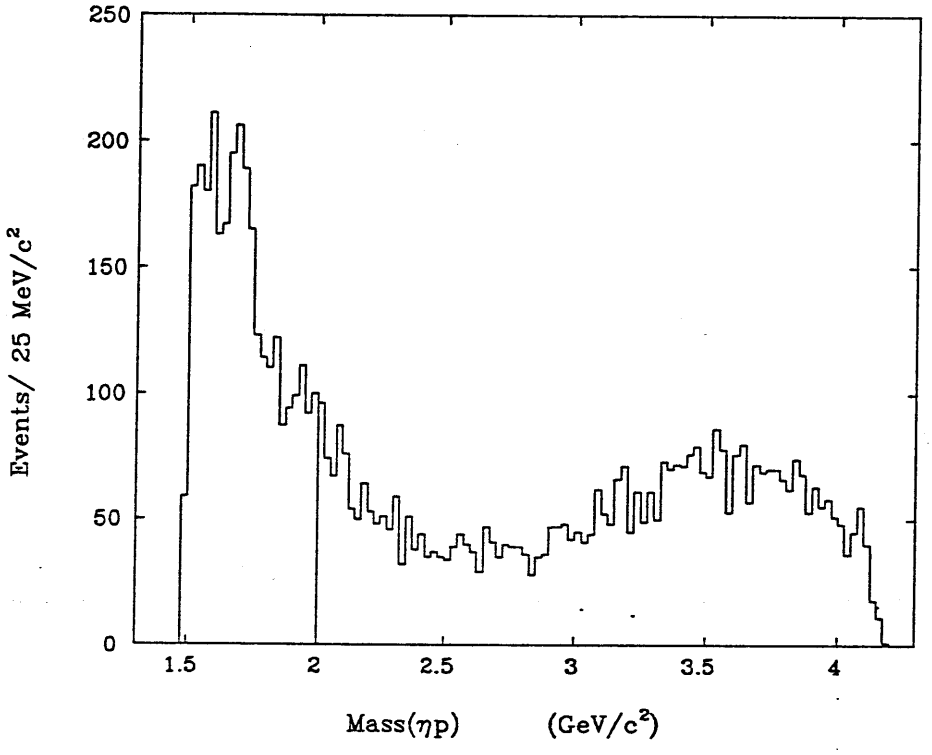

Fig. 45 The ηp effective mass distribution. The solid line indicate cut position to remove N^* contamination.

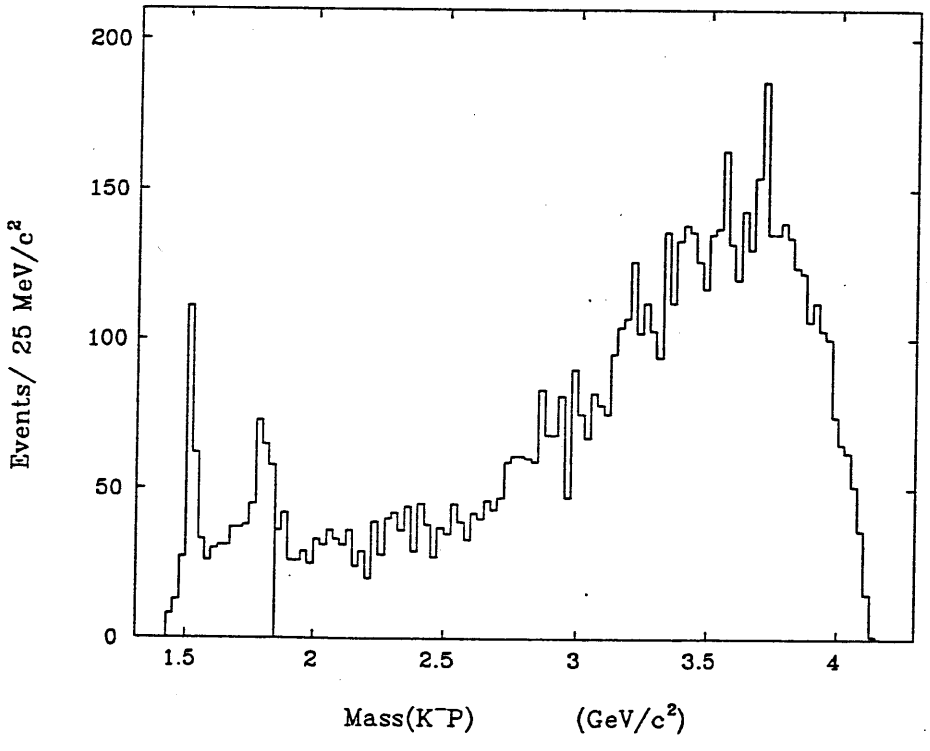

Fig. 46 The $K^- p$ effective mass distribution. Two clear peaks of $Y^*(\Sigma^*/\Lambda^*)$ resonance are seen in low $M(K^- p)$ mass region. Solid line indicate the cut position used to remove these Y^* contaminations.

the events after appling N^* and Y^* cuts and limiting the $|t'_{p-p}|$ region between 0.08 GeV/c^2 and 1.00 GeV/c^2 . In these figures, non-acceptance corrected and acceptance corrected distributions are presented to demonstrate the uniform nature of angular acceptance in this mass region.

Both $\cos\theta_{GJ}$ and ϕ_{GJ} distributions show clear structures. In particular, the azimuthal symmetry observed in fig.48 is confirmation of parity conservation in the production and decay process. The depopulation at $\sim \pm 180°$ and at $\sim 0°$ indicate that helicity 1 natural parity exchange gives an important contribution to the t-channel production.

6.2 Angular Moment analysis

In order to determine the spin of this prominent peak around 1.75GeV/c^2 and also to search another structure in this system, the mass dependence of the angular distribution of $K^-\eta$ system is studied quantitatively for $K^-\eta$ mass region below 2.3GeV/c^2 and in the $|t'_{p-p}|$ region between 0.08 GeV/c^2 and 1.00 GeV/c^2 . The lower $|t'_{p-p}|$ region is removed in this analysis since the reconstruction of slow proton is difficult.

This angular analysis is carried out in the succeeding two steps. In the first step, the decay angular distribution of this system is expressed in terms of spherical harmonic moments, and in the second step, this moments is decomposed into the production amplitudes. Following sections are devoted on the first step of the moment analysis and the second step will be discussed in the next chapter.

6.3 Basic Formula of moment analysis

The acceptance corrected decay angular distribution $G(X,\Omega)$ of $K^-\eta$ system can be expressed in terms of the moments t_{lm} of the spherical harmonics,

$$G(X,\Omega) = \frac{1}{4\pi} \sum_{l,m\geq 0} t_{lm}(X) Y'_{lm}(\Omega) \tag{6.3}$$

where we have used the abbreviation $X = (M_{K^-\eta}, |t'_{p-p}|)$ for mass and momentum transter, and used $\Omega = (\cos\theta_{GJ}, \phi_{GJ})$ for the K^- decay angles in the t-channel helicity

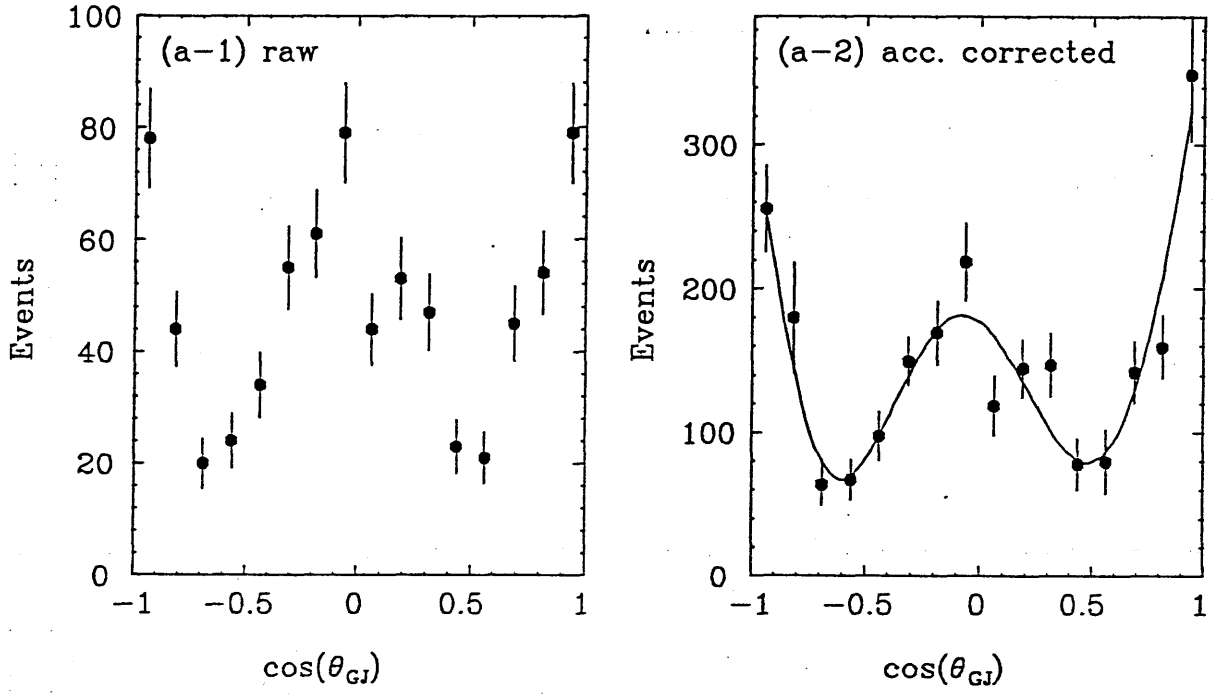

Fig. 47 The (a-1) non-acceptance corrected and (a-2) acceptance corrected $\cos\theta_{GJ}$ distribution in the region $1.70\text{GeV/c}^2 < M(K^-\eta) \leq 1.80\text{GeV/c}^2$ and $0.08 \geq |t'_{p-p}| < 1.00(\text{GeV/c}^2)^2$. The curve supperposed in (a-2) is a fit by the moments with $L_{max} = 8$ and $m_{max} = 2$.

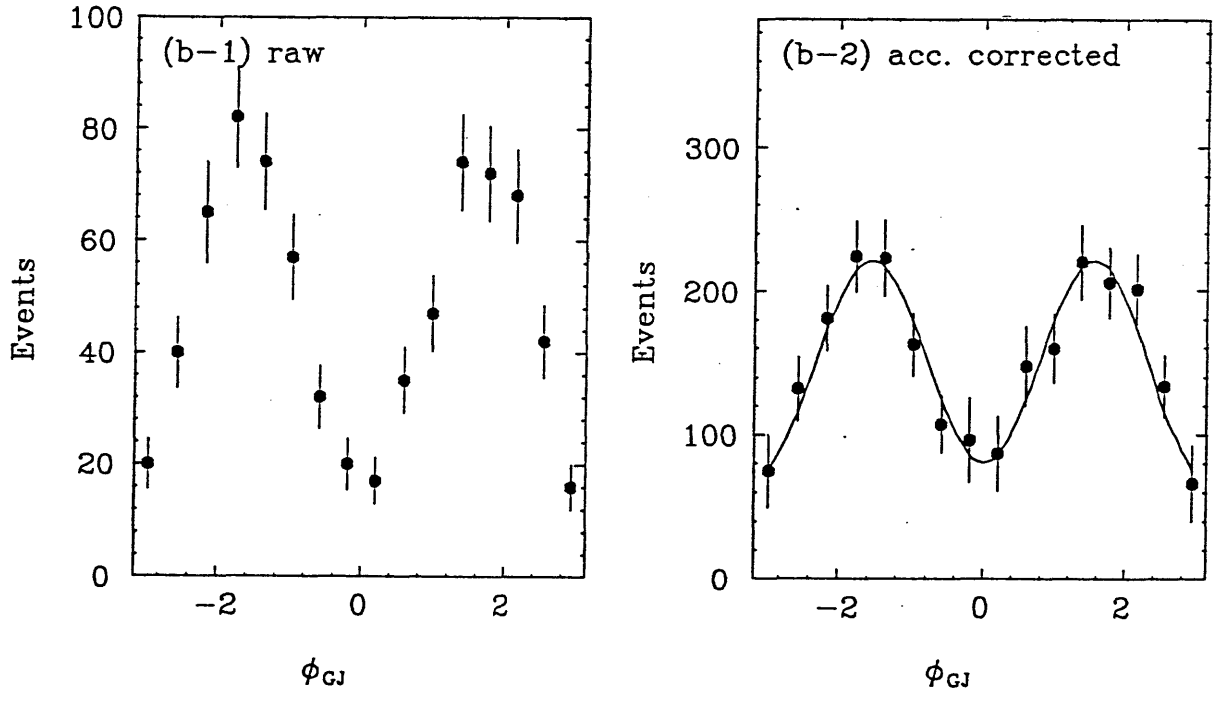

Fig. 48 The (b-1) non-acceptance corrected and (b-2) acceptance corrected ϕ_{GJ} distribution in the same mass region. The curve supperposed in (b-2) is a fit by the moments.

frame (Gottfried-Jackson frame). The $Y'_{lm}(\Omega)$ in this equation stands for the real part of spherical harmonic function:

$$Y'_{lm}(\Omega) = \epsilon_{lm} Re(Y_{lm}(\Omega)) \tag{6.4}$$

with $\epsilon_{lm} = 1$ for $m = 0$ and $\epsilon_{lm} = 2$ for $m \neq 0$, respectively. This simplication results from the parity conservation in the strong interaction process. In this thesis, we use $Y_{00}(\Omega) = 1$ as a normalization condition of harmonic functions. With this definition, t_{00} moment corresponds to the acceptance corrected total number of events in each bin of mass $M_{K^-\eta}$ and $|t'_{p-p}|$. The orthogonal condition of Y'_{lm} is given by :

$$\begin{aligned} \int Y'_\lambda(\Omega) Y'_\mu(\Omega) d\Omega &= 4\pi\epsilon_\lambda \delta_{\lambda\mu} \\ \lambda &= (l, m) \\ \mu &= (l', m') \end{aligned} \tag{6.5}$$

where $\delta_{\lambda\mu}$ is Kronecker's delta.

This acceptance corrected distribution $G(X, \Omega)$ is obtained from the observed data distribution $D(X, \Omega)$ by correcting for the spectrometer acceptance $A(X, \Omega)$:

$$D(X, \Omega) = A(X, \Omega) G(X, \Omega) \tag{6.6}$$

This acceptance correction are carried out by expressing the distributions in terms of spherical harmonic moments. Multipling both side of eq.(6.6) by $Y'_\mu(\Omega)$ and integrating over Ω using the orthogonal condition eq.(6.5), we can obtain a set of linear equations in each bin of the variables $X = (M_{K^-\eta}, |t'_{p-p}|)$:

$$\epsilon_\lambda r_\lambda = \sum_\mu A_{\lambda\mu} t_\mu \tag{6.7}$$

where r_λ are raw data moments defined by the form :

$$\begin{aligned} r_\lambda &= \frac{1}{\epsilon_\lambda} \int D(\Omega) Y'_\lambda(\Omega) d\Omega \\ &\sim \frac{1}{\epsilon_\lambda} \sum_i^N Y'_\lambda(\Omega_i) \end{aligned} \tag{6.8}$$

As can be seen from the second equation of (6.8), the raw data moment is the simple summation of the event weighted value of the spherical harmonic function $Y'_\lambda(\Omega_i)$.

$A_{\lambda\mu}$ in (6.7) are acceptance correlation matrix defined by the equations:

$$A_{\lambda\mu} = \frac{1}{4\pi} \int A(\Omega) Y'_{\lambda}(\Omega) Y'_{\mu}(\Omega) d\Omega \tag{6.9}$$

This correlation matrix can be calculated by the Monte Calro method.

Taking matrix inversion of eq.(6.7), the acceptance corrected moments t_μ are determined from raw data moments r_λ and the acceptance correlation matrix $A_{\lambda\mu}$:

$$t_\mu = (A_{\lambda,\mu})^{-1} \epsilon_\lambda r_\lambda, \tag{6.10}$$

and the corresponding error matrix $\mathbf{E}$ for t_μ is given by the equation

$$\mathbf{E} = \mathbf{A^{-1}} \mathbf{D} (\mathbf{A^{-1}})^{\mathbf{T}} \tag{6.11}$$

where $\mathbf{D}$ corresponds to the error matrix of the raw data moments :

$$\begin{aligned} D_{\lambda\mu} &= \frac{\partial \epsilon r}{\partial Y'_{\lambda} \partial Y'_{\mu}} \\ &= \int D(\Omega) Y'_{\lambda}(\Omega) Y'_{\mu}(\Omega) d\Omega \\ &\sim \sum_{i=1}^{N} Y'_{\lambda}(\Omega_i) Y'_{\mu}(\Omega_i) \end{aligned} \tag{6.12}$$

6.4 The acceptance correction

The determination of the acceptance correlation matrix $A_{\lambda\mu}$ is performed by Monte Calro method. In the Monte Calro, the integral of eq.(6.9) is calculated by the summation of each Monte Calro event:

$$A_{\lambda\mu} \sim \frac{1}{N_{Gen}} \sum_{i=1}^{N_{Obs}} Y'_{\lambda}(\Omega_i) Y'_{\mu}(\Omega_i) \tag{6.13}$$

where N_{Gen} is the total number of generated events and N_{Obs} is the number of observed events passed all the same cuts applied to the real data. This summation is approximately equal to the integral if enough number of events are generated.

In a strict sence, however, since the resolution of the spectrometer is limited, the smearing effect due to the finit resolution of kinematical variables may be taken into account in the calculation of the acceptance. If we take this effect into account, the equation (6.13) is modified to:

$$A_{\lambda\mu} = \frac{1}{N_{Gen}} \sum_{i=1}^{N_{obs}} \left(\frac{G(X_i^G, \Omega_i^G)}{G(X_i^R, \Omega_i^R)} \right) Y_\lambda'(\Omega_i^R) Y_\mu'(\Omega_i^R) \tag{6.14}$$

where the superfices R and G refer to reconstructed and generated quantities. In this formula, since the production distribution $G(X, \Omega)$ does not known in prior, the acceptance matrix and angular moments t_{lm} should be determined iteratively. The acceptance matrix determined with the flat angular distribution is used as an initial estimation of the acceptance matrix. Using this matrix, the acceptance corrected moments t_{lm} can be determined and more realistic production distribution $G(X, \Omega)$ is obtained from these t_{lm}. This iteration is repeated until further iteration does not seem to change the results. In practice, this iteration has reasonably converged in a few times.

The number of events generated by the M.C. is at least 20 times larger than the real data in each mass bin. The obtained overall mass acceptance A_{0000} is already shown in fig.40. The wiggle seen around $M(K^-\eta) \sim 1.75\text{GeV/c}^2$ is smearing effects due to the finite resolution of the spectrometer. For another acceptance correlation moments, the moments with small l (≤ 2) are only significant and those are changed smoothly as a function of mass.

6.5 The Background

Since signal to noise ratio of η signal is about 1:1, the estimation of the non-η background lies underneath η resonance is important to obtain the true moments of $K\eta$ system. To estimate this background, the behavior of each moment is studied in the wide three pion mass $M(\pi^+\pi^-\pi^\circ)$ region. Then the background is determined by interpolating the shape of the moment in the η wing region into η mass region. The detail procedure is as follows.

The K^- decay angles of $\cos\theta_{GJ}$ and ϕ_{GJ} can be defined in the rest frame of $K^-\pi^+\pi^-\pi^\circ$ system in the reaction $K^-p \to K^-\pi^+\pi^-\pi^\circ p$. Therefore the raw data

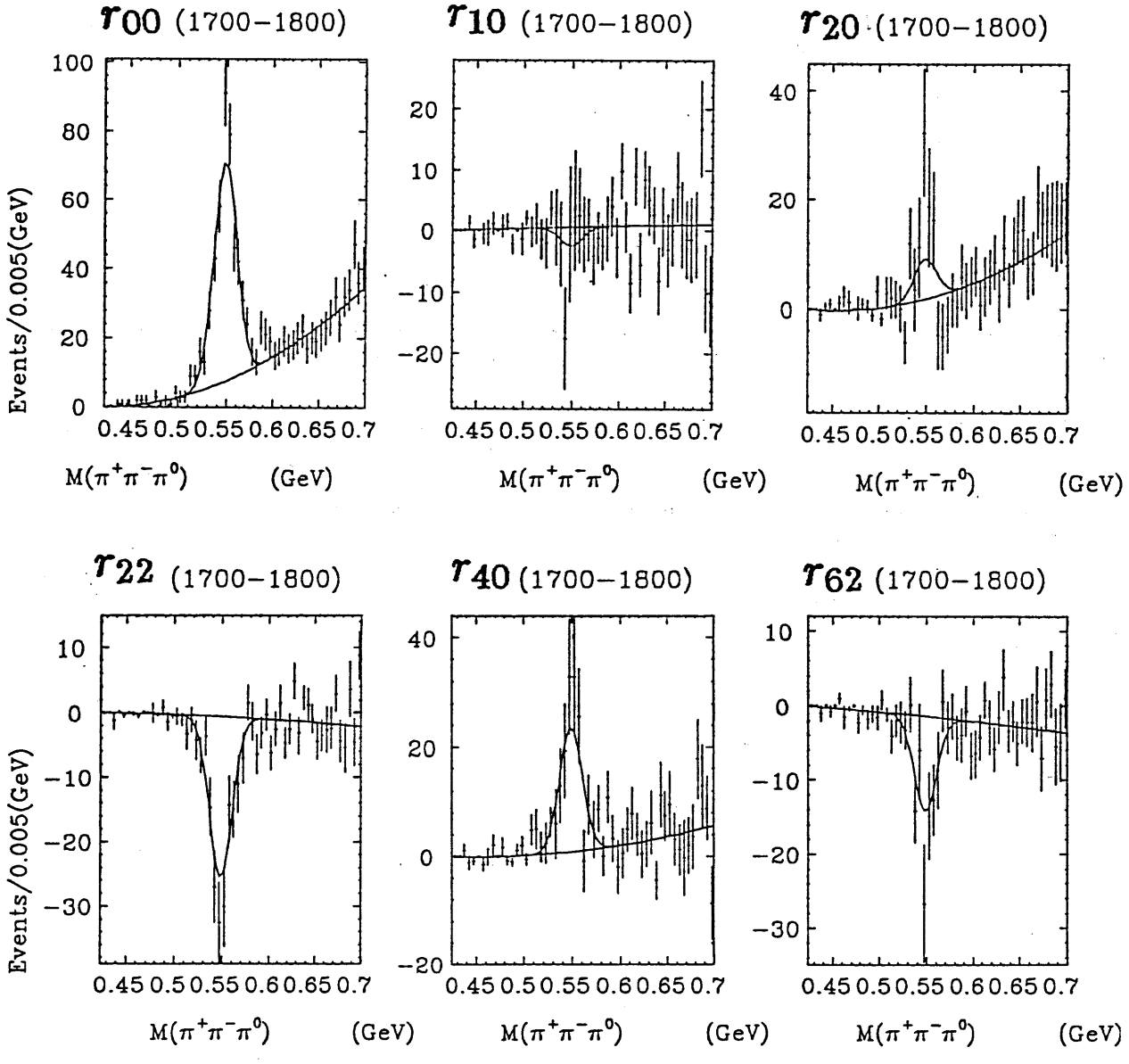

Fig. 49 The raw data moments as a function of $M(\pi^+\pi^-\pi^\circ)$ in the $K^-\pi^+\pi^-\pi^\circ$ mass region between $1.7 - 1.8 \mathrm{GeV/c^2}$.

moments r_{lm} in this system can be obtained in any mass $M(\pi^+\pi^-\pi^\circ)$ region by the equation (6.8). In the first step of the background estimation, these raw data moments are evaluated as a function of $M(\pi^+\pi^-\pi^\circ)$ in each 100MeV/c^2 bin of $M(K^-\pi^+\pi^-\pi^\circ)$. The bin width of $M(K^-\pi^+\pi^-\pi^\circ)$ is twiced the bin size normally used in the analysis of η mass region to guarantee the statistics. 50MeV/c^2 bin step is used in the analysis of η region. The typical distributions of raw data moments are shown in fig.49for the $K^-\pi^+\pi^-\pi^\circ$ mass region between 1.70GeV/c^2 – 1.80GeV/c^2. The structure caused by η resonance is observed clearly in the moments $r_{00}, r_{20}, r_{22}, r_{40}$ and r_{62}.

In the next step, each raw data moment is fitted with a Gaussian resolution function for η signal plus a second order polynomial to separate the background. The result of fit is supperposed in each figure of Fig.49. In this fit, the sigma of the Gaussian is fixed to a typical resolution of η signal in each mass bin. The background components in the η mass region are, then, determined by integrating the background terms over the η mass region (0.52GeV/c^2 $< M(\pi^+\pi^-\pi^\circ) \leq$ 0.57GeV/c^2). In the third step, the acceptance correction of these background moments are performed using equation (6.10) . The final step is the estimation of the error of this background moment. This error is calculated from the error of the background terms in the Gaussian fit and its acceptance correction is carried out using the equation (6.11).

6.6 The Moments as a function of $K^-\eta$ mass

The $K^-\eta$ mass dependence of the acceptance corrected moments in the $|t'_{p-p}|$ interval between 0.08(GeV/c)^2 and 1.00(GeV/c)^2 are shown in fig.50. Here closed circle with error bar is the moments in the η signal region and histograms show non η background contribution. The background is smooth in mass and only moments with small l are significant. The acceptance corrected and background subtracted $K\eta$ mass distribution (t_{00} moment) is shown in fig.51.

We can see clear bump structure in the moments of $t_{00}, t_{20}, t_{22}, t_{40}$ and t_{62} for the mass region $\sim$ 1.75GeV/c^2 . Since moments with $l > 6$ or $m > 2$ are not significant, these structures are the indication of the presence of a spin 3 resonance. There is no evidence for significant structure elsewhere. Especially, again, no evidence of $K_2^*(1430)$ is seen.

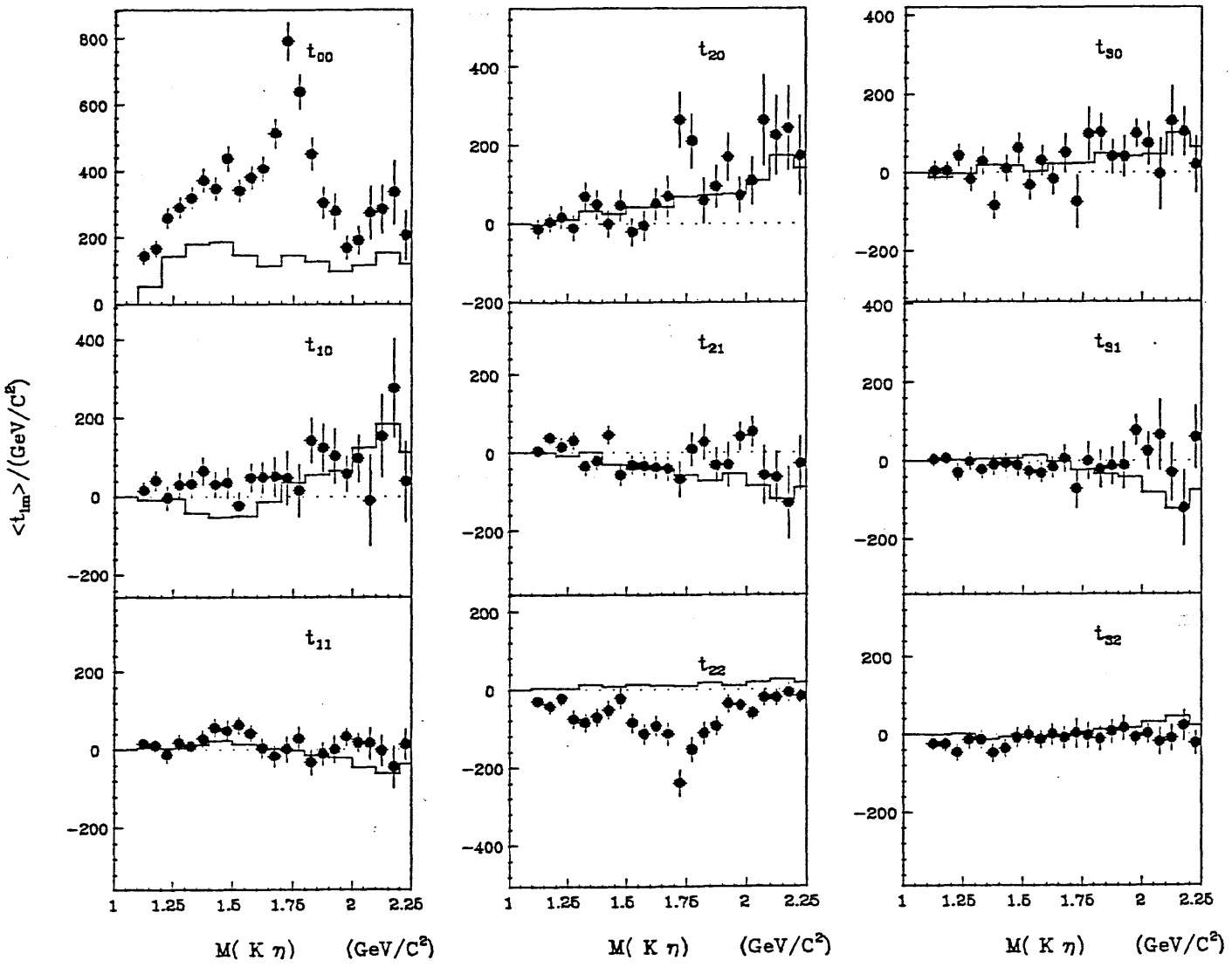

Fig. 50 The $K^-\eta$ mass dependence of the acceptance corrected moments in the $|t'_{p-p}|$ interval between $0.08(\mathrm{GeV/c})^2$ and $1.00(\mathrm{GeV/c})^2$. The non η background is shown by the histogram.

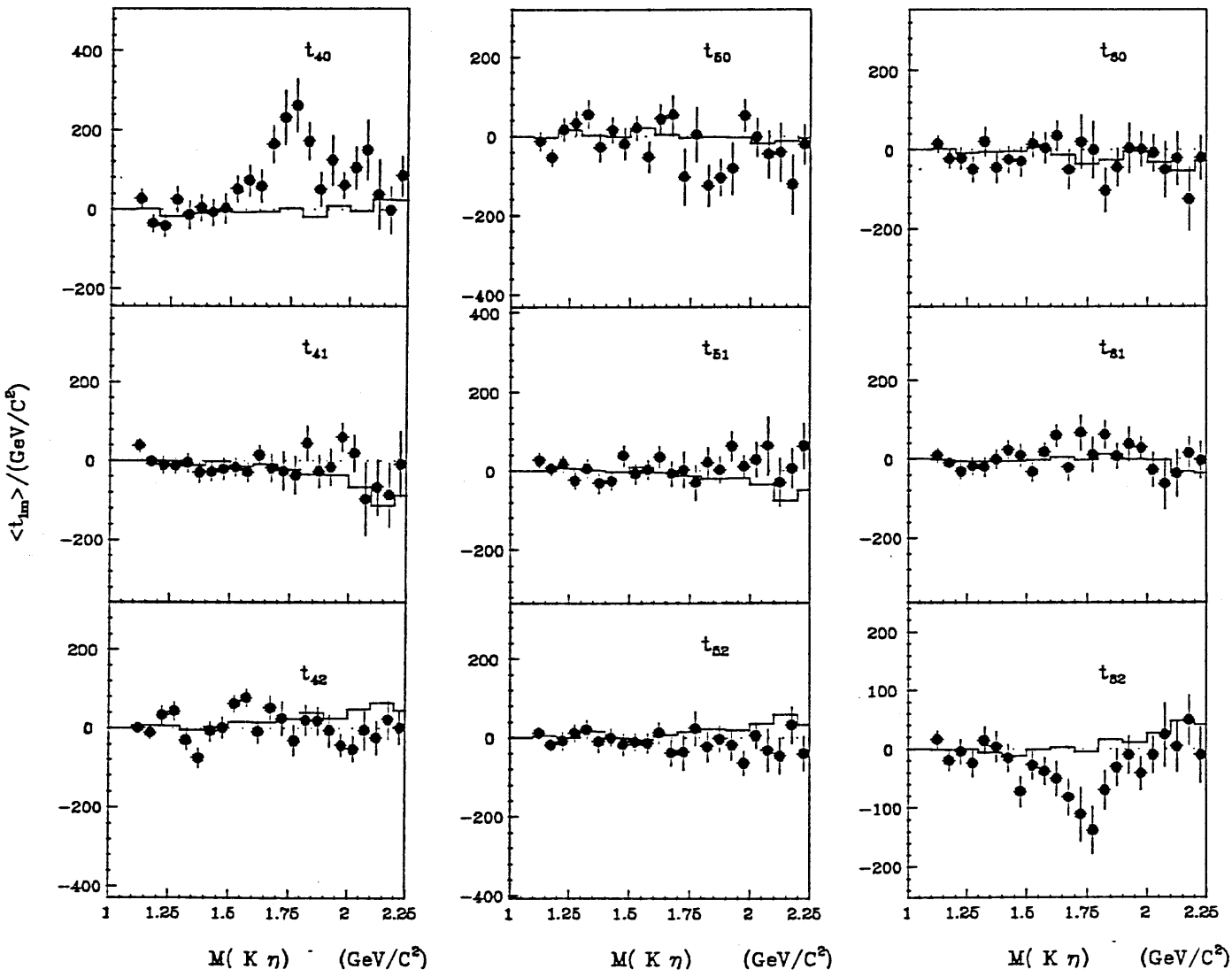

Fig. 50 **continued**

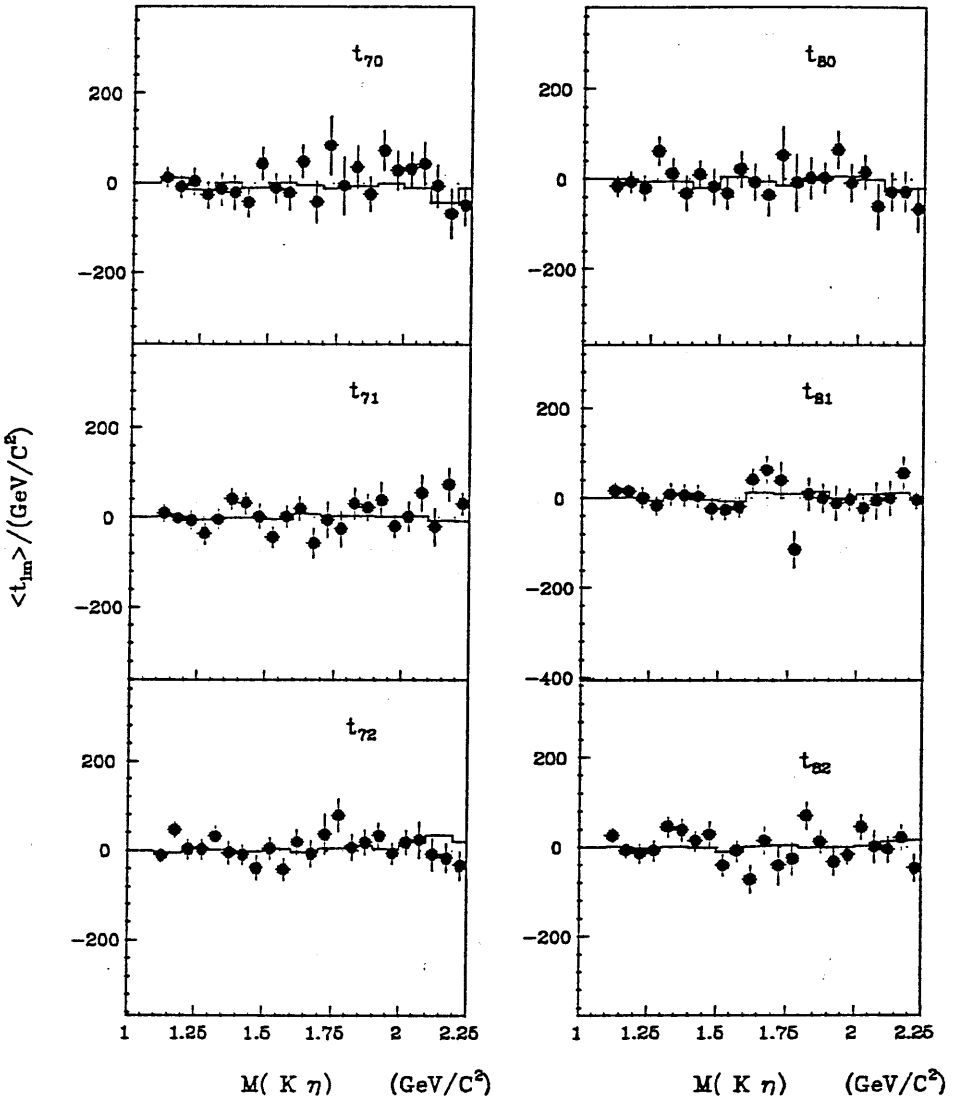

Fig. 50 **continued**

Since both natural and un-natural parity amplitudes are existing in the mass region $\sim 1.75\text{GeV/c}^2$, it is necessary to decompose these moments into production amplitudes for more quantitative discussion about the structure around $\sim 1.75\text{GeV/c}^2$.

6.7 Moments as a function of $|t'_{p-p}|$

To study the production mechanism in the $\sim 1.75\text{GeV/c}^2$ region, the momentum transfer $|t'_{p-p}|$ dependence of the moments is obtained in the $K^-\eta$ mass between 1.60GeV/c^2 and 1.95GeV/c^2. These distributions are shown in Fig.52. In these figures, the non η background is also shown by the histogram. Again, same moments of $l \leq 6$ and $m \leq 2$ are dominant.

Especially for $m = 2$ moment of t_{22} and t_{62}, the turnover effects are observed in the small $|t'_{p-p}|$ region. This is the indication of the natural parity exchange for this resonance.

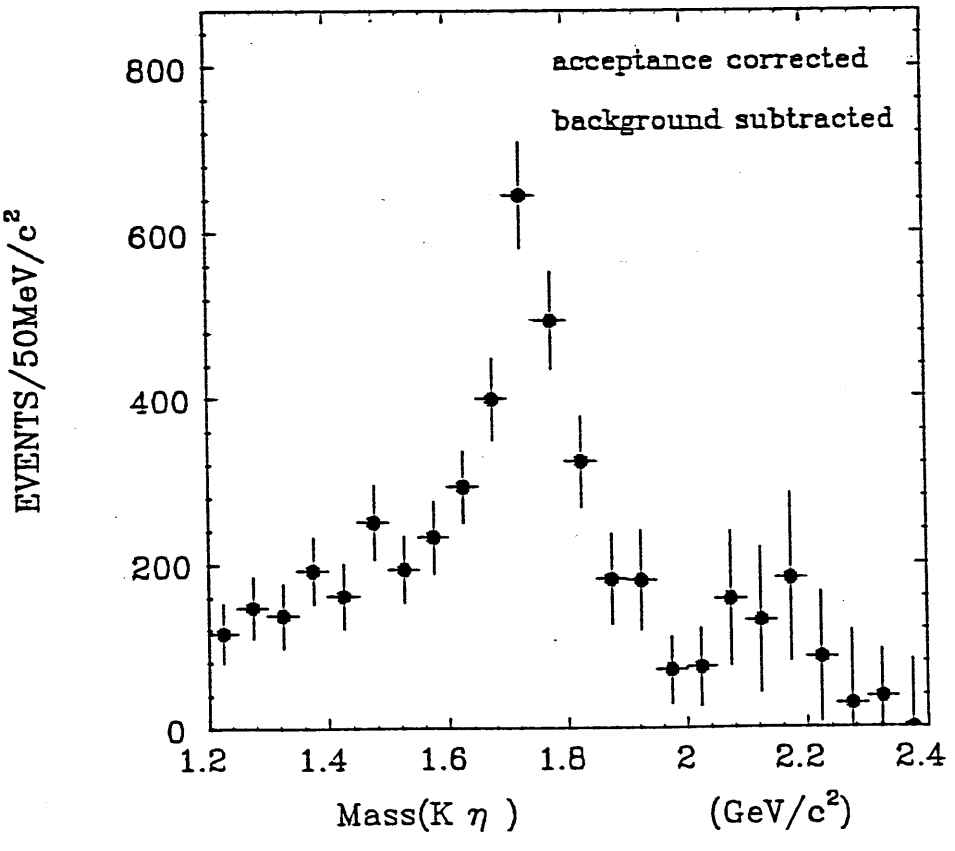

Fig. 51 The acceptance corrected and background subtracted $K\eta$ mass distribution.(t_{00} moment) in the $|t'_{p-p}|$ interval between $0.08(\text{GeV/c})^2$ and $1.00(\text{GeV/c})^2$.

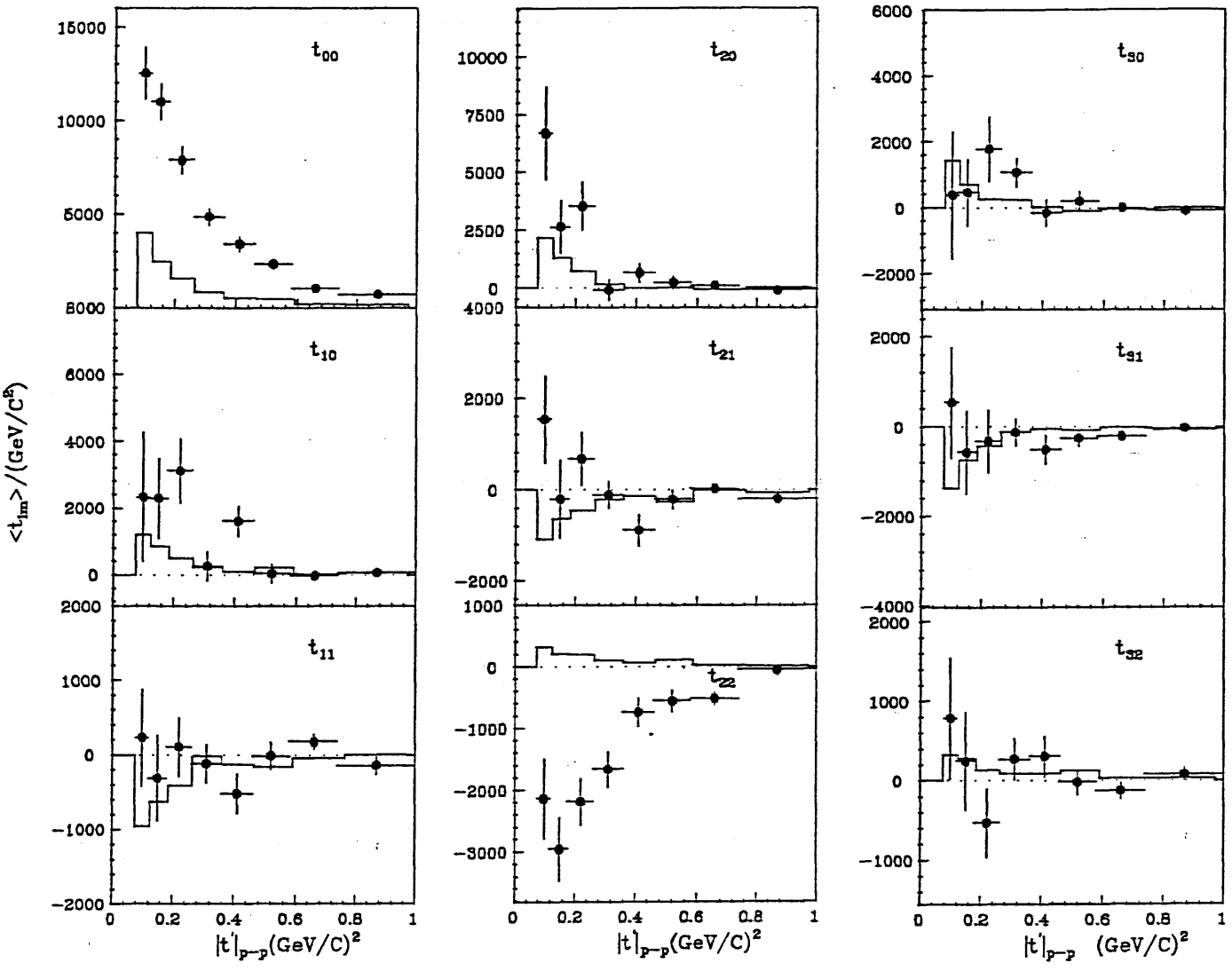

Fig. 52 The momentum transfer $|t'_{p-p}|$ dependence of the moments in the $K^-\eta$ mass region between 1.60GeV/c^2 and 1.95GeV/c^2 . The histogram shows the non η background .

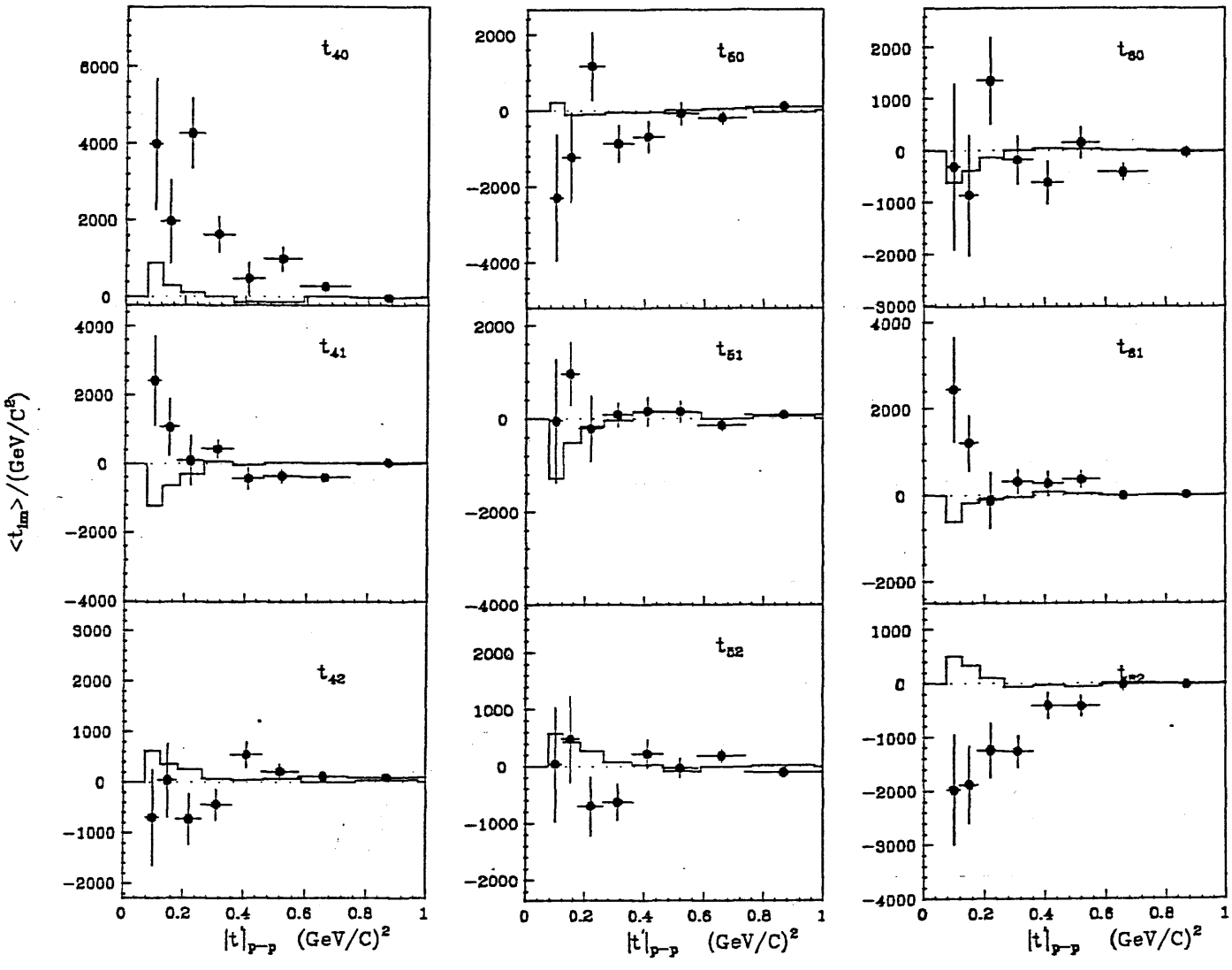

Fig. 52 continued

7. The Amplitude Decomposition

7.1 The basic formula

In order to extract the $K^-p \to (K^-\eta)p$ amplitudes from the observed moments, it is convenient to use combination of helicity amplitude with definite exchange naturality. In terms of helicity amplitudes H^L_λ, the production amplitudes $L_{\lambda\eta}$ of the $K^-\eta$ system with spin L and t-channel helicity λ via natural(**NPE**) $\eta = +$ or unnatural(**UPE**) $\eta = -$ parity excange are expressed by the form:

$$L_{\lambda\eta} = c_\lambda(H^L_\lambda - \eta(-1)^\lambda H^L_{-\lambda}) \tag{7.1}$$

where c_λ is $\frac{1}{2}$ for $\lambda = 0$ and $\frac{1}{\sqrt{2}}$ for $\lambda \neq 0$.

The observed moments can be expressed as sums of billinear products of these production amplitudes. The explicit relations between moments and amplitudes are given by [33]:

$$t_{lm} = \sum_{LL'\lambda\lambda\eta} \left(\frac{(2L+1)(2L'+1)}{2l+1}\right)^{\frac{1}{2}} < LL'00|l0 >(-1)^{\lambda'} < LL'\lambda\lambda'|lm > \cdot \frac{1}{4c_\lambda c_{\lambda'}} Re(L_{\lambda\eta} L^{*'}_{\lambda'\eta}). \tag{7.2}$$

where $<\ |\ >$ are Clebsh-Gordan coefficients. In this expression, the summation of nucleon helicity is implicit and the spin coherence at nucleon vertex is assumed.

$$\begin{aligned} Re(L_{\lambda\eta} L^{*'}_{\lambda'\eta}) &= Re(L^{\lambda\eta}_{++} L^{*'\lambda'\eta}_{++}) + Re(L^{\lambda\eta}_{+-} L^{*'\lambda'\eta}_{+-}) \\ &= Re(L^{\lambda\eta}_{--} L^{*'\lambda'\eta}_{--}) + Re(L^{\lambda\eta}_{-+} L^{*'\lambda'\eta}_{-+}) \end{aligned} \tag{7.3}$$

The relations between these amplitudes and moments relevant in this analysis are listed in the following table (table-10).

Table-10: The relations between the moments and the production amplitudes

$$
\begin{aligned}
t_{00} =& S_0^2 + P_0^2 + P_-^2 + P_+^2 + D_0^2 + D_-^2 + D_+^2 + F_0^2 + F_-^2 + F_+^2 \\
t_{10} =& 2.S_0P_0 + 1.789P_0D_0 + 1.549(P_-D_- + P_+D_+) + 1.656(D_-F_- + D_+F_+) + 1.757D_0F_0 \\
t_{11} =& 1.414S_0P_- + 1.095P_0D_- - 0.632P_-D_0 + 1.014D_0F_- - 0.717D_-F_0 \\
t_{20} =& 2.S_0D_0 + 0.894P_0^2 + 1.757P_0F_0 - 0.447(P_-^2 + P_+^2) + 1.434(P_-F_- + P_+F_+) \\
& + 0.639D_0^2 + 0.319(D_-^2 + D_+^2) + 0.596F_0^2 + 0.447(F_-^2 + F_+^2) \\
t_{21} =& 1.414S_0D_- + 1.095P_0P_- + 1.171P_0F_- - 0.717P_-F_0 + 0.452D_0D_- + 0.298F_0F_- \\
t_{22} =& 0.548(P_-^2 - P_+^2) - 0.293(P_-F_- - P_+F_+) + 0.391(D_-^2 - D_+^2) + 0.365(F_-^2 - F_+^2) \\
t_{30} =& 2.S_0F_0 + 1.757P_0D_0 - 1.014(P_-D_- + P_+D_+) + 1.193D_0F_0 + 0.422(D_-F_- + D_+F_+) \\
t_{31} =& 1.414S_0F_- + 1.171P_0D_- + 1.014P_-D_0 + 0.632D_0F_- + 0.298D_-F_0 \\
t_{32} =& 0.926(P_-D_- - P_+D_+) + 0.577(D_-F_- - D_+F_+) \\
t_{40} =& 1.746P_0F_0 + 0.857D_0^2 + 0.545F_0^2 + 0.091(F_-^2 + F_+^2) - 1.069(P_-F_- - P_+F_+) \\
& - 0.571(D_-^2 + D_+^2) \\
t_{41} =& 1.195P_0F_- + 0.976P_-F_0 + 1.107D_0D_- + 0.498F_0F_- \\
t_{42} =& 0.845(P_-F_- - P_+F_+) + 0.452(D_-^2 - D_+^2) + 0.287(F_-^2 - F_+^2) \\
t_{50} =& 1.699D_0F_0 - 1.201(D_-F_- + D_+F_+) \\
t_{51} =& 1.140D_0F_- + 1.074D_-F_0 \\
t_{52} =& 0.870(D_-F_- - D_+F_+) \\
t_{60} =& 0.840F_0^2 - 0.630(F_-^2 + F_+^2) \\
t_{61} =& 1.112F_0F_- \\
t_{62} =& 0.431(F_-^2 - F_+^2)
\end{aligned}
$$

Here L_0 stand for helicity zero unnatural parity amplitude $L_0 = L_{0-}$, and L_+, L_- are the helicity one natural parity L_{1+} and un-natural parity amplitudes L_{1-} , respectively. In this table, we use the abbreviated notations:

$$LL' \equiv Re(L_{\lambda\eta}L^{*'}_{\lambda'\eta}) = |L_{\lambda\eta}||L^{*'}_{\lambda'\eta}|\cos(\theta_{LL'}). \tag{7.4}$$

Fitting the moments by these amplitudes, absolute value of each amplitude and the relative phases can be determined.

7.2 The Fitting procedure

The acceptance corrected and background subtracted moments are used to detemine the production amplitudes. Since moments with $l \leq 6$ and $m \leq 2$ are enough to reproduce the data distribution, the amplitude $\lambda > 1$ is neglected. Each moments upto $l = 6, m = 2$ are used to determine the amplitudes $S_0, P_0, P_\pm, D_0, D_\pm F_0$ and $F_\pm$. We choose F_0 and F_+ waves as a reference in **UPE** and **NPE** amplitude. These reference phases can be chosen independently, since there are no interference term between **UPE** and **NPE** amplitudes (see table-10).

The determination of fitting parameters are perfomed independently in each mass bin. The χ^2 function to be minimized in the fit is defined by the form:

$$\chi^2 = \sum_{\mu\nu} (t_\mu - \overline{t_\mu})(E_{\mu\nu})^{-1}(t_\nu - \overline{t_\nu}) \tag{7.5}$$

where t_μ are measured moments after subtracting the non-η background and $\overline{t_\mu}$ are predicted moments in the terms of amplitudes. $E_{\mu\nu}$ are error matrix for t_μ. The effect of the background subtruction are included in this error matrix by adding both error matrices in η resonance region $E^{\eta}_{\mu\nu}$ and background $E^{back.}_{\mu\nu}$.

$$E_{\mu\nu} = E^{\eta}_{\mu\nu} + E^{\text{back.}}_{\mu\nu} \tag{7.6}$$

In the practical fit of the moments, real and imaginary parts of the amplitudes S_0, P_0, $P_\pm$, $D_0, D_\pm$, F_0 and $F_\pm$ are used as free parameters instead of the absolute value of amplitudes and relative phases. The former parameterization is found to be more suitable than the latter in this analysis, since boundary conditions of the latter parameterization are critical to fit small statistics data.

7.3 The Results of the Amplitudes as a function of $K^-\eta$ mass

The amplitudes as a function of $K^-\eta$ mass are obtained in the $|t'_{p-p}|$ region between 0.08 and 1.00(GeV/c)^2. The summed amplitudes

$$|L|^2_{\rm tot} = |L_+|^2 + |L_-|^2 + |L_0|^2 \tag{7.7}$$

are shown in fig.53. Only F wave has the significant peak structure. And other waves are consistent with flat distribution within error bars. The F wave is stable since it is the highest wave in the amplitude decomposition. For another underling waves S, P, D, there are ambiguities in the region above 1.5GeV/c^2. But those difference are within error bars shown in fig.53. The detailed discussion on the ambiguities of the underling waves is given in Appendix 1.

7.4 Properties of F wave

The resonance fit with Breit-Wigner form

To extract the resonance parameters from F wave, a fit is performed with relativistic Breit-Wigner with no background term. The Breit- Wigner used in this fit is expressed in the form :

$$\begin{aligned}
\frac{d\sigma}{dM} &= c\frac{M\Gamma^i(M)}{(M_0^2 - M^2)^2 + M_0^2\Gamma^2_{\rm tot}(M)} \\
\Gamma_{\rm tot}(M) &= \sum_i \Gamma^i(M) \\
\Gamma^i(M) &= \Gamma^i_0 \left(\frac{q}{q^i_0}\right)^{2l+1} \left(\frac{M_0}{M}\right) \left(\frac{D_l(q_0 r)}{D_l(qr)}\right) \\
\Gamma^0_{\rm tot} &= \sum_i \Gamma^i_0
\end{aligned} \tag{7.8}$$

where l is a resonance spin, c is a normalization constant, M is the effective mass of the $K^-\eta$ system. M_0 and $\Gamma^0_{\rm tot}$ are the resonance mass and the total width, respectively. Γ^i_0 is the partial width to the i'th decay mode at $M = M_0$. q and q_0 are c.m. momenta of decayed particle at M and M_0 , respectively. Finally, $D_l(qr)$ is a Blatt and Weisskopf barrier factor[34] and r in this factor is interaction radius of the resonance, which is fixed at 3(GeV/c)$^{-1}$ in the fit. The explicite form of the barrier factor $D_l(X)$ for $l \leq 4$ is given by:

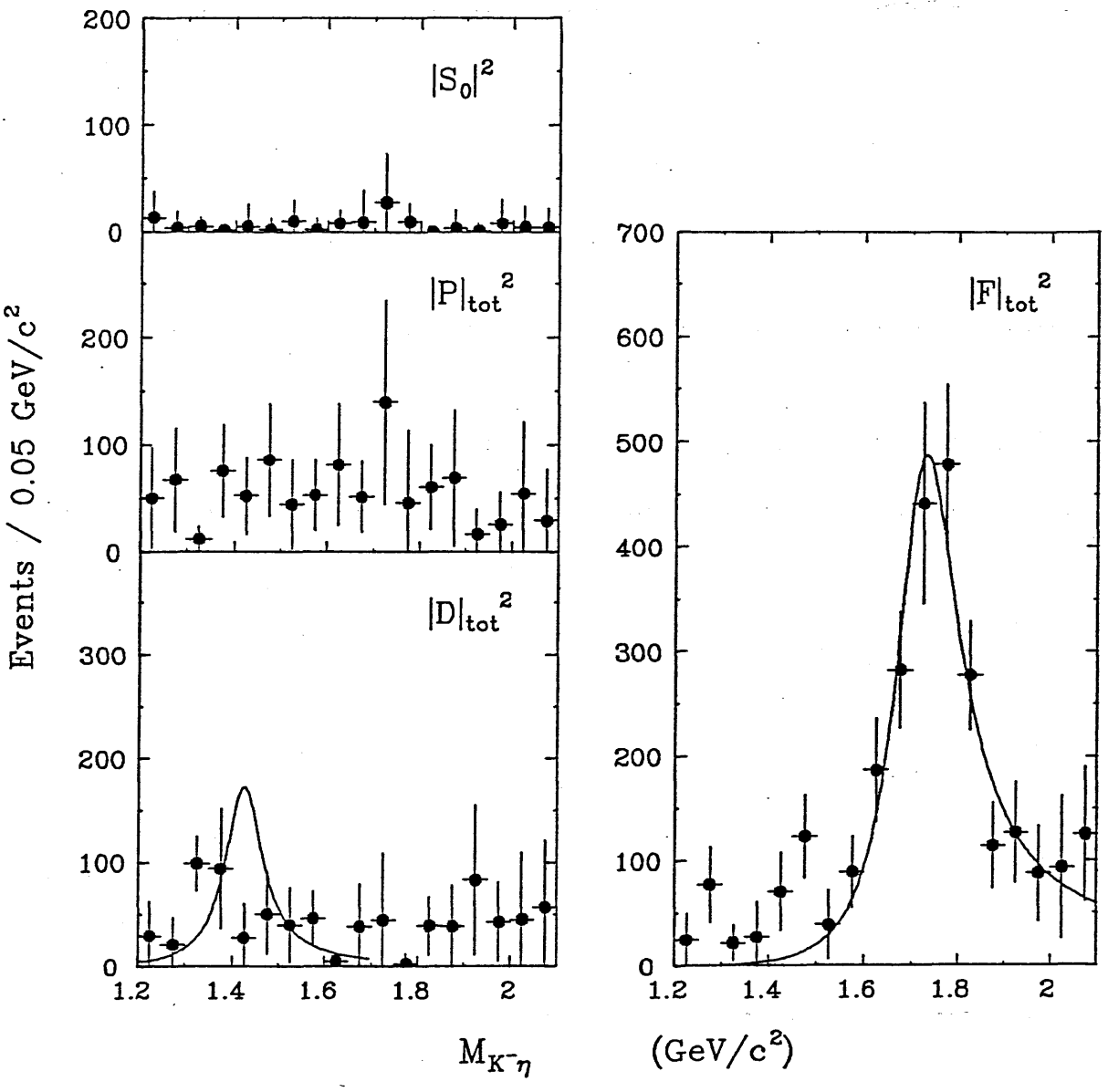

Fig. 53 The $K^-\eta$ mass dependence of the summed amplitudes. The curve superposed on $|F|^2_{tot}$ shows the results of the Breit-Wigner fit described in the text. While the curve on the $|D|^2_{tot}$ intensity shows the 95 % confidence level upper limit for $K_2^*(1430)$ production.

$$
\begin{aligned}
D_0(X) &= 1 \\
D_1(X) &= 1 + X^2 \\
D_2(X) &= 9 + 3 \cdot X^2 + X^4 \\
D_3(X) &= 225 + 45 \cdot X^2 + 6 \cdot X^4 + X^6 \\
D_4(X) &= 11025 + 1575 \cdot X^2 + 135 \cdot X^4 + 10 \cdot X^6 + X^8
\end{aligned}
\tag{7.9}
$$

The fitting results of $|F|^2_{\rm tot}$ are supperposed in fig.53. The obtained mass and width are summalized in the table-11.

Table-11: The resonance parameters of $|F|^2_{\rm tot}$

	$\|F\|^2_{tot}$
Mass	$M = 1749 \pm 10 \pm 12$ MeV/c^2
Width	$\Gamma = 193\ ^{+51}_{-37}$ MeV/c^2
χ^2 /NDF	7.0 /9

In this table, the quoted errors are statistical and systematic errors, respectively. One of the main contribution to the systematic error on mass is estimated by shifting the mass binning by half (± 5 MeV/c^2). Other source of systematics by the the fit conditions are checked by changing the value of interaction radius r between $2 - 4$(GeV/c)$^{-1}$ or including other decay modes $K\pi, K^*\pi$ and $K\rho$ in the decay barrier factor. These effects are found negligible. Another main systematics on mass comes from the difficulty in eliminating the N^* reflection. This effect is estimated by using different N^* cut values and is approximately as large as the statistical $\sim \pm 10$MeV/c^2. The systematic error on mass quoted in the table is obtained by adding these two errors in quadrature.

Given the results of the moment analysis and the amplitude decomposition, the peak around 1.75GeV/c^2 is therefore most naturally interpreted as the $J^p = 3^-$ $K_3{}^*(1780)$. The mass value itself is systematically lower than the value cited in the PDG table [8], but the difference is within one standard deviation.

The total intensity of the F wave ($K_3{}^*(1780)$) is consistent with the peak intensity observed in the $K\eta$ mass spectrum(Fig.51).

7.5 The decay branching ratio of $K_3^*(1780)$

Fig.54 shows the detailed decomposition of the F wave. Both $|F_0|^2$ and $|F_+|^2$ show strong peak and $|F_-|^2$ contribution is negligible. The intensity of F_0 wave is about 60% of F_+ wave. The observation of both **UPE** amplitude F_0 and **NPE** amplitude F_+ are consistent with the results of $K_3^*(1780)$ production in the same non charge exchange reaction of $K\pi$ channel [7]. The observation of the substantial intensity of the **UPE** amplitude in the non charge exchange reaction is explained by the generalized C-parity conservation. This conservation implies that the pomeron, which contribute to the **NPE** amplitude, couples to the odd spin states only through a small non-singlet component. The dominant **NPE** amplitude, therefore, is reduced and the **UPE** waves contribute significantly. [7].

The curve superposed is the fit with pure Breit-Wigner form to obtain the production cross section. The fit results are:

$$\begin{aligned} M_{F_+} &= 1752 \pm 11 \text{ MeV/c}^2 \\ \Gamma_{F_+} &= 192^{+50}_{-36} \text{ MeV/c}^2 \\ (\chi^2/NDF &= 7.0/9) \end{aligned} \tag{7.10}$$

$$\begin{aligned} M_{F_0} &= 1733 \pm 15 \text{ MeV/c}^2 \\ \Gamma_{F_0} &= 147^{+110}_{-51} \text{ MeV/c}^2 \\ (\chi^2/NDF &= 6.7/9) \end{aligned} \tag{7.11}$$

Integrating the Breit-Wigner formulae for the $|F_0|^2$ and $|F_+|^2$ over the approximayely two Γ mass region between $1.4 - 2.2\text{GeV/c}^2$, and correcting the $\eta \to \pi^+\pi^-\pi^\circ$ decay braching ratio (=0.237), the visible cross section in the measured $|t'|$ region (0.08 – 1.00 $(\text{GeV/c})^2$) is obtained to be:

$$\sigma(K_3^{*-}(1780)) \cdot BR(K_3^{*-}(1780) \to K\eta) = 2.30 \pm 0.23 \pm 0.08 \mu b \tag{7.12}$$

The quoted errors are statistics and systematics, respectively. The systematic error is estimated from the difference when mass binnings are shifted by half. The effect on

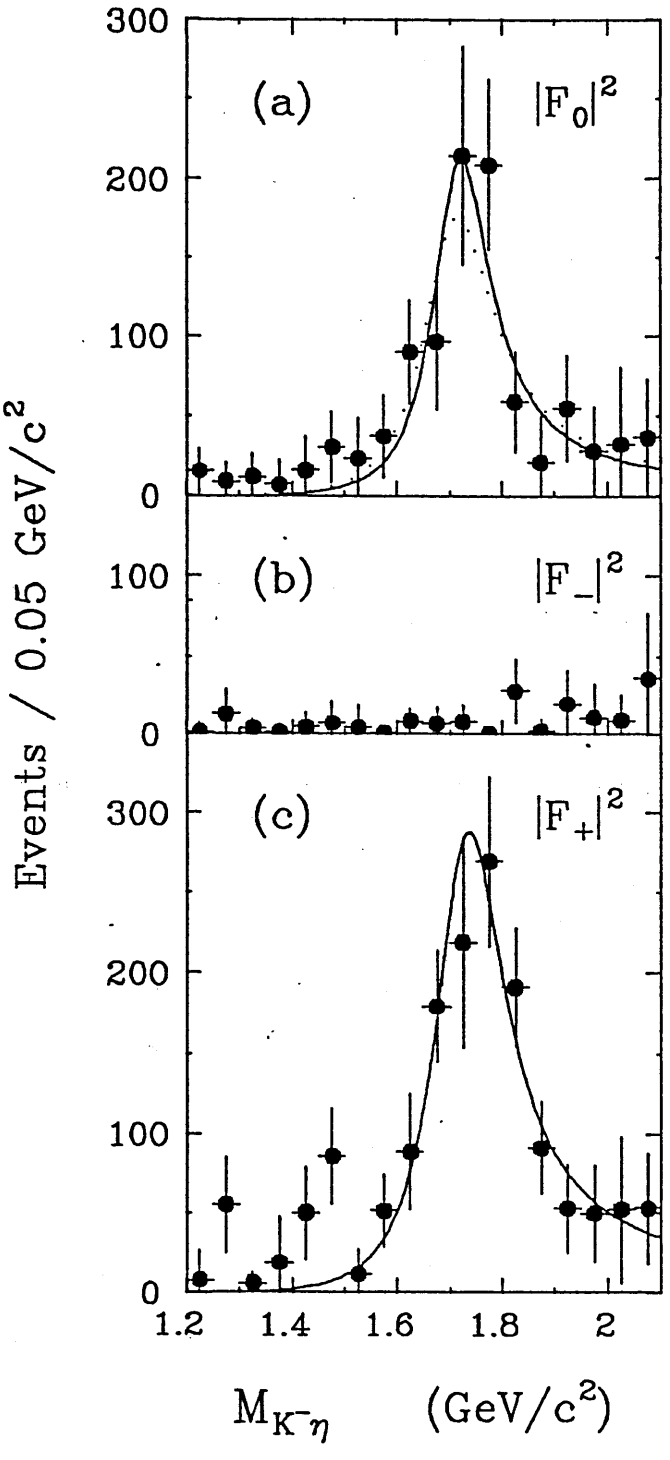

Fig. 54 Detail of the F-wave structure; Mass spectrum of (a) $|F_0|^2$, (b) $|F_-|^2$, and (c) $|F_+|^2$. The curve supperposed is the results of the fit with Breit-Wigner form used for the determination of the cross section for the $K_3^*(1780)$ as described in the text.

the integral value by the change of fitting conditions are small. For example, a fit of $|F_0|^2$ wave by fixing the mass or width to the value of $|F|_{\rm tot}$ gives -1.4 % or +0.5 % change of the integral, respectively.

The momentum transfer $t'_{p\to p}$ dependences of the significant amplitudes $|F_0|^2$ and $|F_+|^2$ in the $K_3^*(1780)$ region (1.60-1.95GeV/c^2) are shown in fig. 55a and fig. 55b, respectively. The t' dependence of F_+ wave is consistent with the expected form of natural parity exchange, and F_0 is consistent with un-natural parity exchange. The fit by the forms

$$A_+|t'|e^{-B_+|t'|}$$

for $|F_+|^2$ and

$$A_0\frac{-t}{(m_\pi^2-t)^2}e^{-B_0|t'|}$$

for $|F_0|^2$ in the $|t'|$ region of $0.08 \le |t'_{p\to p}| < 1.00(\mathrm{GeV/c})^2$, yielding the shape parameters $B_0 = 5.9 \pm 1.4(\mathrm{GeV/c})^{-2}$ (χ^2/NDF= 4.3/6) and $B_+ = 9.2 \pm 0.8(\mathrm{GeV/c})^{-2}$ (χ^2/NDF = 4.4/6). Correcting the t' dependence by the formulae obtained above, the cross section times branching ratio in the full t' region is found to be $\sigma(K_3^{*-}(1780))\cdot BR(K_3^{*-}(1780) \to K^-\eta) = 3.90 \pm 0.55\ \mu b$ (systematic error included). The error mainly comes from the extrapolation of the t' distribution to $t' = 0$.

The products of the production $K_3^*(1780)$ cross section times branching fraction to $K\pi$ system in the non-charge exchange reaction is given by the CERN-Geneva group [7]. They parametrized in the formula :

$$\sigma(K_3^{*-}(1780))\cdot BR(K_3^{*-}(1780)\to K\pi) = A\cdot \mathrm{p}^{-n}\quad(\mu b)\quad(\mathrm{p\ in\ GeV/c})$$
$$A = 76 \pm 25,\quad n = 0.95 \pm 0.1 \qquad (7.13)$$

where p is a incident beam momentum.

Taking cross section $\sigma(K_3^{*-}(1780))\cdot BR(K_3^{*-}(1780)\to K\pi) = 7.8\ \pm 2.6\ \mu b$ at 11 GeV/c from this formula , the relative width of $K\eta$ to $K\pi$ is

$$R_3 = \frac{\Gamma(K_3^*(1780)\to K\eta)}{\Gamma(K_3^*(1780)\to K\pi)} = 0.50\ \pm\ 0.18.$$

Taking the most precise measurement value for $BR(K^*(1780) \to K\pi) = 18.7\ \pm 1.2\%$

[4], we obtain $BR(K_3^*(1780) \to K\eta) = 9.4 \pm 3.4\%$‖ .

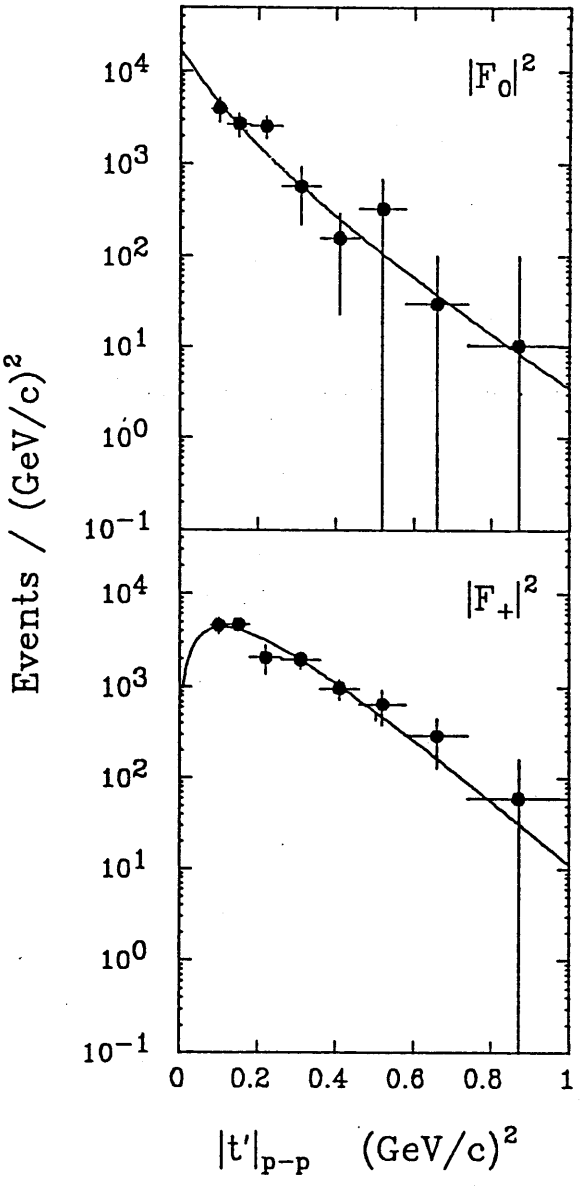

Fig. 55 The $|t'_{p-p}|$ dependence of (a) $|F_0|^2$, and (b) $|F_+|^2$ in the $K_3^*(1780)$region between 1.60 and 1.95 GeV/c^2 . The curves show the results of the fits described in the text.

‖ A future direct comparison with the $K_s^0\pi^-$ decay in this experiment will greatly improve the precision of this result by removing most of the systematic error.

7.6 The upper limit of $K_2^*(1430)$

The D-wave amplitude (fig. 56) show no positive evidence for the 2^+ $K_2^*(1430)$, even though the $K_2^*(1430)$ production cross section is known to be large [7].

Taking the production cross section for the $K_2^*(1430)$ into $K\pi$ from Ref. [7],

$$\sigma(K_2^{*-}(1430)) \cdot BR(K_2^{*-}(1430) \to K\pi) = A \cdot \mathrm{p}^{-n} \quad (\mu b) \quad (\mathrm{p \text{ in GeV/c}}) \\ A = 302 \pm 96, \quad n = 0.77 \pm 0.1 \tag{7.14}$$

the upper limit of the relative width of $K\eta$ to $K\pi$ is estimated from the $|D|^2_{tot}$ distribution is

$$R_2 = \frac{\Gamma(K_2^*(1430) \to K\eta)}{\Gamma(K_2^*(1430) \to K\pi)} < 0.92\%$$

at the 95% confidence level. The $K_2^*(1430)$ signal intensity corresponding to this upper limit is shown by the solid curve on the D-wave amplitude in fig. 56. The excessed events around $M(K\eta) \sim 1.35\mathrm{GeV/c^2}$ is also included in the K_2^* signal to determine the upper limit conservatively. Another fit using the amplitudes of $S_0, P_{0,\pm}$ and $D_{0,\pm}$ by excluding the F wave is also tried below 1.5 GeV/c. This fit gives the similar upper limit of $< 0.80\%$. While the upper limit estimated from the mass distribution (t_{00} moments) assuming the smooth background is $< 0.60\%$. We have accepted the most large one as a conservative estimation for the upper limit of K_2^*.

Using the value $BR(K_2^*(1430) \to K\pi) = 0.485$ [4], we find an upper limit for $BR(K_2^*(1430) \to K\eta)$ of 0.45% at the 95% confidence level. This is substantially smaller than the value 5.2 $\pm$ 2.9 % , which is indirectly obtained by the Particle Data Group from a multi-channel fit [8]. The dotted curve in fig. 56 is the expected signal intensity if the branching fraction $BR(K_2^*(1430) \to K\eta)$ is just **half** of the above Particle Data Group value. The same curve is also shown in the acceptance corrected and background subtracted $K\eta$ mass distribution (t_{00} moment) in fig.57. These figures indicate that $BR(K_2^*(1430) \to K\eta)$ should be much smaller than the PDG value.

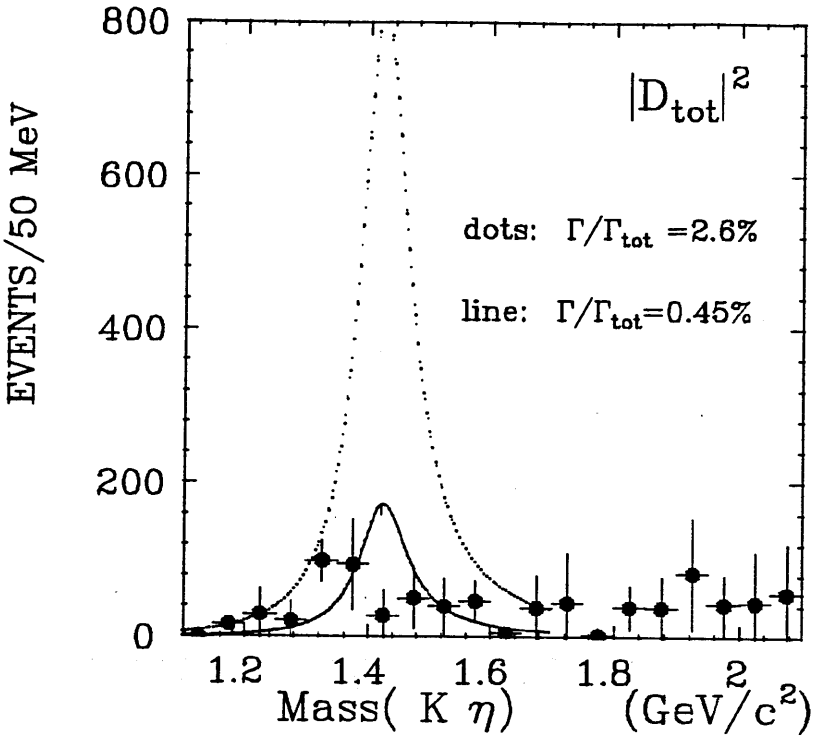

Fig. 56 The $K^-\eta$ mass dependence of the D wave. The solid curve shows the 95 % confidence level upper limit for $K_2^*(1430)$ production and the dotted curve the expected signal intensity if the branching fraction $BR(K_2^*(1430) \rightarrow K\eta)$ is 2.6%.

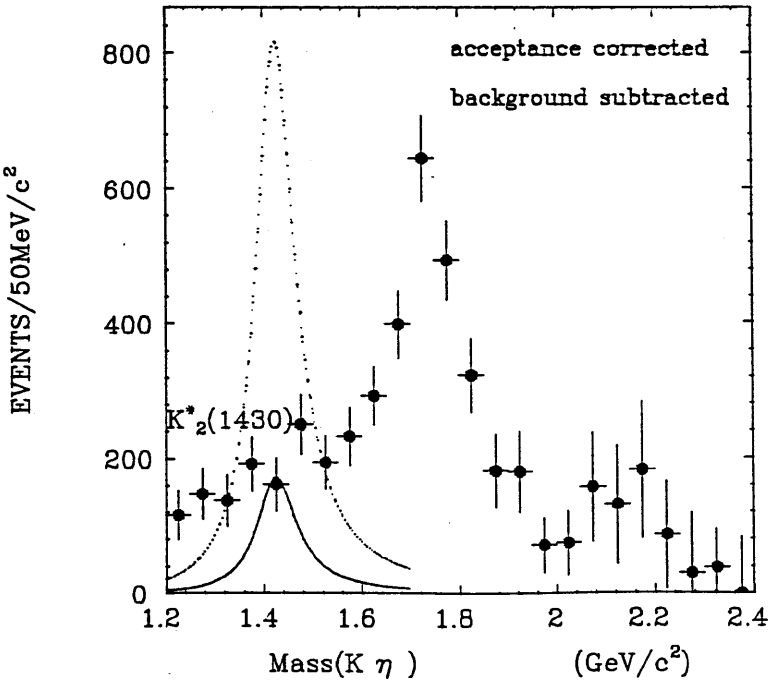

Fig. 57 The acceptance corrected and background subtracted $K\eta$ mass distribution.(t_{00} moments) The solid curve shows the 95 % confidence level upper limit for $K_2^*(1430)$ production and the dotted curve the expected signal intensity if the branching fraction $BR(K_2^*(1430) \rightarrow K\eta)$= 2.6%.

8. The Discussion and Conclusion

8.1 Discussion

As is shown in the preceding chapter, $K_3^*(1780)$ is observed in the $K\eta$ mass spectrum as a promimant peak (Fig.43) and its nature of spin 3 is confirmed in the t_{lm} moments and by the clear peak structure of the F wave. The intensity of the F wave is consistent with the peak in the $K\eta$ mass spectrum (Fig.50,Fig.57). The measured relative width of $K\eta$ to $K\pi$ is

$$R_3 = \frac{\Gamma(K_3^*(1780) \to K\eta)}{\Gamma(K_3^*(1780) \to K\pi)} = 0.50 \pm 0.18.$$

On the other hand, no positive evidence of the $K_2^*(1430)$ is observed in either the $K^-\eta$ mass spectrum (Fig. 43) and the D-wave amplitude (Fig. 53). The upper limit of the relative width of $K\eta$ to $K\pi$ is

$$R_2 = \frac{\Gamma(K_2^*(1430) \to K\eta)}{\Gamma(K_2^*(1430) \to K\pi)} < 0.92\%$$

at the 95% confidence level.

This dramatic difference between the $K\eta$ coupling to the $K_2^*(1430)$ and the $K_3^*(1780)$ is consistent with the prediction of SU(3) and nonet-symmetry of pseudo-scalar which are described in the chapter 2. In this symmetry, there are two different $K^*\overline{K}\eta$ three meson couplings according to the charge conjugation of parent and daughter meson states. Two pseudo-scalar decays of $K_2^*(1430)$ is D-type coupling, while those of $K_3^*(1780)$ is F-type's. The large difference of the observed decay rates is explained from this different coupling types and with the special value of η and η' mixing angle. A straight-forward calculation explained in the chapter 2 gives the predictions of the relative branching ratios of $K_2^*(1430)$ and $K_3^*(1780)$:

$$\begin{aligned} R_2 = \frac{\Gamma(K_2^*(1430) \to K\eta)}{\Gamma(K_2^*(1430) \to K\pi)} &= \frac{1}{9}(\cos\theta_p + 2\sqrt{2}\sin\theta_p)^2 \left(\frac{q_{K\eta}}{q_{K\pi}}\right)^5 \\ &= \frac{1}{9}(\cos\theta_p + 2\sqrt{2}\sin\theta_p)^2 \cdot 0.298 \end{aligned} \tag{8.1}$$

and

$$R_3 = \frac{\Gamma(K_3^*(1780) \to K\eta)}{\Gamma(K_3^*(1780) \to K\pi)} = (cos\theta_p)^2 \left(\frac{q_{K\eta}}{q_{K\pi}}\right)^7 = (cos\theta_p)^2 \cdot 0.424 \quad . \tag{8.2}$$

Where $q_{K\eta}$ and $q_{K\pi}$ are the c.m. momenta of the final $K\eta$ and $K\pi$ states, respectively, and θ_p is the SU(3) singlet-octet mixing angle of η and η' in the 0^- nonet. The decay branching ratios predicted from these formulae are plotted in fig.58 as a function of θ_p.

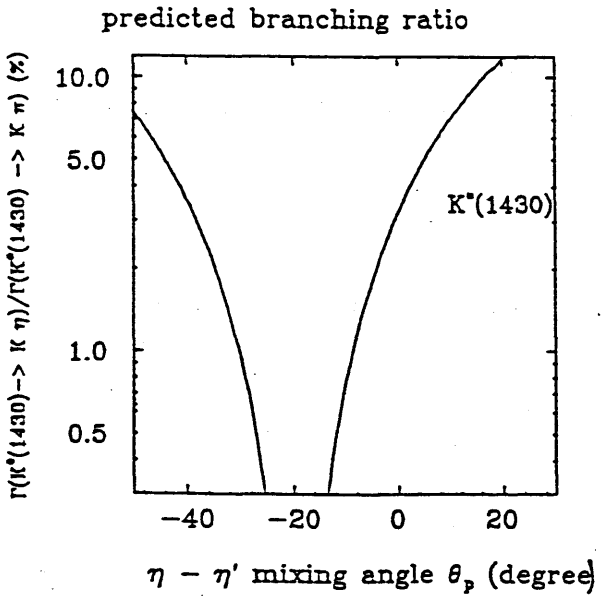

Fig. 58-a The SU(3) prediction of $K_2^*(1430)$ decay branching ratio: $R_2 = \frac{\Gamma(K_2^*(1430)\to K\eta)}{\Gamma(K_2^*(1430)\to K\pi)}$

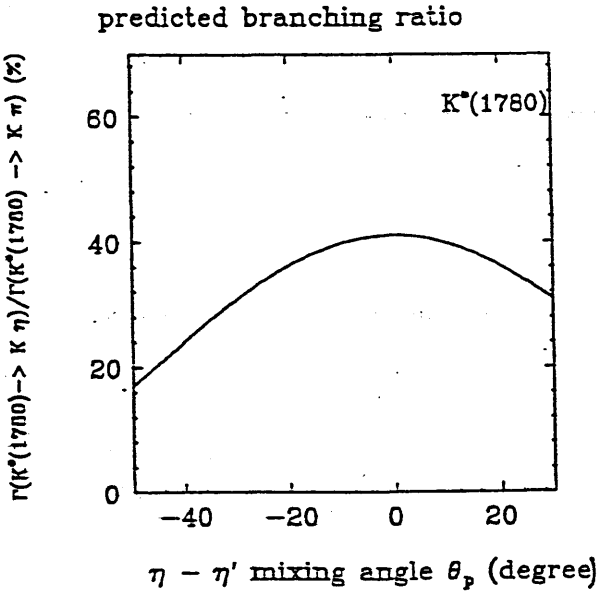

Fig. 58-b The SU(3) prediction of $K_3^*(1780)$ decay branching ratio: $R_3 = \frac{\Gamma(K_3^*(1780)\to K\eta)}{\Gamma(K_3^*(1780)\to K\pi)}$

Since θ_p is known to be small negative value, R_2 is suppressed significantly over the explicit factor 9, due to the cancellation in the parenthesis. As can be seen from fig.58-a, R_2 almost vanishes around $\sim -20°$. On the other hand, the value of R_3 is relatively large and is rather insensitive to θ_p. For typical mixing angles, the branching ratios are as follows:

$\theta_p = \ 0.0° : R_2 = 3.3\%, R_3 = 42\%$;
$\theta_p = -10.0° : R_2 = 0.8\%, R_3 = 41\%$ (quadratic mass formula) ;
$\theta_p = -19.5° : R_2 = 0.0\%, R_3 = 38\%$;
$\theta_p = -23.0° : R_2 = 0.1\%, R_3 = 36\%$ (linear mass formula).

The value of R_3 measured in the experiment is consistent with all of the above predicted values. In contrast, the measured upper limit of R_2 excludes the non-mixing case ($\theta_p = 0.0°$) and is close to the value of quadratic mass formula. The prediction by the linear mass formula is consistent with this result. In this regard , it should be noted a recent review by Gilman and Kauffman [17] conclude that $\theta_p \simeq -20°$ is consistent with all of the relevant physical evidence. This evidence is strongly supported in the process $J/\Psi \rightarrow \gamma\eta(\eta')$ and the measurements of the $\gamma\gamma$ decay width of η, η', π° mesons. In the hadronic decay of the light meson, this evidence is not clear. Although it is difficult to distinguish between $\theta_p \simeq -10°$ and $\theta_p \simeq -20°$ from this 95% upper limit of R_2, no observation of the $K_2^*(1430)$ in the $K\eta$ system may indicate that $\theta_p \simeq -20°$ is also favour in the hadronic decay of the light meson.

The simple SU(3) and nonet-symmetry of the pseudo-scalar explain the $K\eta$ decay of both $K_2^*(1430)$ and $K_3^*(1780)$ resonances remarkably well. This SU(3) features apply generally to all the K^* states. $K\eta$ couples preferentially to odd spin K^*'s, and not to even spin K^*'s. Further exploration of the underlying K^* states in the $K\eta$ channel, and studies of the $K^* \rightarrow K\eta'$ decay may reinforce the argument. In the $K\eta'$ channel, the situation is reversed, so that even spin K^*'s couple to $K\eta'$ preferentially, and suppression of the $K_3^*(1780)$ is expected. The SU(3) predicts that :

$$\begin{aligned} R^{\eta'}_{\text{even}} &= \frac{\Gamma(K^*_{\text{J=even}} \rightarrow K\eta')}{\Gamma(K^*_{\text{J=even}} \rightarrow K\pi)} = \frac{1}{9}(\sin\theta_p - 2\sqrt{2}\cos\theta_p)^2 \left(\frac{q_{K\eta'}}{q_{K\pi}}\right)^{2\text{J}+1} \\ R^{\eta'}_{\text{odd}} &= \frac{\Gamma(K^*_{\text{J=odd}} \rightarrow K\eta')}{\Gamma(K^*_{\text{J=odd}} \rightarrow K\pi)} = (\sin\theta_p)^2 \left(\frac{q_{K\eta'}}{q_{K\pi}}\right)^{2\text{J}+1} \end{aligned} \tag{8.3}$$

8.2 Conclusion

In conclusion, we have performed a complete analysis of $K^-\eta$ system in the reaction $K^-p \rightarrow K^-\eta p(\eta \rightarrow \pi^+\pi^-\pi^\circ)$. A clear $K_3^*(1780)$ signal is observed in the $K^-\eta$ mass spectrum and its nature of spin 3 is comfirmed by the moment analysis and the amplitude decomposition. Both natural parity exchange and un-natural parity exchange amplitudes are seen for the $K_3^*(1780)$. After correcting the different dependence of the momentum transfer of these two amplitudes, the branching fraction $BR(K_3^*(1780) \rightarrow K\eta)$ is measured to be 9.4 $\pm$ 3.4 %. No positive evidence of the $K_2^*(1430)$ is observed. The

upper limit of the branching fraction $BR(K_2^*(1430) \rightarrow K\eta)$ obtained to be less than 0.45% at the 95% confidence level. This upper limit is significantly lower than the value cited by the Particle Data Group [8]. These results provide clear experimental evidence for the suppression of the $K_2^*(1430)$ coupling and the relatively large coupling of the $K_3^*(1780)$ to the $K\eta$ channel predicted by SU(3) with octet-singlet mixing of η-η'.

No exotic phenomina is seen in the mass distribution, moments and amplitudes of the $K\eta$ system.

9. Appendix-1

The method of Barret zeros

The important feature of the amplitude decomposition is the ambiguity of the solutions. It is well known that the set of equations in the Table-10 has multiple set of solutions. If upto $\tilde{L}$ waves are included to describe the data, there will be $2^{\tilde{L}}$ descrete sets of ambiguities for helicity zero amplitudes and $2^{\tilde{L}-1}-$ hold ambiguities for helicity 1 **NPE**. And if helicity 1 **UPE** amplitudes are significant, these amplitudes also have $2^{\tilde{L}-1}$ set of solutions. This is serious problems to discuss the underling waves. But a general treatment to study this ambiguity is possible with the methode of Barret zeros.[35] Here I describe this methode in the case that both helicity 0,1 **UPE** and helicity 1 **NPE** amplitudes are existing upto F wave.($\tilde{L}=3$).

The decay angular distribution $G(X,\Omega)$ of K^* in the reaction $K^-p \to K^*p$ can be expressed by the aboslute square of the amplitudes:

$$G(X,\Omega) = \frac{1}{4\pi}(|A_0(X,\Omega) + A_-(X,\Omega)|^2 + |A_+(X,\Omega)|^2) \tag{9.1}$$

where $A_0(X,\Omega), A_-(X,\Omega)$ are the sum of helicity zero and 1 **UPE** amplitude, respectively. And $A_+(X,\Omega)$ is the sum of helicity 1 **NPE** amplitude. Note that there are no interfererence terms between **UPE** and **NPE** amplitudes.

The situation of the multiple solutions in the amplitude decomposition can be understand by expressing **UPE** and **NPE** amplitude as a function of $\cos\theta$, explicitely. The **UPE** amplitude $A_0(X,\Omega)$ can be written in the form

$$\begin{aligned} A_0(X,\Omega) =& S_0(X)Y_0^0(\Omega) + P_0(X)Y_1^0(\Omega) + D_0(X)Y_2^0(\Omega) + F_0(X)Y_3^0(\Omega) \\ =& \frac{5\sqrt{7}}{2}F_0(X)Z^3 + \frac{3\sqrt{5}}{2}D_0(X)Z^2 + (\sqrt{3}P_0(X) - \frac{3\sqrt{7}}{2}F_0(X))Z \\ &+ (S_0(X) - \frac{\sqrt{5}}{2}D_0(X)), \end{aligned} \tag{9.2}$$

where Z stands for $Z = \cos\theta$. This third order polinomial function of Z has three complex roots $Z_K^0(X), (K=1,2,3)$, which are often called Barrelet zeros. Using these

roots, above amplitude can be written by the form of products:

$$A_0(X,\Omega) = C_0(X) \prod_{K=1}^{\tilde{L}} (Z - Z_K^0(X)) \tag{9.3}$$

Similarly, helicity 1 **NPE** and UPE amplitudes $A_\pm(X,\Omega)$ can be expressed in terms of roots $Z_K^\pm(X)$ as :

$$A_+(X,\Omega) = C^+(X)\sin(\phi)\sin(\theta) \prod_{K=1}^{\tilde{L}-1} (Z - Z_K^+(X)) \tag{9.4}$$

$$A_-(X,\Omega) = C^-(X)\cos(\phi)\sin(\theta) \prod_{K=1}^{\tilde{L}-1} (Z - Z_K^-(X)) \tag{9.5}$$

These roots $Z_K^\pm(X)$ are also obtained from the explicit form of $A_\pm(X,\Omega)$. In the case $\tilde{L} = 3$, these amplitudes can be written:

$$\begin{aligned} A_+(X,\Omega) &= P_+(X)\{\sqrt{\frac{1}{2}}(Y_1^{+1}(\Omega) + Y_1^{-1}(\Omega)\} + D_+(X)\{\sqrt{\frac{1}{2}}(Y_2^{+1}(\Omega) + Y_2^{-1}(\Omega)\} \\ &+ F_+(X)\{\sqrt{\frac{1}{2}}(Y_3^{+1}(\Omega) + Y_3^{-1}(\Omega)\} \\ &= -i\cdot\sin(\phi)\sin(\theta)\cdot\{\frac{15}{2}\sqrt{\frac{7}{6}}F_+(X)Z^2 + \frac{3\sqrt{5}}{\sqrt{3}}D_+(X)Z \\ &+ (\sqrt{3}P_+(X) - \frac{3}{2}\sqrt{\frac{7}{6}}F_+(X))\} \end{aligned} \tag{9.6}$$

$$\begin{aligned} A_-(X,\Omega) &= P_-(X)\{\sqrt{\frac{1}{2}}(Y_1^{+1}(\Omega) - Y_1^{-1}(\Omega)\} + D_-(X)\{\sqrt{\frac{1}{2}}(Y_2^{+1}(\Omega) - Y_2^{-1}(\Omega)\} \\ &+ F_-(X)\{\sqrt{\frac{1}{2}}(Y_3^{+1}(\Omega) - Y_3^{-1}(\Omega)\} \\ &= -i\cdot\cos(\phi)\sin(\theta)\cdot\{\frac{15}{2}\sqrt{\frac{7}{6}}F_-(X)Z^2 + \frac{3\sqrt{5}}{\sqrt{3}}D_-(X)Z \\ &+ (\sqrt{3}P_-(X) - \frac{3}{2}\sqrt{\frac{7}{6}}F_-(X))\} \end{aligned} \tag{9.7}$$

These second order complex coefficient functions of Z have two roots $Z_K^\pm, (K = 1,2)$.

If we write the amplitudes in the form of prodcucts like this, it can be seen from (9.1) that the change of $Z_K^{0,\pm} \rightarrow Z_K^{*0,\pm}$ gives the same value of angular distribution, if $A_0 A_-^* = 0$. This means that there are different set of solutions in the choice of the signs of $ImZ_K^{0,\pm}$ as far as $ImZ_K^{0,\pm} \neq 0$, since the change of the Barret zeros $Z_K^{0,\pm} \rightarrow Z_K^{*0,\pm}$ results different set of amplitudes. This is the origin of the discrete ambiguities of amplitudes existing in the set of equations Table-10.

In the case of $\tilde{L} = 3$, the maximum number of solutions for **NPE** amplitude are $2^{3-1} = 4$. But half of these solutions differ only the sign of the overall relative phase and give the same the intensity of the amplitudes. Then this number is reduced two as far as discussing the absolute value of the amplitudes. While for **UPE** amplitudes the possible solutins are $2^3/2 = 4$, also ignoring the phase difference and neglecting small helicity 1 **UPE** amplitudes.

In the analysis of the reaction $K^- p \rightarrow K^- \eta p$, the seach of these possible all solutions have been carried out by following ways. We, at first, determined the barret zeros from one set of amplitudes obtained form the first fit of moments. Another possible set of solutions were, then, calculated from these barret zeros by changing the sign of imaginal part of $Z_K^{0,\pm}$. In this time, I ignored the ambiguties of small helicity 1 **UPE** amplitudes. Lastly, refit of the moments were carried out using these new set of the amplitudes as initial value of the fit. This fit may be necessary since the helicity 1 **UPE** amplitude were not exactory zeros.

In this way, I have checked all possible solutions in the full mass region, but no significant difference of the solutions was observed in all underling waves. In the mass region $\geq 1.75 \mathrm{GeV/c^2}$, relatively large difference was observed between two solutions of **NPE** amplitudes (P_+ and D_+), but its difference was in the order of one statistical errors. No significant difference was observed between all 4 solutions for helicity 0 **UPE** amplitudes (S_0, P_0, D_0) in the full mass region.

10. Appendix-2

The Monte Carlo Simulation of LASS spectrometer

In this appendix, the simulation program of LASS Spectrometer is briefly discussed to demonstrate how real responce of the LASS spectrometer are taken into account. In this program, a special attention is payed to various points in the generation of beam profile , particle tracking and the simulation of device response.

Beam generation

Because phase space of the incoming beam depends on the steering of the primary and secondary beam lines, randumly selected real beam tracks taken from T3 trigger are used to generate beam track position and the momentum at the interaction point. The secondary beams tracks are also simulated using the secondary tracks in T3 events. In this way, the effects of the secondary beam tracks on the helix-track reconstruction are properly incorporated.

Particle tracking

The traveling of the charged particles in the magnetic field is performed by a fourth-order Runge-Kutta method using measured field map. The nominal step size is 30cm decreasing when necessary to ensure the accuracy of the resulting trajectory. The detailed geometrical location of the target and detectors in the Solenoid and Dipole spectrometer are incorporated as being composed of 'volumes' that responde to the passage of particles. The effects included in the traveling of particles are

1. multiple coulomb scattering.
2. enegy loss in the material.
3. nuclear absorption. The difference in the nuclear cross section for various particles and the momentum also taken into account. The nuclear absorption process is modeled simply that particle stops in the material and no secondary particles are generated.
4. weak decays of charged and neutral particles.

Simulation of device response

The efficiency and resolution known from the real data are incorporated into the simulation programs in each components of the devices. In the simulation program, the wire-by-wire efficiencies of PWC anode are taken into account. Dead-wires, inefficient region of supports wire and a few notably inefficient planes in a special period of the experiments are, also, taken into account. The PWC anode coordinates are simulated by digitizing the position of the particle to the nearest anode wire. The multi-anode hits are, also, simulated by modeling the the correlation between the anode cluster size (number of hit wires) and the angle of the tracks in the plane orthogonal to the direction of the anode wire.

The cathode coordinate is simulated in one of two way. One way is the direct pulse height simulation by smearing the pulse height itself so as to reproduce the observed cathode spacial resolution. In this way, the overlap of the cathode pulses caused by two tracks can be simulated, automatically. In the second method, cathode coordinates are smeared by the known cathode resolution and effects of the overlap of multiple cathode peaks are taken into account.

In the simulation of the MS chambers, those effects are incorpolated that the wand read out electronic merges the two coordinate that less than 0.45 cm apart. In the twixt region, the effective efficiency of the MS chambes are tuned so that the track-finding efficiency agrees between real data and MC events.

The simulation of the Čerenkov counters is performed by swimming the charged particles through the counter and determining how many Čerenkov photons are given by the particle in each cell. This number is determined empirically from the studies of the light detection efficiency of each cell.

REFERENCES

1. D. Aston et al., Phys. Lett. 99B (1981) 502
   D. Aston et al., Phys. Lett. 106B (1981) 235
   D. Aston et al., Phys. Lett. 149B (1984) 258
   D. Aston et al., Nucl. Phys. B247 (1984) 261
2. D. Aston et al., Phys. Letters 180B (1986) 308
3. C. Daum et al., Nucl. Phys. B187 (1981) 1
4. D. Aston et al., SLAC-PUB-4260/DPNU-87-25,
   to be published in Nucl. Phys. B.
5. D. Aston et al., SLAC-PUB-3972/DPNU-86-15,
   to be published in Nucl. Phys. B.
6. P. Estabrooks et al., Nucl. Phys. B133 (1978) 490
   P. Estabrooks, Phys. Rev. D19 (1979) 2678
7. W. E. Cleland et al., Nucl. Phys. B208 (1982) 189
   A. D. Martin et al., Nucl. Phys. B134 (1978) 392
8. Review of Particle Properties, Particle Data Group, Phys. Lett. 170B (1986) 1
9. J. Badier et al., Phys. Lett. 19 (1965) 612
   G. Bassompiere et al., Nucl. Phys. B13 (1969) 189
   J. M. Bishop et al., Nucl. Phys. B9 (1969) 403
   M. Aguilar-Benitez et al., Phys. Rev. D4 (1971) 2583
10. H. J. Lipkin, Phys. Rev. Lett. 46 (1981) 1307
11. H. J. Lipkin, Proceeding of the second International Conference on Hodron Spectroscopy, Tsukuba (1987) 365
12. M. Bauer and B. Stech, Phys. Lett. 152B (1985) 380
13. M. Bauer, B. Stech and M. Wirbel, Z. Phys. C34 (1987) 103
14. H. Albrecht et al.(ARGUS), Phys.Lett. 158B(1985) 525
    C. Bebec et al.(CLEO), Phys.Rev.Lett. 56(1986) 1983
    C. Baltusaitis et. al.(Mark III), Phys.Lett. 56(1986) 2136

15. R. Rückl , Proceeding of the XXIII International Conference on High Energy Physiscs, Berkeley (1986) 797

16. A. Buras ,J. Gerard and R. Rückl, Nucl.Phys. B268(1986) 16

17. F. J. Gilman and R. Kauffman, SLAC-PUB-4301

18. Etkin et al. , Phys. Rev. D22 (1980) 42
Baubilli et. al., Nucl. Phys. B202 (1982) 21

19. Nathan Isgur , Phys. Rev. D12 (1975) 3770

20. P.Langacker , Phys.Lett. 90B (1975) 447

21. S. Godfrey and N. Isgur , Phys.Rev. D32 (1985) 189

22. M.S. Chanowitz , Proceeding of the Second International Conference on Hadron Spectroscopy (1987) 269

23. J.F. Donoghue,B.R. Holstein, and Y.C. R. Lin Phys. Rev. Lett. 55 (1985) 2766

24. W.D. Apel et. al. Phys. Lett. 83B (1979) 198

25. N.R. Stanton et. al. Phys. Lett. 92B (1980) 353

26. The LASS Spectrometer. SLAC-Report-298 April 1986

27. F.Binon et al., Nuovo Cim. 78A,313(1983)

28. D.Alde et al., Nucl. Phys. B269,485(1986)

29. S.Shapiro et al., "A proportional Chamber Front End Amplifier and Pulse Shaping Circuit," IEEE Trans. Nucl. Sci. NS23(1976) 264.

30. S.Shapiro et al., "A Dead Timeless Shift Register Style Readout Scheme for Multiwire Proportional Chambers," IEEE Trans. Nucl. Sci. NS23(1976) 269.

31. E.Cisneros et al., "A Low Noise PWC Cathode Readout System," IEEE Trans. Nucl. Sci. NS28(1981) 465.

32. M.Breidenbach et al., "A Semi-Autonomous Controller for Data acquisition: The Brilliant ADC," SLAC-PUB-2032 (1977)

33. G. Costa et al., Nucl. Phys. B175 (1980) 402

34. M. Blatt and V. F. Weisskopf, Theoretical Nuclear Physics (Wiley, N.Y.,1952)

35. E.Barret,Nuovo.Cimento. 8A (1972) 331, A.Gersten, Nucl.Phys. B12(1969) 537